

**An Experimental and Numerical Investigation of the Three-Dimensional
Flow Field About a Ram Accelerator Projectile**

by

John B. Hinkey Jr.

A dissertation submitted in partial fulfillment
of the requirements for the degree of

Doctor of Philosophy

University of Washington

1994

Approved by _____
(Chairperson of Supervisory Committee)

Program Authorized
to Offer Degree _____ Aeronautics and Astronautics _____

Date _____ March 18, 1994 _____

In presenting this dissertation in partial fulfillment of the requirements for the Doctoral degree at the University of Washington, I agree that the Library shall make its copies freely available for inspection. I further agree that extensive copying of this dissertation is allowable only for scholarly purposes, consistent with "fair use" as prescribed in the U.S. Copyright Law. Requests for copying or reproduction of this dissertation may be referred to University Microfilms, 1490 Eisenhower Place, P.O. Box 975, Ann Arbor, MI 48106, to whom the author has granted "the right to reproduce and sell (a) copies of the manuscript in microform and/or (b) printed copies of the manuscript made from microform."

Signature _____

Date _____

University of Washington

Abstract

An Experimental and Numerical Investigation of the Three-Dimensional
Flow Field About a Ram Accelerator Projectile

by John B. Hinkey Jr.

Chairman of Supervisory Committee:

Professor Abraham Hertzberg
Dept. of Aeronautics and Astronautics

An experimental and numerical investigation of the three-dimensional flow field associated with the ram accelerator projectile is presented. Experiments are performed which measure, with high spatial and temporal resolution, the tube wall pressure induced by a sub-caliber projectile as it travels supersonically through a tube containing a methane-based, pre-mixed combustible gas mixture. These experiments were performed in the sub-, trans, and superdetonative regimes of a single stage and reveal the three-dimensional nature of the projectile flow field as affected by the projectile fins, various combustion phenomena, and the phenomenon of projectile canting. Numerical simulations of the non-reacting three-dimensional flow field using a finite-volume based, inviscid, second-order accurate computational fluid dynamics code help to reveal the structure of the flow field between the projectile and the tube wall and are compared to the experimental results. It is found that the flow field is highly influenced by the projectile fins and that the non-reacting, inviscid simulations agree well with the experimental results. Canting of the projectile is experimentally and numerically verified and is found to have a significant link to the phenomenon of superdetonative projectile unstarts.

Table of Contents

	page
List of Figures	iii
Chapter 1: Introduction	1
1.1 The Ram Accelerator	1
1.2 The Ram Accelerator Experimental Facility	3
1.3 Spatial Resolution of Instrumentation	4
1.4 Projectile Flow Fields	4
Chapter 2: Experimental Apparatus	9
2.1 Highly Instrumented Tube Section	9
2.2 Inserts	11
2.3 Fin Orientation Sensors	12
2.4 Transducer Inadequacies	12
Chapter 3: Numerical Simulation Method	17
3.1 Three-Dimensional Finite Volume Formulation	17
3.2 Flux Solvers	21
3.2.1 <i>Advection Upstream Splitting Method</i>	22
3.2.2 <i>Harten, Lax, and van Leer Approximate Riemann Solver</i>	23
3.3 MUSCL Differencing and Limiters	24
3.3.1 <i>Basics of MUSCL Differencing</i>	24
3.3.2 <i>Limiters</i>	26
3.3.3 <i>Interpolation Using Primitive or Characteristic Variables</i> ...	27
3.4 Convergence Acceleration Techniques	29
3.4.1 <i>Runge-Kutta Time Integration</i>	29
3.4.2 <i>Residual Smoothing</i>	30
Chapter 4: Ideal 3-D Projectile Flow Field	35
4.1 Subdetonative Experimental Results	35
4.2 Numerical Simulations	39
4.3 Comparison Between Experiment and Simulation	42
Chapter 5: Non-Ideal 3-D Projectile Flow Fields	61
5.1 Experiments Exhibiting Non-Ideal Pressure Records	61
5.2 Projectile Canting	66
5.2.1 <i>Definition and Examples of Canted Projectiles</i>	66
5.2.2 <i>Method to Determine Position of Canted Projectiles</i>	68

Table of Contents (con't)

	<i>page</i>
5.2.3 <i>Estimate of the Degree of Projectile Canting</i>	72
5.3 Numerical Simulations of Canted Projectiles	73
5.3.1 <i>Numerical Validation of the Theory of Projectile Canting</i>	73
5.3.2 <i>Simulation of Canted Axisymmetric Projectiles</i>	74
5.3.3 <i>Simulation of Canted Projectiles Including Fin Effects</i>	76
5.4 Implications of Non-Ideal Projectile Flow Fields	79
5.4.1 <i>Projectile Performance</i>	79
5.4.2 <i>Projectile Unstarts</i>	81
Chapter 6: Conclusions	116
6.1 Three-Dimensionality of the Projectile Flow Field	116
6.2 Projectile Canting	117
6.3 Combustion Phenomena	117
6.4 Recommendations for Future Research	117
References	119
Appendix	122

List of Figures

<i>Figure</i>	<i>Page</i>
1-1 Comparison of the ram accelerator to a conventional ramjet.	6
1-2 Geometry of a standard, CNC machined ram accelerator projectile used in the present research.	6
1-3 Propulsive regimes of ram accelerator operations relative to the Chapman-Jouguet (C-J) detonation speed of the combustible gas mixture.	7
1-4 Schematic of the ram accelerator experimental facility.	7
1-5 Illustration of the distance between instrumentation stations relative to the length of a projectile in the present facility.	8
2-1 Highly instrumented tube section (HITS), tube couplers, and existing tube ends. Projectile shown for scale.	14
2-2 Instrumentation stations of the HITS.	14
2-3 Cross sections of two adjacent instrumentation stations of the highly instrumented tube section.	15
2-4 Inserts, tube couplers, and existing tube ends. Projectile shown for scale.	15
2-5 Typical dimensions (in inches) of the thin metal rings used to determine the orientation of the projectile fins relative to the instrumentation ports of the HITS or inserts.	16
2-6 Tube wall pressure trace showing the measured pressure overshoot of approximately 35% for a normal shock in argon passing by an instrumentation station (Burnham, 1993).	16
4-1 Tube wall pressure data from a 4-fin projectile showing the influence of the fins on the flow field. Subdetonative regime, 1540 m/s (Mach 4.2) or 88% of the C-J detonation speed. Gas mixture of $2.7\text{CH}_4+2\text{O}_2+5.8\text{N}_2$	44
4-2 Representation of the tube wall pressure from Fig. 4-1 as being proportional to surface shading and radial distance from the surface of a cylinder representing the tube wall. A gas mixture of $2.7\text{CH}_4+2\text{O}_2+5.8\text{N}_2$, subdetonative regime, 1540 m/s (Mach 4.2) or 88% of the C-J detonation speed.	45
4-3 Same data as shown in Fig. 4-2, but with the cylinder cut away along the centerline of a fin and along the centerline of a channel (the space between adjacent fins). Projectile shown for fin orientation and scale.	46
4-4 Tube wall pressure data from a 4-fin projectile showing the influence of the fins on the flow field. Subdetonative regime, 1440 m/s (Mach 4.0) or 82% of the C-J detonation speed. Gas mixture of $2.7\text{CH}_4+2\text{O}_2+5.8\text{N}_2$	47

List of Figures (con't)

<i>Figure</i>	<i>Page</i>
4-5	Representation of the tube wall pressure from Fig. 4-4 as being proportional to surface shading and radial distance from the surface of a cylinder representing the tube wall. A gas mixture of $2.7\text{CH}_4+2\text{O}_2+5.8\text{N}_2$, subdetonative regime, 1440 m/s (Mach 4.0) or 82% of the C-J detonation speed. Projectile shown for fin orientation and scale. 48
4-6	Tube wall pressure data from a 5-fin projectile. Subdetonative regime, 1560 m/s (Mach 5.3) or 89% of the C-J detonation speed. Gas mixture of $2.7\text{CH}_4+2\text{O}_2+5.8\text{N}_2$ 49
4-7	Representation of the tube wall pressure from Fig. 4-6 as being proportional to surface shading and radial distance from the surface of a cylinder representing the tube wall. A gas mixture of $2.7\text{CH}_4+2\text{O}_2+5.8\text{N}_2$, subdetonative regime, 1560 m/s (Mach 5.3) or 89% of the C-J detonation speed. Projectile shown for fin orientation and scale. 50
4-8	Tube wall pressure data from a 4-fin projectile travelling at Mach 3.9 (1410 m/s) or 81% of the C-J detonation speed in a non-reacting mixture of $2.7\text{CH}_4+7.8\text{N}_2$. Note the regularity of the shock pattern in the flow behind projectile. 51
4-9	Representation of the tube wall pressure from Fig. 4-8 as being proportional to surface shading and radial distance from the surface of a cylinder representing the tube wall. A non-reacting mixture of $2.7\text{CH}_4+7.8\text{N}_2$, subdetonative regime, 1410 m/s (Mach 3.9) or 81% of the C-J detonation speed of the equivalent reacting mixture. Projectile shown for fin orientation and scale. 52
4-10	Comparison of the experimental tube wall pressure along the centerline of a channel (trace 15 from Fig. 4-8) with that calculated using an axisymmetric simulation. 53
4-11	Three-dimensional view of the projectile geometry used in the numerical simulations of the ideal three-dimensional flow field. 53
4-12	Cross plane grid showing the 1 mm gap between the projectile fin and the tube wall. 54
4-13	Cross plane grids at the 1/4, 1/2, 3/4, and 1 projectile lengths. 54
4-14	Line plots of the calculated tube wall pressure of a 4-fin projectile as a function of distance at 5 different circumferential angles from the centerline of a fin to the centerline of a channel. Projectile velocity of 1400 m/s (Mach 4.0) in a non-reacting mixture of $2.7\text{CH}_4+2\text{O}_2+5.8\text{N}_2$ 55
4-15	Tube wall pressure distribution from the numerical simulation of a 4-fin projectile travelling at 1400 m/s (Mach 4.0) in a non-reacting mixture of $2.7\text{CH}_4+2\text{O}_2+5.8\text{N}_2$ 56

List of Figures (con't)

<i>Figure</i>	<i>Page</i>
4-16	Calculated projectile body surface pressure distribution of a 4-fin projectile travelling at 1400 m/s (Mach 4.0) in a non-reacting mixture of $2.7\text{CH}_4+2\text{O}_2+5.8\text{N}_2$ 57
4-17	Line plots of the calculated tube wall pressure of a 4-fin projectile as a function of distance at 5 different circumferential angles from the centerline of a fin to the centerline of a channel. Projectile velocity of 1850 m/s (Mach 5.1) in a non-reacting mixture of $2.7\text{CH}_4+2\text{O}_2+5.8\text{N}_2$ 58
4-18	Calculated tube wall pressure distribution for a 4-fin projectile travelling at 1850 m/s (Mach 5.1) in a non-reacting mixture of $2.7\text{CH}_4+2\text{O}_2+5.8\text{N}_2$ 59
4-19	Calculated projectile body pressure distribution of a 4-fin projectile travelling at 1850 m/s (Mach 5.1) in a non-reacting mixture of $2.7\text{CH}_4+2\text{O}_2+5.8\text{N}_2$ 60
5-1	Tube wall pressure traces from the first set of pressure transducers in the HITS. Subdetonative regime, 1400 m/s (Mach 3.9) or 80% of the C-J detonation speed. 84
5-2	Tube wall pressure traces from the first set (a) and the second set (b) of pressure transducers in the HITS. Transdetonative regime, 1850 m/s (Mach 5.1) or 106% of the C-J detonation speed. 85
5-3	Tube wall pressure traces from the pressure transducers in the inserts. Superdetonative regime, 1960 m/s (Mach 5.4) or 112% of the C-J detonation speed. 86
5-4	Reconstructed tube wall pressure distribution from the superdetonative regime, 1960 m/s (Mach 5.4) or 112% of the C-J detonation speed. Pressure data are proportional to surface shading and radial distance from the surface of a cylinder representing the tube wall. Pressure normalized by initial tube fill pressure. 87
5-5	Tube wall pressure traces from the transducers in the inserts. Superdetonative regime, 2020 m/s (Mach 5.6) or 115% of the C-J detonation speed. 88
5-6	Reconstructed tube wall pressure distribution from the superdetonative regime, 2020 m/s (Mach 5.6) or 115% of the C-J detonation speed. Pressure data are proportional to surface shading and radial distance from the surface of a cylinder representing the tube wall. Pressure normalized by initial tube fill pressure. 89

List of Figures (con't)

<i>Figure</i>	<i>Page</i>
5-7	Qualitative comparison of a tube wall pressure trace from Fig. 5-5 with the numerical simulation of Soetrisno et. al (1992). Experimental conditions are 2020 m/s (Mach 5.6) or 115% of the C-J detonation speed with a mixture of $2.7\text{CH}_4+2\text{O}_2+5.8\text{N}_2$ at 32 atm. Numerical conditions are 1840 m/s (Mach 5.0) or 104% of the C-J detonation speed with a mixture of $2.5\text{CH}_4+2\text{O}_2+5.5\text{N}_2$ at 31 atm. 90
5-8	Three possible positions of a projectile relative to the tube wall. 91
5-9	Illustration of the difference in arrival position of the initial shock and the magnitude of the reflection at the opposing sides of a tube for a canted projectile. 91
5-10	Tube wall pressure traces using the HITS illustrating a canted projectile. Subdetonative regime, 1560 m/s (Mach 4.3) or 89% of the C-J detonation speed. Reacting mixture of $2.7\text{CH}_4+2\text{O}_2+5.8\text{N}_2$ 92
5-11	Tube wall pressure traces from Fig. 5-10 with the time scale expanded to accentuate the difference in arrival time of the initial shock wave. The arrival points of the initial shock wave have been connected by lines between traces for better visualization. 93
5-12	Tube wall pressure traces illustrating a canted projectile, superdetonative regime, 1920 m/s (Mach 5.3) or 110% of the C-J detonation speed of the equivalent reacting gas. A non-reacting gas mixture of $2.7\text{CH}_4+7.8\text{N}_2$ 94
5-13	Tube wall pressure traces from Fig. 5-12 with the time scale expanded to accentuate the difference in arrival time of the initial shock wave and the variation in the magnitude of the reflected shock. 95
5-14	Notation for determining the approximate location of the projectile nose tip. 96
5-15	Notation for the oblique shock relations in the immediate vicinity of the tube wall. 96
5-16	General geometry of a canted axisymmetric three-dimensional projectile and the tube wall used in the numerical simulations. One-half of the full tube is numerically simulated by assuming a plane of symmetry. The computational grid is $149 \times 49 \times 49$ cells in the axial, radial, and circumferential directions respectively. 97
5-17	Calculated upper and lower tube wall pressure for an axisymmetric projectile which is translated by 2 mm (0° angle of attack) toward the lower wall. Mach 4.0 (1450 m/s) or 83% of the C-J detonation speed of the equivalent reacting gas mixture. The position where the initial shock wave reflects from the tube wall is different while the magnitude of the reflections are equal. 97

List of Figures (con't)

<i>Figure</i>	<i>Page</i>
5-18 Calculated upper and lower tube wall pressure for a canted axisymmetric projectile. The nose tip is translated by 5 mm toward the lower wall with an angle of attack of 4°. Mach 4.0 (1450 m/s) or 83% of the C-J detonation speed of the equivalent reacting gas mixture. The positions where the initial shock wave reflects from the tube wall are different and the magnitude of the reflections are not equal.	98
5-19 General geometry of a canted axisymmetric three-dimensional projectile and the tube wall used in the numerical simulations. One-half of the full tube is numerically simulated by assuming a plane of symmetry while only the first 2/3 of the projectile length (102 mm) is simulated. The computational grid is 149x49x49 in the axial, radial, and circumferential directions respectively.	98
5-20 Comparison of calculated (bottom) to experimental (top) tube wall pressure traces for a canted projectile with an estimated angle of attack of 4.5° and a nose tip translation of 7.5 mm. Subdetonative regime, 1560 m/s (Mach 4.3) or 89% of the C-J detonation speed.	99
5-21 Three-dimensional surface plot of the calculated tube wall pressure distribution resulting from a canted axisymmetric projectile with an angle of attack of 4.5° and a nose tip translation of 7.5 mm. Subdetonative regime, 1560 m/s (Mach 4.3) or 89% of the C-J detonation speed. Surface shading is proportional to pressure.	100
5-22 Three-dimensional surface plot of the calculated body surface pressure distribution of a canted axisymmetric projectile with an angle of attack of 4.5° and a nose tip translation of 7.5 mm. Pressure distribution of the upper and lower symmetry planes also shown. Subdetonative regime, 1560 m/s (Mach 4.3) or 89% of the C-J detonation speed. Surface shading is proportional to pressure.	101
5-23 Comparison of calculated (bottom) and experimental (top) tube wall pressure traces for a canted projectile with estimated angle of attack of 3° and a nose tip translation of 6.5 mm. Superdetonative regime, 1920 m/s (Mach 5.3) or 110% of the C-J detonation speed. Non-reacting mixture of 2.7CH ₄ +7.8N ₂	102
5-24 Three-dimensional surface plot of the calculated tube wall pressure distribution resulting from a canted axisymmetric projectile with an angle of attack of 3° and a nose tip translation of 6.5 mm. Superdetonative regime, 1920 m/s (Mach 5.3) or 110% of the C-J detonation speed. Surface shading is proportional to pressure.	103

List of Figures (con't)

<i>Figure</i>	<i>Page</i>
5-25 Three-dimensional surface plot of the calculated body surface pressure distribution of a canted axisymmetric projectile with an angle of attack of 3° and a nose tip translation of 6.5 mm. Pressure distribution of the upper and lower symmetry planes also shown. Superdetonative regime, 1920 m/s (Mach 5.3) or 110% of the C-J detonation speed. Surface shading is proportional to pressure.	104
5-26 Projectile geometry used in the simulation of a canted projectile with fins which has an angle of attack of 4.5° and a nose tip translation of 7.5 mm. 149x119x29 cell grid in the axial, circumferential and radial directions respectively.	105
5-27 Three-dimensional surface plots of the calculated tube wall pressure distribution resulting from a canted projectile with fins which has an angle of attack of 4.5° and a nose tip translation of 7.5 mm. Subdetonative regime, 1560 m/s (Mach 4.3) or 89% of the C-J detonation speed. Surface shading is proportional to pressure.	106
5-28 Three-dimensional surface plots of the calculated body surface pressure distribution of a canted projectile with fins which has an angle of attack of 4.5° and a nose tip translation of 7.5 mm. Pressure distribution of the upper and lower symmetry planes also shown. Subdetonative regime, 1560 m/s (Mach 4.3) or 89% of the C-J detonation speed. Surface shading is proportional to pressure.	107
5-29 Line plots of the calculated tube wall pressure distribution of a canted projectile with fins which has an angle of attack of 4.5° and a nose tip translation of 7.5 mm. Subdetonative regime, 1560 m/s (Mach 4.3) or 89% of the C-J detonation speed. These 5 traces correspond to 45° increments in circumferential angle from the upper to lower wall.	108
5-30 Projectile geometry used in the simulation of a canted projectile with fins which has an angle of attack of 3° and a nose tip translation of 6.5 mm. 149x119x29 cell grid in the axial, circumferential and radial directions respectively.	109
5-31 Three-dimensional surface plot of the calculated tube wall pressure distribution resulting from a canted projectile with fins which has an angle of attack of 3° and a nose tip translation of 6.5 mm. Superdetonative regime, 1920 m/s (Mach 5.3) or 110% of the C-J detonation speed. Surface shading is proportional to pressure.	110

List of Figures (con't)

<i>Figure</i>	<i>Page</i>
5-32 Three-dimensional surface plot of the calculated body surface pressure distribution of a canted projectile with fins which has an angle of attack of 3° and a nose tip translation of 6.5 mm. Pressure distribution of the upper and lower symmetry planes also shown. Superdetonative regime, 1920 m/s (Mach 5.3) or 110% of the C-J detonation speed. Surface shading is proportional to pressure.	111
5-33 Line plots of the calculated tube wall pressure distribution of a canted projectile with fins which has an angle of attack of 3° and a nose tip translation of 6.5 mm. Subdetonative regime, 1920 m/s (Mach 5.3) or 110% of the C-J detonation speed. These 5 traces correspond to 45° increments in circumferential angle from the upper to lower wall.	112
5-34 Plot of projectile velocity versus distance for 5-fin and 4-fin projectiles. Single-stage of 16 m in length, gas mixture of $2.7\text{CH}_4 + 2\text{O}_2 + 5.8\text{N}_2$, and a tube fill pressure of 28 atm. Projectile masses are 74 gm and 84 gm for 4-fin and 5-fin projectiles respectively.	113
5-35 Tube wall pressure traces from a projectile unstart. Superdetonative regime, 2060 m/s (Mach 5.7) or 118% of the C-J detonation speed. Note the large amplitude shock wave and the remains of the initial conical shock generated by the projectile nose cone.	114
5-36 Comparison of data from trace 1 of Fig. 5-35 to that of an instrumentation station approximately 22 cm upstream (opposite the direction of projectile motion) with the same azimuthal orientation. Magnetic sensor data shown below to correlate projectile position with the pressure traces. Note difference in shock pressure peak amplitude.	115

ACKNOWLEDGMENTS

The author would like to acknowledge those who have contributed significantly towards the completion of this dissertation. First, the members of his supervisory committee: Abraham Hertzberg, Adam P. Bruckner, David T. Pratt, and Scott Eberhardt. Their input and constructive criticism over the four years of my tenure at the University of Washington were greatly appreciated and helped to significantly improve the quality of this work. Malcolm Saynor is greatly appreciated for his quick responses to frequent “machining emergencies”. My fellow graduate students, Andrew J. Higgins and Gilbert Chew, are the ones who helped to keep my perspective and sanity, mostly through comic relief and intelligent (and sometimes seemingly not-so-intelligent) discussions on just about every topic known to man (or at least known to grad students who watched NOVA, Charley Rose, The Simpsons, or Star Trek the night before). Edward A. Burnham has perhaps contributed the most to the research for this dissertation by assisting in the experiments and numerical simulations, truly co-authoring publications, processing data, foregoing many a nights sleep to complete an experiment, and generally keeping me on my technical toes. The importance of his contributions cannot be overstated. My parents, John and Evelyn Hinkey, for their support, love, and unbelievable patience during the last eleven years. My sisters, Susan, Jennifer, and Wendy (“Weebs”) for putting up with a brother in absentia who seems to have trouble remembering important dates (like birthdays). Last, but certainly not least, Robin Cross, who has given me her love and patience during the last five years.

Chapter 1: Introduction

This chapter introduces the concept of the ram accelerator and then briefly discusses the different operating regimes and theoretical limits of operation. Descriptions of the facility and general instrumentation are given as well as the limitations of some of the transducers utilized in this study. Past numerical and experimental assumptions concerning the nature of the flow field between the projectile and the tube wall are discussed along with recent experimental and numerical research which takes into account the three-dimensional nature of the ram accelerator flow field. Finally, a description of the present research is given which sets the stage for subsequent chapters.

1.1 The Ram Accelerator

The ram accelerator is a ramjet-in-tube propulsion concept developed at the University of Washington (Hertzberg, Bruckner, and Bogdanoff, 1988) which operates in a manner similar to a conventional ramjet or scramjet, as shown in Fig. 1-1. A sub-caliber projectile similar in shape to the centerbody of a conventional ramjet travels supersonically through a tube filled with a combustible gaseous mixture, with the tube wall acting as an outer cowl. Combustion on and behind the projectile produces a pressure rise which results in a net positive thrust. A typical projectile, shown in Fig. 1-2, has four fins which extend from the sides of the body and serve to center the projectile in the tube. Projectiles are typically fabricated from high strength aluminum or magnesium alloys in two hollow segments, the nose cone and body, which are threaded together to form the complete projectile.

Three regimes of ram accelerator propulsion have been studied to date (Hertzberg, Bruckner, and Knowlen, 1991). These are characterized by the projectile speed relative to the Chapman-Jouguet (C-J) detonation speed of the combustible mixture, as shown in Fig. 1-3. The subdetonative regime occurs at speeds lower than approximately 90% the C-J detonation speed, is characterized by thermal choking of the flow behind the projectile and is therefor known as the thermally choked mode of propulsion (Bruckner, Knowlen, and Hertzberg, 1991). The transdetonative regime occurs between approximately 90% and 110% of the C-J detonation speed, while the superdetonative regime occurs above approximately 110% of the C-J detonation speed. The theoretical velocity limit of a projectile based on a one-dimensional, thermally choked analysis is predicted to be the C-J detonation speed of the combustible gas mixture; however, projectiles routinely operate at velocities considerably greater than this (Bruckner, Knowlen, and Hertzberg, 1991). Using the thermally choked mode of propulsion and transitioning to different gas mixtures once the projectile reaches approximately 90% of the C-J detonation speed of a particular mixture (multiple stages or staging), the University of Washington ram accelerator has achieved velocities near 2700 m/s, with a total velocity gain of nearly 1600 m/s. Single stage velocities have exceeded 2100 m/s in a methane based gas mixture with a total velocity gain in excess of 1000 m/s.

Currently, large scale ram accelerators are a topic of experimental research at other institutions, such as the US Army Research Laboratory (ARL), the US Air Force at Eglin AFB, and overseas at ISL, the French-German Research Institute. Computationally, the ram accelerator is a topic of study at the Naval Research Laboratory (NRL), Science Applications International Corp., Amtec Engineering, Inc., as well as ARL. High spatial resolution measurements are necessary to understand the structure and basic physics of the flow field surrounding the ram accelerator projectile. This information can then be utilized to increase the performance of other experimental facilities as well as assisting in the validation of viscous, unsteady, chemically reacting, three-dimensional CFD codes.

1.2 The Ram Accelerator Experimental Facility

The current ram accelerator facility (Fig. 1-4) consists of a light gas gun, ram accelerator section, final dump tank, and projectile decelerator (Knowlen et al., 1991). The 38 mm bore, 6 m long, single-stage light gas gun is capable of launching an obturator and projectile combination (typical combined mass approximately 60 to 100 g) to speeds up to 1300 m/s. The muzzle of the gas gun is connected to a perforated-wall tube that passes through an evacuated tank, which serves as a dump for the helium driver gas.

The 16 m long ram accelerator section consists of eight steel tubes, with a bore of 38 mm and an outer diameter of 100 mm. There are a total of 144 instrumentation ports at 40 axial locations, spaced at 40 cm intervals along the accelerator tube. At 24 axial stations, there are four ports separated by 90°, and at 16 stations there are three ports separated by 120°. This permits the use of either three or four transducers at each station. Piezoelectric pressure transducers, electromagnetic transducers (copper wire coiled around a Lexan core), and fiber-optic light guides can be located in any of these instrumentation ports. A 32 channel, 1 MHz digital data acquisition system is used to acquire the data. Multiplexing permits monitoring of up to 100 separate input signals.

The ram accelerator tube is designed to operate at propellant fill pressures up to 50 atm. Thin Mylar diaphragms are used to close off each end of the accelerator tube and to separate sections of the tube filled with different propellant mixtures. The fuel, oxidizer, and diluent gases are metered using sonic orifices and directed to the appropriate sections of the ram accelerator tube.

The end of the accelerator tube is connected by a 0.76 m long drift tube to a 2.4 m long evacuated dump tank, where the projectile experiences free flight. The tank has a pair of 25 cm diameter viewing ports used for high-speed photography. The free-flying projectile impacts a metal witness plate and is brought to a stop in carpet remnants that are tightly packed in a 20 cm bore by 1 m long tube attached to the far end and inside of the final dump tank.

1.3 Spatial Resolution of Instrumentation

The most important aspect of the present facility relative to this dissertation is the linear and circumferential density of instrumentation along the 38 mm bore tubes. The facility consists of eight two-meter long tubes held together by left- and right-hand threaded collars which join two adjacent tube segments together when rotated. Instrumentation stations are located at 40 cm intervals along the tubes and have alternating 4 port (orthogonal) and 3 port (equispaced) configurations. The 40 cm interval represents 2 to 3 projectile lengths (see Fig. 1-5) and therefore is not adequate for the study of transient phenomena or for high spatial resolution axial measurements, but is reasonable for other studies due to the overall 16 m length of the facility. Also, the 90° or 120° angular resolution at each instrument station is too coarse for measurement of the circumferential variation of the tube wall pressure and luminosity associated with the three-dimensional gas dynamic phenomena produce by the projectile.

1.4 Projectile Flow Fields

Previous to the study of Hinkey, Burnham, and Bruckner (1992), the effects of the projectile fins on the flow field between the projectile surface and the tube wall were thought to be negligible and did not have a significant effect on projectile performance (acceleration and/or maximum velocity). Previous numerical studies had assumed the flow around the projectile to be completely axisymmetric in nature due to the difficulty of modelling three-dimensional flows and also due to the belief that three-dimensional effects were not significant in regards to performance. Recently, with the availability of higher performance computers and enhanced diagnostics, experimental and numerical studies have begun the investigation of the full three-dimensional flow field around the ram accelerator projectile and have taken into account the fins of the afterbody which have a significant effect on the flow field. This dissertation presents the previously published research by the author in the area of the three-dimensional flow field of the ram accelerator projectile as well as recent work which has not been published. The research presented herein utilized highly instrumented sections of tube that have axial resolution on the order

of one-tenth of a projectile length and maximum circumferential (azimuthal) resolution of 22.5° to experimentally investigate the ideal three-dimensional flow field, the non-ideal three-dimensional flow field induced by the phenomenon of projectile canting (the projectile axis is not colinear with the tube axis), as well as other observed gas dynamic phenomena. The interpretation of the experimental data is aided and confirmed by numerical simulations of various projectile geometries, using a fully three-dimensional, non-reacting, inviscid, second-order accurate finite volume-based computational fluid dynamics code developed by the author. Additionally, an analytical method is introduced which, in conjunction with experimental data, is able to estimate the position and orientation of a projectile when it is canted. The experimental studies presented in this dissertation were performed in a single 16 m long stage using a methane-based combustible gas mixture of $2.7 \pm 0.1 \text{CH}_4 + 2\text{O}_2 + 5.8 \pm 0.1 \text{N}_2$ which has an experimentally determined C-J detonation speed of approximately 1750 m/s. Experiments were also performed in a non-reacting mixture of $2.7 \text{CH}_4 + 7.8 \text{N}_2$ which has nearly identical non-reacting thermodynamic properties of the combustible mixture. High resolution tube wall pressure data were recorded in the sub-, trans-, and superdetonative regimes with velocities between 1400 m/s and 2060 m/s. Initial tube fill pressures of 18 to 35 atm were used. Projectiles manufactured from a high strength aluminum alloy (7071-T651) by computer numerically controlled (CNC) machines were exclusively utilized. Projectiles having either four or five fins were used which had nominal masses of 74 and 84 gm respectively.

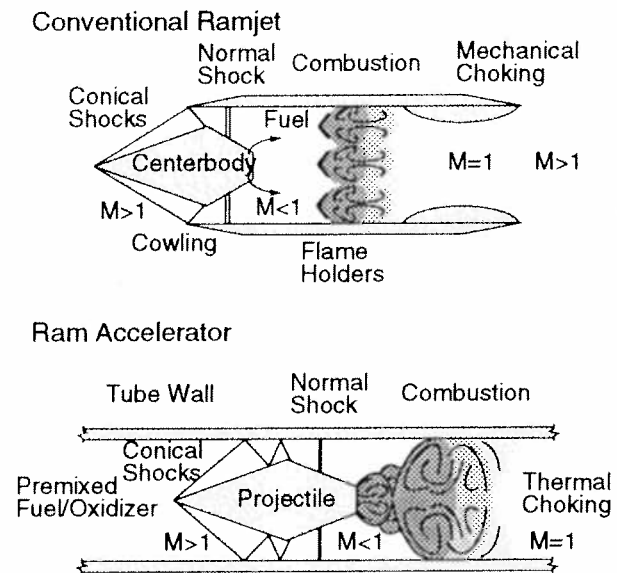


Figure 1-1: Comparison of the ram accelerator to a conventional ramjet.

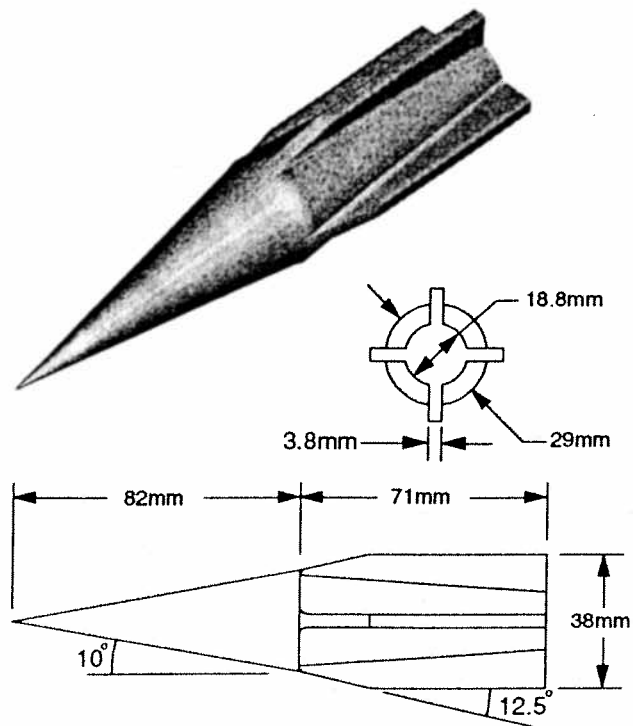


Figure 1-2: Geometry of a standard, CNC machined ram accelerator projectile used in the present research.

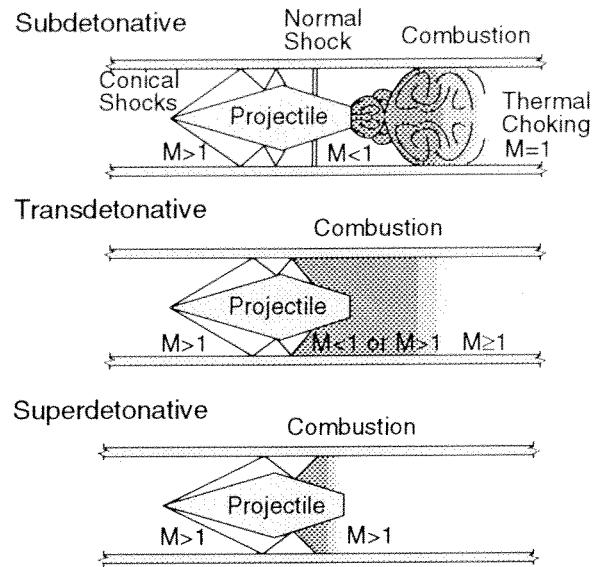


Figure 1-3: Propulsive regimes of ram accelerator operations relative to the Chapman-Jouguet (C-J) detonation speed of the combustible gas mixture.

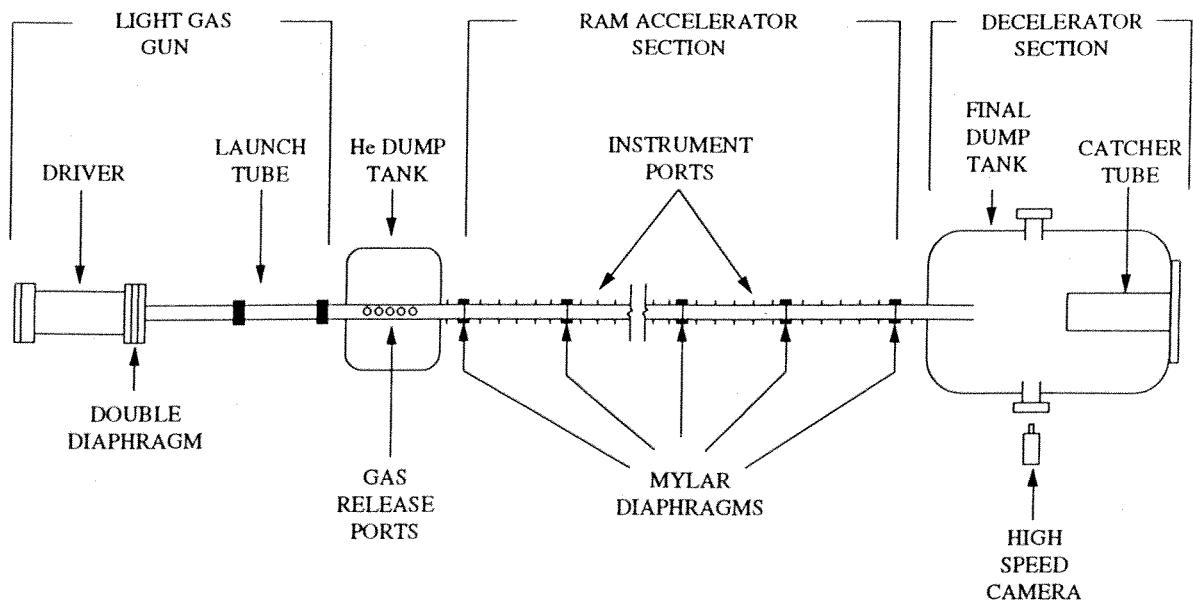


Figure 1-4: Schematic of the ram accelerator experimental facility.

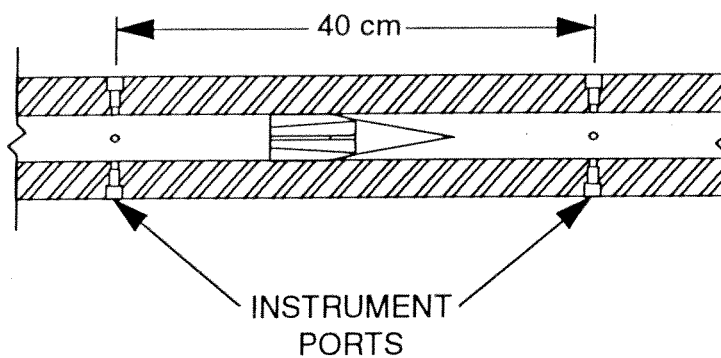


Figure 1-5: Illustration of the distance between instrumentation stations relative to the length of a projectile in the present facility.

Chapter 2: Experimental Apparatus

This chapter describes two types of special high instrument density sections of tube known as the highly instrumented tube section (HITS) and inserts. The method by which they are installed in the ram accelerator facility are schematically shown. A method which allows the orientation of the projectile fins relative to the instrumentation ports is developed. The inadequacies of the transducers which were subsequently installed in these special tube sections are also illuminated and the effect on interpretation of the experimental data is discussed.

2.1 Highly Instrumented Tube Section

To perform tube wall pressure and luminosity measurements with the required spatial accuracy it was decided that a special high instrument density tube section was needed. This tube section would need to have sufficient axial and circumferential spatial resolution to study such phenomena as starting transients (ignition and diffuser), mixture transitions, high acceleration (unsteadiness), projectile gas dynamic unstarts, and the three-dimensional flow field surrounding the projectile during operation in the three regimes of propulsion.

There were several design requirements for any method of increasing instrumentation density. First, any additional apparatus must have been able to fit into the existing ram accelerator system with little or no modification to the facility. Second, to study as many phenomena as possible it was necessary for the high instrument density tube section to be insertable nearly anywhere along the 16 m long system. For the study of ignition tran-

sients, only the beginning section of the ram accelerator needed high density instrumentation while for normal operational studies, other locations needed the dense instrumentation. For the study of ignition transients and mixture transitions it was also necessary for the instrumentation to be very close to the mylar diaphragms which separate the light gas gun launcher from the ram accelerator section or which separate the different gas mixtures. Currently, the minimum distance from an instrumentation port to a diaphragm station (the end of an individual tube) is 20 cm and therefore is inadequate for measuring transition or ignition phenomena.

The above requirements precluded the modification of any of the existing tubes because of their design which limited the distance between an instrumentation port and a diaphragm to a minimum of 6 to 8 cm (due to the method used to join individual tubes together). Also, any modified tube containing a significant number of instrumentation ports would be a permanent potential source of combustible gas leaks whether instrumentation was installed or not. In addition, a 2 m long modified tube could not be easily moved to any other part of the system and would therefore lack the necessary flexibility.

Due to the previously described constraints it was decided to construct a separate short section of ram accelerator tube and to design a new tube coupling method. The highly instrumented tube section (HITS) and tube couplers are shown in Fig. 2-1. The tube couplers (one with a right hand internal thread and one with a left hand internal thread) separately thread onto the existing tube segments and provide a sturdy flange to which the HITS is attached and allow the coupling of the entire assembly together. Unlike the original tube coupling system, the flanges allow the HITS to be positioned extremely close to a diaphragm if desired. The length of the tube section was constrained by the maximum available spacing between any two adjacent 2 m long tubes in the system with the facility completely assembled. A 20 mm spacing between the instrumentation stations was chosen as a compromise between structural considerations and the need for high spatial resolution.

The 20 mm spacing between instrumentation stations and the available spacing between existing tubes allowed eight instrumentation stations along the length of the HITS (see Fig. 2-2). The 20 mm spacing of these stations is approximately three times the 6.35 mm diameter of the instrumentation ports. This configuration allows for all eight

instrumentation stations at some point during an experiment to be simultaneously located somewhere along the projectile body, since the typical projectile length is 153 mm (see Fig. 2-1). At each instrumentation station there are four instrumentation ports separated by 90° . There are eight axial stations with each set of ports rotated by 45° relative to the previous station, as shown in Fig. 2-3. Instrumenting two adjacent stations effectively provides a point measurement along the length of the tube with eight ports separated by 45 degrees azimuthally and 20 mm axially. Under proper conditions and with appropriate instrumentation, the HITS can be used to determine the projectile orientation, as well as infer the three-dimensional structure of the flow between the projectile and the tube wall.

The HITS and tube couplers were manufactured from a solid 6 inch diameter rod of hot rolled, heat treated, and stress relieved AISI 4150 modified steel alloy (BD30). This material has a Brinell hardness of 302 (Rockwell C 32), a tensile strength of 156,000 psi and a yield strength of 138,000 psi. Also, this material exhibits high impact resistance and good machinability.

2.2 Inserts

A second type of high instrument density section was subsequently constructed and allows twice the circumferential resolution of the HITS. It consists of two very short sections of tube (Fig. 2-4) which each have 8 instrument ports separated by 45° . When the two short sections are combined or stacked together at different angles the effective angular resolution becomes 22.5° and with the 6.22 mm diameter of the pressure transducers the entire tube circumference is effectively instrumented. These sections are referred to as inserts and are designed to obtain very high circumferential resolution measurements of the flow field surrounding a projectile. The inserts can be used independently or in conjunction with the HITS. The inserts were also manufactured from the same material as the HITS.

2.3 Fin Orientation Sensors

The reliable determination of the orientation of the projectile fins relative to the transducers in the HITS or inserts is very desirable. This allows the recorded tube wall pressures to be correlated with the location of the fins and hence assist in the interpretation of the experimental data. A method was developed which utilized thin disks of brass, aluminum, or lexan which were placed between the HITS or inserts and the downstream tube. The disks, shown in Fig. 2-5 were not solid, but had a center hole which was slightly smaller than the internal diameter of the ram accelerator tubes. Typically the disks were anywhere from 0.050 to 0.010 inches in thickness and had an internal diameter which ranged from 0.050 to 0.010 inch less than the internal diameter of the tube. The idea was that the projectile would pass through the HITS or inserts and subsequently the projectile fins would interfere with the downstream disk, thus producing notches which could be used to determine the orientation of the projectile fins. It was assumed, and has been shown (Knowlen et al., 1992), that projectiles in general do not appreciably spin while accelerating (in fact they only make approximately a complete revolution over the entire 16 m length of the facility when they are purposely induced to spin). It was also assumed that the small interference of the disks with the fins would not interfere with the recorded tube wall pressure, and in fact differences between experiments which utilize the disks and those that do not have not been observed.

2.4 Transducer Inadequacies

There are other difficulties with the present instrumentation which is a result of the fact that individual pressure transducers do not have adequate local spatial resolution or response time (frequency response). The sensitive surface of the pressure transducers is approximately 6.23 mm in diameter (the width of a projectile fin is approximately 3.8 mm) and hence will spatially integrate the tube surface pressure with the center of the probe having the most weight. The frequency response of the pressure transducers is also somewhat inadequate due to the fact that they must be designed to accommodate pressures in excess of 80,000 psi (5,400 atm) and shock loads of 100,000 g's in order to operate in

the present facility. The advertised rise time of the pressure transducers is 1 μ sec with a natural frequency (frequency response) of 0.5 Mhz. The combination of the spatial averaging and somewhat inadequate frequency response must be kept in mind when reviewing experimental data and when comparing it to numerical simulations which may have higher computed spatial resolution and a related inherently higher frequency response.

An additional difficulty with the pressure instrumentation system was found (Hinkey, Burnham, and Bruckner, 1993) to be that transducers sometimes recorded higher than expected pressures for approximately the first 50 μ sec after a shock wave passes the transducer (Fig. 2-6). This was found to be associated with the transducer being recessed from the tube wall a slight amount which has the effect of momentarily increasing the pressure at the transducer face for a short period of time (Burnham, 1993). Measured overpressures were approximately 25% to 35% of the correct value and must be taken into account when comparing experimental tube wall pressure data with those generated numerically.

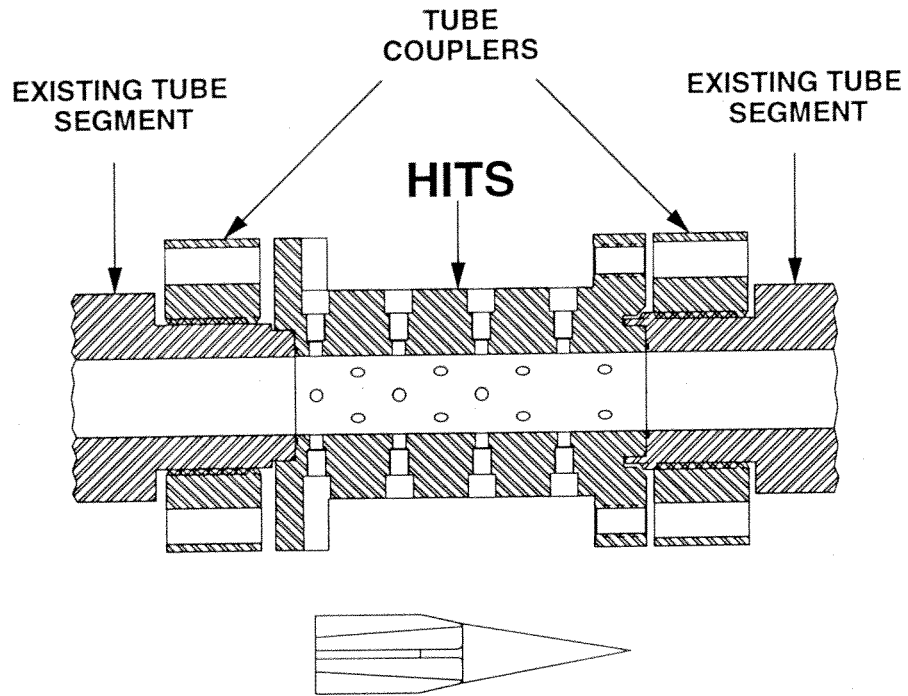


Figure 2-1: Highly instrumented tube section (HITS), tube couplers, and existing tube ends. Projectile shown for scale.

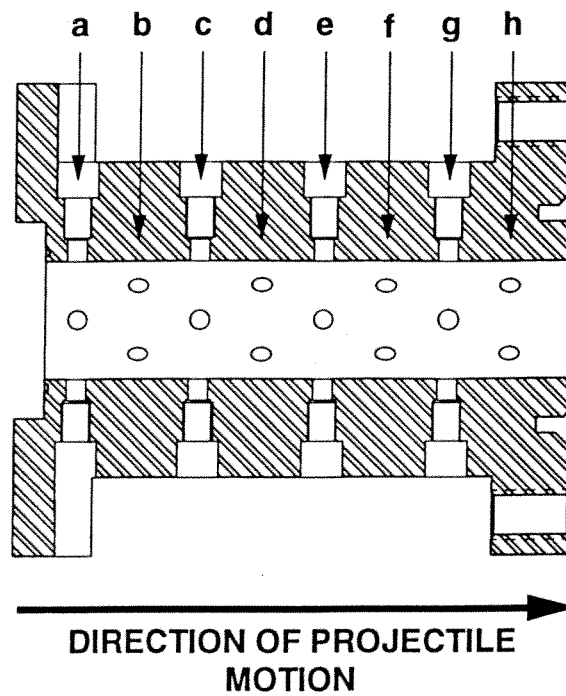


Figure 2-2: Instrumentation stations of the HITS.

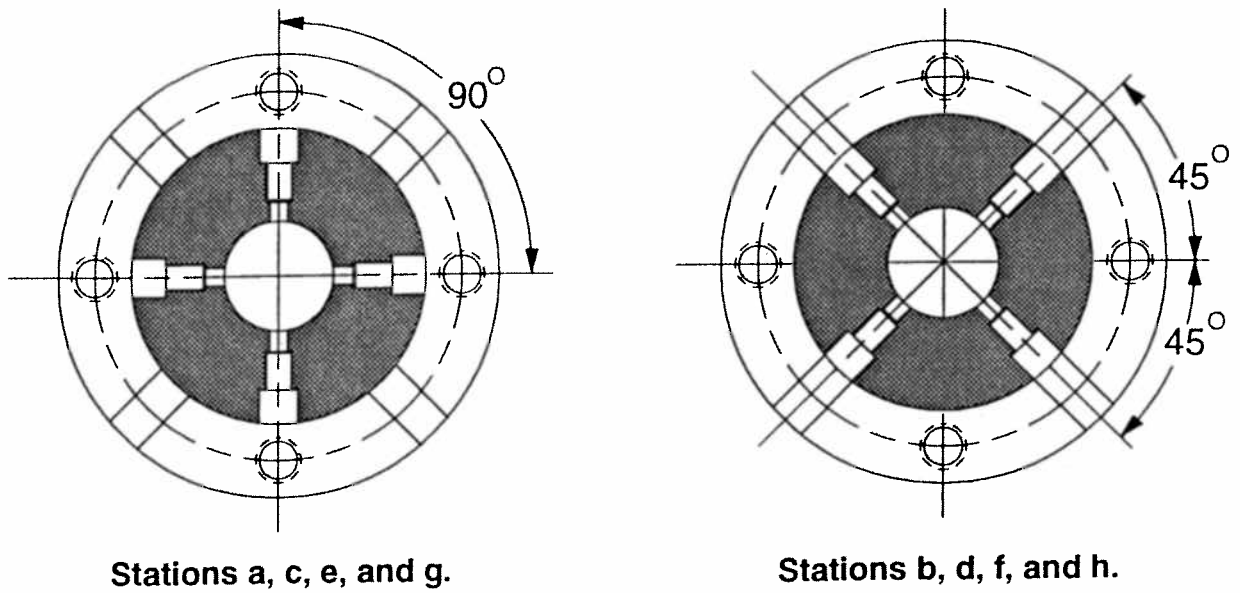


Figure 2-3: Cross sections of two adjacent instrumentation stations of the highly instrumented tube section.

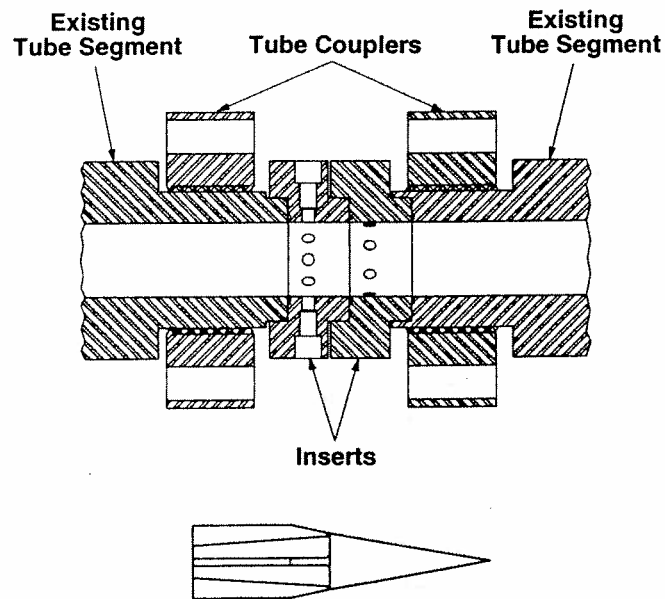


Figure 2-4: Inserts, tube couplers, and existing tube ends. Projectile shown for scale.

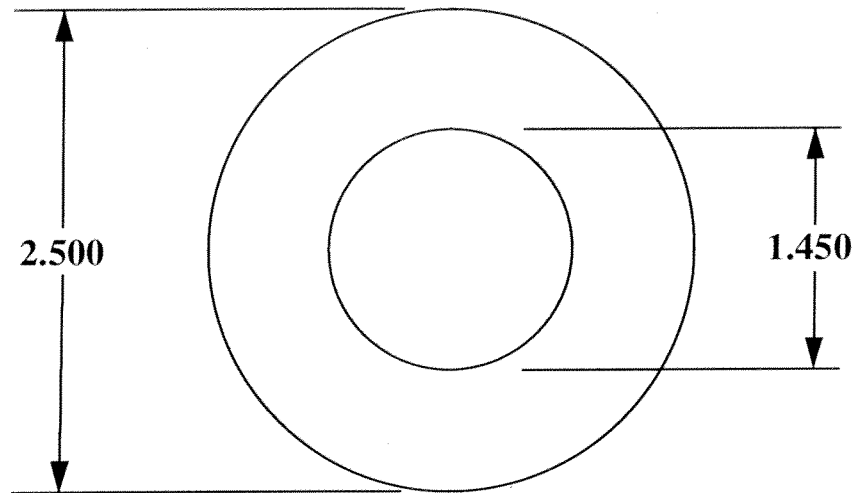


Figure 2-5: Typical dimensions (in inches) of the thin metal rings used to determine the orientation of the projectile fins relative to the instrumentation ports of the HITS or inserts.

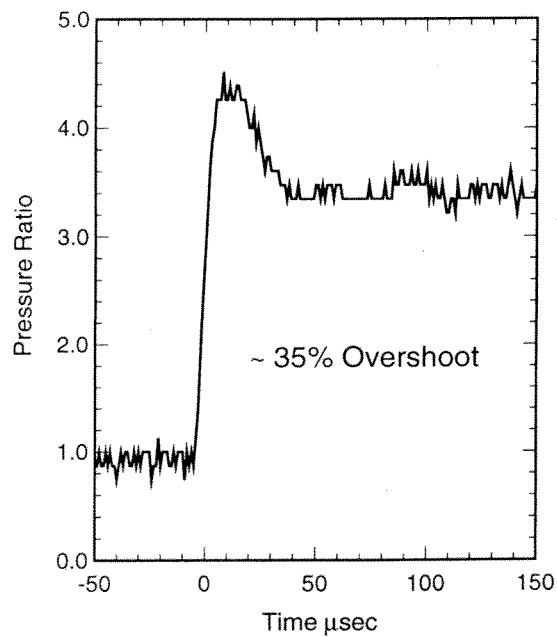


Figure 2-6: Tube wall pressure trace showing the measured pressure overshoot of approximately 35% for a normal shock in argon passing by an instrumentation station (Burnham, 1993).

Chapter 3: Numerical Simulation Method

This chapter describes the numerical method which was used to solve the three-dimensional Euler equations in the numerical simulation of the flow field between the projectile and the tube wall. The general finite volume formulation for solving the Euler equations is developed for a cell centered scheme. Four approximate Riemann solvers are discussed, some of which were used to determine the flux at the cell interfaces. To limit oscillations of the second order accurate solution, various forms of MUSCL differencing with limiters are explored. Finally, several explicit convergence acceleration techniques which were utilized are reviewed.

3.1 Three-Dimensional Finite Volume Formulation

Numerical simulations of the non-reacting, inviscid three-dimensional flow field between the projectile and tube wall were performed with an explicit finite volume based scheme which solved the Euler equations in three-dimensions. Although the following development is done in three-dimensions, the techniques are applicable to one- and two-dimensional codes as well. The three-dimensional Euler equations can be expressed in integral conservation law form as

$$\frac{\partial}{\partial t} \iiint_V Q dV + \iint_S \vec{F} \cdot \vec{n} ds = \iiint_V H dV \quad (3-1)$$

where Q is the vector of conserved variables per unit volume, dV is a differential control volume, \vec{F} is the flux vector, \vec{n} is the outward pointing unit normal of differential area ds ,

and H is a general vector of source terms which may contain body forces, chemical source terms, viscous fluxes or a combination of all three. The vector of conserved variables, Q , is defined as

$$Q = \begin{bmatrix} \rho \\ \rho u \\ \rho v \\ \rho w \\ e \end{bmatrix} \quad (3-2)$$

where ρ is the density, u , v , and w are the cartesian velocities in the x -, y -, and z -directions respectively, and e is the total energy per unit volume and is given by

$$e = \frac{P}{\gamma - 1} + \frac{1}{2}\rho(u^2 + v^2 + w^2) \quad (3-3)$$

where P is the pressure and γ is the ratio of specific heats. The set of equations are closed by the equation of state,

$$P = \rho RT \quad (3-4)$$

where it is assumed that the fluid behaves as an ideal gas with constant specific heats (R and γ are constants, i.e., a calorically perfect gas).

The Cartesian fluxes, \vec{F} , are given by

$$\vec{F} = F_x \hat{i} + F_y \hat{j} + F_z \hat{k} \quad (3-5)$$

where

$$F_x = \begin{bmatrix} \rho u \\ \rho u^2 + P \\ \rho vu \\ \rho wu \\ u(e + P) \end{bmatrix}, \quad F_y = \begin{bmatrix} \rho v \\ \rho uv \\ \rho v^2 + P \\ \rho wv \\ v(e + P) \end{bmatrix}, \quad F_z = \begin{bmatrix} \rho w \\ \rho uw \\ \rho vw \\ \rho w^2 + P \\ w(e + P) \end{bmatrix}. \quad (3-6)$$

The numerical solution to the integral Euler equations is formulated by approximating the integration over differential volumes and differential areas by *finite* volumes and *finite* areas, i.e.,

$$\frac{\partial}{\partial t}(V_{ijk}Q_{ijk}) + \left[\sum_{l=1}^{ns} (\vec{F} \cdot \vec{n}s)_l \right]_{ijk} = V_{ijk}H_{ijk} \quad (3-7)$$

where V_{ijk} is the volume of cell ijk , ns is the number of sides of the cell ijk , and s_l is the surface area of side l which has a unit normal of n_l . The vector Q_{ijk} is now the cell average of the conserved variables and is given by

$$Q_{ijk} = \frac{1}{V_{ijk}} \iiint_{V_{ijk}} Q dV. \quad (3-8)$$

A formulation which lends itself more easily to numerical implementation than Eqn. (3-8) is given by

$$\frac{\partial}{\partial t}(V_{ijk}Q_{ijk}) + \left[\sum_{l=1}^{ns} (T^{-1}F_n s)_l \right]_{ijk} = V_{ijk}H_{ijk} \quad (3-9)$$

where F_n is the flux vector in the normal direction with respect to side l and T^{-1} is the transformation matrix which rotates the flux vector into the cartesian coordinates used to define the vector of conserved variables, Q_{ijk} . F_n is then defined as

$$F_n = \begin{bmatrix} \rho u_n \\ \rho u_n^2 + P \\ \rho u_{t_1} u_n \\ \rho u_{t_2} u_n \\ u_n (e + P) \end{bmatrix}, \quad (3-10)$$

where the subscripts n , t_1 , and t_2 denote the normal, 1st tangential and 2nd tangential directions respectively relative to surface area s_l and form an orthogonal system. The variables u_n , u_{t1} , and u_{t2} are then found from

$$Q_n = T \cdot Q \quad (3-11)$$

which is the vector of conserved variables expressed in coordinates normal to side l . The rotation matrix, T , is defined as

$$T = \begin{bmatrix} 1 & 0 & 0 & 0 & 0 \\ 0 & n_x & n_y & n_z & 0 \\ 0 & t_{1x} & t_{1y} & t_{1z} & 0 \\ 0 & t_{2x} & t_{2y} & t_{2z} & 0 \\ 0 & 0 & 0 & 0 & 1 \end{bmatrix} \quad (3-12)$$

where n_x , n_y , n_z are the respective x -, y -, and z -components of the unit normal vector of surface l , t_{1x} , t_{1y} , and t_{1z} are the respective x -, y -, and z - components of the 1st tangential normal vector of surface l , and t_{2x} , t_{2y} , and t_{2z} are the respective x -, y -, and z - components of the 2nd tangential normal vector of surface l .

The normal flux, F_n , is found at each cell interface by approximately solving the Riemann problem, given the “right” and “left” hand states on either side of the surface l . If the source term, H_{ijk} , is assumed to be zero, the solution of the conserved variables at time level n may be updated to the next time level, $n+1$, by

$$Q_{ijk}^{n+1} = Q_{ijk}^n - \frac{\Delta t}{V_{ijk}} \left[\sum_{l=1}^{ns} (T^{-1} F_n s)_l \right]_{ijk} = Q_{ijk}^n - \Delta t \cdot Res_{ijk} \quad (3-13)$$

where Δt is the desired time step (assuming stability constraints are satisfied) and Res_{ijk} is the residual. The time step is chosen as

$$\Delta t = CFL \cdot \frac{V_{ijk}}{|\lambda_\xi| \cdot s_\xi + |\lambda_\eta| \cdot s_\eta + |\lambda_\zeta| \cdot s_\zeta} \quad (3-14)$$

where CFL is the Courant-Friedrichs-Lewy number (typically 0.75 and 0.45 for first- and second-order accuracy resp.), λ_ξ , λ_η , and λ_ζ are the maximum eigenvalues in the ξ , η , and ζ grid directions, and s_ξ , s_η , and s_ζ are the cell areas projected in the grid directions.

3.2 Flux Solvers

The flux normal to each surface of cell ijk is found by solving an approximate Riemann problem when given the appropriate “right” and “left” hand states at the cell surfaces. Approximate Riemann solvers, by virtue of their name, approximately solve the one-dimensional Riemann or “shock tube” problem across a one-, two-, or three-dimensional interface or surface. Four approximate Riemann solvers were considered for the present study; the advection upstream splitting method (AUSM) (Liou and Steffen, 1993), van Leer’s flux splitting method (VLFS) (Anderson, Thomas, and van Leer, 1986), Roe’s approximate Riemann solver (RARS) (Roe, 1981), and the solver of Harten, Lax and van Leer (HLL) (Ingram et al., 1993). The “right” and “left” hand states of the conserved variables were found using MUSCL differencing (Anderson, Thomas, and van Leer, 1986) and were transformed (rotated) into a coordinate system relative to the unit normal of the surface in question.

Of the four Riemann solvers mentioned, only AUSM, VLFS, and HLL were considered because of various deficiencies encountered with RARS. The advection upstream splitting method proved to be quite non-dissipative and in fact was too non-dissipative for the Euler equations at times, but has been reported to be quite effective for the Navier-Stokes equations (Welch and Chima, 1993), does not need an entropy fix and can be easily extended to non-ideal gases. Van Leer’s flux-split method is easy to implement, but does not recognize the contact discontinuity and hence is quite dissipative. The Harten, Lax and van Leer method is straight forward, slightly more expensive than AUSM or VLFS (but less expensive than RARS), and is as non-dissipative as RARS without needing an

entropy fix. Roe's approximate Riemann solver is very popular and shown to be accurate, but is quite expensive (order of n_{eq}^2 calculations required to calculate the flux, where n_{eq} is the number of equations considered) and needs parametrized entropy fixes to prevent non-physical solutions.

3.2.1 Advection Upstream Splitting Method

We will not elaborate on VLFS or RARS since they are well known, and will first consider AUSM, the advection upstream splitting method of Liou and Steffan (1993). The uniqueness of AUSM is that it treats the advective and pressure terms in the flux vector separately and thereby recognizes the contact discontinuity. The flux vector, F , can be written as

$$F = \begin{bmatrix} \rho \\ \rho u \\ \rho v \\ \rho w \\ (e + P) \end{bmatrix} u + \begin{bmatrix} 0 \\ P \\ 0 \\ 0 \\ 0 \end{bmatrix} = F^c + \begin{bmatrix} 0 \\ P \\ 0 \\ 0 \\ 0 \end{bmatrix} \quad (3-15)$$

which is split into convective (advective) and pressure terms. Given the "right" (R) and "left" (L) hand states, the flux at the interface, $F_{1/2}$, can be written as

$$F_{1/2} = \frac{1}{2} M_{1/2} \left[\begin{bmatrix} \rho a \\ \rho u a \\ \rho v a \\ \rho w a \\ (e + P) a \end{bmatrix}_L + \begin{bmatrix} \rho a \\ \rho u a \\ \rho v a \\ \rho w a \\ (e + P) a \end{bmatrix}_R \right] \quad (3-16)$$

$$- \frac{1}{2} |M_{1/2}| \Delta_{1/2} \begin{bmatrix} \rho a \\ \rho u a \\ \rho v a \\ \rho w a \\ e + P a \end{bmatrix} + \begin{bmatrix} 0 \\ P_L^+ + P_R^- \\ 0 \\ 0 \\ 0 \end{bmatrix}$$

where $\Delta_{1/2} \{ \} = \{ \}_R - \{ \}_L$. The Mach number at the interface, $M_{1/2}$, is given by

$$M_{1/2} = M_L^+ + M_R^- \quad (3-17)$$

where M_L^+ and M_R^- are given by

$$M^\pm = \begin{cases} \pm \frac{1}{4} (M \pm 1)^2 & \text{if } |M| \leq 1 \\ \frac{1}{2} (M \pm |M|) & \text{otherwise} \end{cases} \quad (3-18)$$

The pressure terms are split according to a second-order polynomial as

$$P^\pm = \begin{cases} \frac{P}{4} (M \pm 1)^2 (2 \mp M) & \text{if } |M| \leq 1 \\ \frac{P}{2} \frac{(M \pm |M|)}{M} & \text{otherwise} \end{cases} \quad (3-19)$$

3.2.2 Harten, Lax, and van Leer Approximate Riemann Solver

The Harten, Lax and Van Leer (HLL) method (Ingram et al., 1993) is a simplified Roe approximate Riemann solver, where the interface flux, F_{lr} is given by

$$F_{lr} = \begin{cases} F_l & S_L > 0 \\ F_{lr}^* & S_L \leq 0 \leq S_R \\ F_r & S_R < 0 \end{cases} \quad (3-20)$$

and where F_{lr}^* is given by

$$F_{lr}^* = \frac{S_R F_l - S_L F_r + S_R S_L (Q_r - Q_l)}{S_R - S_L} \quad (3-21)$$

The wave speeds, S_L and S_R , are *estimated* and are given by

$$\begin{aligned}
S_L &= \min [\lambda_1(Q_l), \lambda_1(Q^{Roe})] \\
S_R &= \max [\lambda_m(Q^{Roe}), \lambda_m(Q_r)]
\end{aligned}
\tag{3-22}$$

where $\lambda_1(Q^{Roe})$ and $\lambda_m(Q^{Roe})$ are the respective smallest and largest eigenvalues of the Roe matrix.

3.3 MUSCL Differencing and Limiters

As alluded to in section 3.2, the “right” and “left” hand states at the cell surfaces must be found before the Riemann problem can be approximately solved. These states are found using what is known as MUSCL differencing which is an acronym for **M**onotone **U**pwind-centered **S**cheme for **C**onservation **L**aws (Anderson, Thomas, and van Leer, 1986). The basic idea of MUSCL differencing is that one uses a high order interpolation of the cell averaged conserved variables, Q , to get the “right” and “left” hand states at cell interfaces, Q_r and Q_l respectively. These states are then used to get the flux at the cell interfaces by using an approximate Riemann solver and the result is a second or third order accurate solution (away from discontinuities). This is in contrast to **F**lux **D**ifference **S**plitting (FDS) where the positive and negative fluxes are calculated at each cell center and then these positive and negative fluxes are either interpolated to a high order at the cell interfaces (for a finite volume scheme) or are central differenced with a second order approximation (for a finite difference scheme).

3.3.1 Basics of MUSCL Differencing

The basic ideal is to interpolate values of Q (the variable Q now means Q_{ijk}) at the cell half point, $j+1/2$, to get the “left” and “right” hand states with higher than first order accuracy. This is most simply done by

$$\begin{aligned}
Q_{j+1/2}^- &= Q_j + \phi_j^- (Q_j - Q_{j-1})/2 \\
Q_{j+1/2}^+ &= Q_{j+1} + \phi_{j+1}^- (Q_{j+2} - Q_{j+1})/2
\end{aligned}
\tag{3-23}$$

where now the + and - superscripts correspond to the “right” and “left” hand interpolated states respectively and ϕ_j^\pm is a switch which controls the order of accuracy, i.e.,

$$\begin{aligned}\phi^\pm &= 0 \Rightarrow O(\Delta h) \\ \phi^\pm &= 1 \Rightarrow O(\Delta h^2)\end{aligned}\tag{3-24}$$

First order solutions are inherently smooth, but oscillations or overshoots can occur near discontinuities when using the second order or higher interpolation, hence a limiting of the interpolated states, Q_r and Q_l can be effected by implementing a spatial variation in ϕ_j^\pm to assure a non-oscillatory solution, i.e., ϕ_j^\pm can have values $0 \leq \phi_j^\pm \leq 1$.

Third order accuracy can be achieved strictly in the one-dimensional case by using an interpolation scheme of the form (shown without a limiter)

$$\begin{aligned}Q_{j+1/2}^- &= Q_j + \frac{1}{4} [(1 - \kappa) \Delta_- + (1 + \kappa) \Delta_+]_j \\ Q_{j+1/2}^+ &= Q_{j+1} - \frac{1}{4} [(1 - \kappa) \Delta_+ + (1 + \kappa) \Delta_-]_{j+1}\end{aligned}\tag{3-25}$$

where

$$\begin{aligned}(\Delta_+)_j &= Q_{j+1} - Q_j \\ (\Delta_-)_j &= Q_j - Q_{j-1}\end{aligned}\tag{3-26}$$

and varying the value of κ changes the order and type of interpolation, i.e.,

$$\begin{aligned}\kappa &= -1 \Rightarrow \text{Fully one sided second order} \\ \kappa &= 1/3 \Rightarrow \text{“Third order” upwind biased} \\ \kappa &= +1 \Rightarrow \text{Second order central differencing}\end{aligned}$$

Having $\kappa = 1/3$ does not give true third order accuracy in two- or three-dimensional calculations, but improvements in smooth solutions have been observed (Anderson, Thomas, and van Leer, 1986).

3.3.2 Limiters

There are many different forms of MUSCL differencing and methods to limit the interpolated values. After trying many methods, two were chosen which achieved non-oscillatory results, but yet gave relatively sharp shock fronts, especially for shocks oblique to the grid.

The first method used is similar to that in Eqn. (3-25) and is known as a minmod limiter (Anderson, Thomas, and van Leer, 1986; Yee, Klopfer, and Montagne, 1988) and is given by

$$\begin{aligned} Q_{j+1/2}^- &= Q_j + \frac{1}{4} [(1 - \kappa) \bar{\Delta}_- + (1 + \kappa) \bar{\Delta}_+]_j \\ Q_{j+1/2}^+ &= Q_{j+1} - \frac{1}{4} [(1 - \kappa) \bar{\Delta}_+ + (1 + \kappa) \bar{\Delta}_-]_{j+1} \end{aligned} \quad (3-27)$$

where

$$\begin{aligned} \bar{\Delta}_+ &= \max[0, \min(\Delta_+ \operatorname{sgn} \Delta_-, b \Delta_- \operatorname{sgn} \Delta_+)] \cdot \operatorname{sgn} \Delta_+ \\ \bar{\Delta}_- &= \max[0, \min(\Delta_- \operatorname{sgn} \Delta_+, b \Delta_+ \operatorname{sgn} \Delta_-)] \cdot \operatorname{sgn} \Delta_- \end{aligned} \quad (3-28)$$

and b is a compression factor with a *largest permissible value* of $b = (3 - \kappa) / (1 - \kappa)$. It was found that the best value for the compression factor in two-dimensional calculations was $b = 1$ when interpolating conserved variables. Problems sometimes were encountered with convergence when using the method of Eqn. (3-27) for steady state solutions due to the fact that it is a non-linear or non-differentiable limiter which resulted in the 2-norm of the residual experiencing a limit cycle.

The second method uses van Leer's differential limiter (Anderson, Thomas, and van Leer, 1986) and is again similar in form to that of Eqn. (3-25) and is given by

$$\begin{aligned} Q_{j+1/2}^- &= Q_j + \frac{s}{4} [(1 - \kappa \cdot s) \Delta_- + (1 + \kappa \cdot s) \Delta_+]_j \\ Q_{j+1/2}^+ &= Q_{j+1} - \frac{s}{4} [(1 - \kappa \cdot s) \Delta_+ + (1 + \kappa \cdot s) \Delta_-]_{j+1} \end{aligned} \quad (3-29)$$

where s is a limiter function and is given by

$$s = \begin{cases} \left(\frac{2\Delta_+ \Delta_- + \epsilon}{\Delta_+^2 + \Delta_-^2 + \epsilon} \right)^\alpha & \text{if } \Delta_+ \cdot \Delta_- > 0 \\ 0 & \text{otherwise} \end{cases} \quad (3-30)$$

where α is a variable which allows one to tune the amount of limiting to the approximate Riemann solver being used (as α increases the interpolation goes to first order faster near discontinuities) and has a value typically close to 1 and $\epsilon \ll 1$ in order to avoid division by zero in smooth regions. Eqn. (3-30) is used so that at extrema $\Delta_+ \cdot \Delta_- \leq 0$ and the interpolation drops to first order.

It was found by the author that Eqn. (3-30) could be significantly improved upon if the following modification was implemented

$$\begin{aligned} s^+ &= \left(\frac{2\Delta_- (\Delta_+ + \Delta_-) + \epsilon}{\Delta_-^2 + (\Delta_+ + \Delta_-)^2 + \epsilon} \right)^\alpha \\ s^- &= \left(\frac{2\Delta_+ (\Delta_+ + \Delta_-) + \epsilon}{\Delta_+^2 + (\Delta_+ + \Delta_-)^2 + \epsilon} \right)^\alpha \end{aligned} \quad (3-31)$$

still assuming that $s^\pm = 0$ if $\Delta_+ \cdot \Delta_- \leq 0$. The use of Eqn. (3-31) gave much sharper shock waves, particularly in the region just after the shock.

3.3.3 Interpolation Using Primitive or Characteristic Variables

MUSCL differencing is not limited to interpolation using only the conserved variables, one can also interpolate primitive variables or characteristic variables instead and then convert the interpolated variable back to conserved variables before using in the approximate Riemann solver. In fact, improvements in the sharpness of shock waves can be realized if primitive variables are used and, in addition, further improvements in the sharpness of shock fronts and convergence rates can be made if characteristic variables are used (Dadone and Grossman, 1992). The vector of primitive variables, V , is given as

$$V = \begin{bmatrix} \rho \\ u \\ v \\ w \\ P \end{bmatrix} \quad (3-32)$$

and the vector of characteristic variables, W , is given by

$$W = \begin{bmatrix} (P + \rho_k a_k u) / (2a_k^2) \\ (P - \rho_k a_k u) / (2a_k^2) \\ \rho_k v \\ \rho_k w \\ \rho - P/a_k^2 \end{bmatrix} \quad (3-33)$$

The conversion from characteristic to primitive variables is done by

$$V = R_k \cdot W \quad (3-34)$$

where the *matrix* R_k is given by

$$R_k = \begin{bmatrix} 1 & 1 & 0 & 0 & 1 \\ a_k/\rho_k & -a_k/\rho_k & 0 & 0 & 0 \\ 0 & 0 & 1/\rho_k & 0 & 0 \\ 0 & 0 & 0 & 1/\rho_k & 0 \\ a_k^2 & a_k^2 & 0 & 0 & 0 \end{bmatrix} \quad (3-35)$$

The subscript k refers to which cell on either side of the interface at $j + 1/2$ the particular variable is to be evaluated at, i.e., if we are calculating $V_{j+1/2}^+$ then $k \Rightarrow j + 1$ and similarly for $V_{j+1/2}^-$, $k \Rightarrow j$. The interpolation using the characteristic and primitive variables can then be accomplished by (Dadone and Grossman, 1992)

$$\begin{aligned}
 V_{j+1/2} &= V_j + \frac{R_j}{4} [(1 - \kappa) \bar{\Delta}_- + (1 + \kappa) \bar{\Delta}_+]_j \\
 V_{j+1/2}^+ &= V_{j+1} - \frac{R_{j+1}}{4} [(1 - \kappa) \bar{\Delta}_+ + (1 + \kappa) \bar{\Delta}_-]_{j+1}
 \end{aligned}
 \tag{3-36}$$

with $\bar{\Delta}_+$ and $\bar{\Delta}_-$ being evaluated using the characteristic variables. Equation (3-29) may also be written similarly to Eqn. (3-36) using primitive and characteristic variables. It was found that with MUSCL interpolation using characteristic variables no significant convergence problems were encountered, but the value of the compression factor, b , still had to be taken as $b = 1$.

3.4 Convergence Acceleration Techniques

The three-dimensional Euler equations are integrated forward in time in an explicit manner while using several techniques to accelerate convergence to steady state. Possible methods include local time stepping, characteristic time stepping (matrix preconditioning methods), multi-stage Runge-Kutta integration (multi-stage schemes), residual smoothing and multigrid. All of these were considered, but only local time stepping, Runge-Kutta integration and residual smoothing were utilized. It should be pointed out that these acceleration methods are also applicable to chemically reacting flows as well as the Navier-Stokes equations.

3.4.1 Runge-Kutta Time Integration

Runge-Kutta time stepping is also known in general as a multistage integration scheme and can be utilized to increase the allowable CFL number and has desirable high frequency damping properties which can help to increase the convergence rate. A standard four-stage scheme (Jameson, Schmidt, and Turkel, 1981) was utilized and is given for each cell ijk as

$$\begin{aligned}
Q^{(0)} &= Q^n \\
Q^{(1)} &= Q^{(0)} - \alpha_1 \Delta t \cdot Res^{(0)} \\
Q^{(2)} &= Q^{(1)} - \alpha_2 \Delta t \cdot Res^{(1)} \\
Q^{(3)} &= Q^{(2)} - \alpha_3 \Delta t \cdot Res^{(2)} \\
Q^{(4)} &= Q^{(3)} - \alpha_4 \Delta t \cdot Res^{(3)} \\
Q^{n+1} &= Q^{(4)}
\end{aligned} \tag{3-37}$$

where the coefficients α_i can be chosen to provide optimal high frequency damping and depend upon the spatial order of accuracy of the MUSCL differencing scheme being used (i.e. what value of κ is used). The optimal coefficients for a four stage scheme for different values of κ are shown below (Van leer, Tai, and Powell, 1989)

Coefficients	Value of κ		
	First Order	$\kappa = -1$	$\kappa = 1/3$
a_1	0.0833	0.1084	0.1666
a_2	0.2069	0.2602	0.3027
a_3	0.4265	0.5052	0.5275
a_4	1	1	1

and the optimal CFL numbers (optimal for convergence, not the absolute maximum allowable) for first, second ($\kappa = -1$), and “third” order ($\kappa = 1/3$) MUSCL differencing are 2.0, 0.9214, and 1.7320 respectively for this 4-stage scheme (these numbers all change for a scheme using a different number of stages and can be found in Van leer, Tai, and Powell, 1989). Local time stepping was used in conjunction with the Runge-Kutta integration scheme to remove the stiffness associated with variations in the local fluid time scales.

3.4.2 Residual Smoothing

Another approach to increasing the convergence rate of an explicit integration scheme is residual smoothing and is usually implemented in conjunction with Runge-Kutta inte-

gration (Jameson and Baker, 1983). This involves an implicit procedure in which the residuals are averaged, thereby increasing the dissipation to the scheme and allows one to use larger values of the CFL number. This averaging has the effect of collecting information from all points in the flow, thus enabling the larger stability bounds. It should also be pointed out that residual smoothing may be implemented in a time accurate solutions (Arnone, Liou, and Povinelli, 1993).

The general method of residual smoothing in one-dimension (Jameson and Baker, 1983) is given as

$$(1 - \epsilon \delta_x^2) \bar{P}_j = P_j \quad (3-38)$$

or

$$-\epsilon \bar{P}_{j-1} + (1 + 2\epsilon) \bar{P}_j - \epsilon \bar{P}_{j+1} = P_j \quad (3-39)$$

where P_j is the unsmoothed residual vector of cell j , \bar{P}_j is the smoothed residual vector and ϵ is a parameter which varies the amount of smoothing. Equation (3-39) is implicit for \bar{P}_j and produces a tridiagonal system which is easily solved. In the simplest implementation of residual smoothing the variable ϵ is given by

$$\epsilon \geq \frac{1}{4} \left[\left(\frac{CFL}{CFL^*} \right)^2 - 1 \right] \quad (3-40)$$

where CFL^* is the maximum CFL number of the unsmoothed scheme and CFL is the CFL number that is desired. In three-dimensions, smoothing is applied in product form as

$$(1 - \epsilon_\xi \delta_\xi^2) (1 - \epsilon_\eta \delta_\eta^2) (1 - \epsilon_\varsigma \delta_\varsigma^2) \bar{P}_{ijk} = P_{ijk} \quad (3-41)$$

and it is still only necessary to solve a sequence of tridiagonal systems and is not very expensive to implement. The smoothing parameters, ϵ_ξ , ϵ_η , and ϵ_ς are given, for example, by (Martinelli and Jameson, 1988)

$$\epsilon_\xi = \max \left\{ 0, \frac{1}{4} \left(\frac{CFL}{CFL^*} \frac{\lambda_\xi}{\lambda_\xi + \lambda_\eta + \lambda_\varsigma} \right)^2 - 1 \right\} \quad (3-42)$$

where λ_ξ , λ_η and λ_ς are the largest eigenvalues in the ξ , η and ς grid directions respectively. This type of smoothing is known as central residual smoothing (C-RS).

In more advanced residual smoothing schemes the residual vector is preferentially smoothed in a direction chosen according to the sign of the characteristic variable of each component of the residual vector which has been transformed to characteristic variables (Blazek et al., 1991). This form of smoothing is known as upwind residual smoothing (U-RS). Still newer techniques hold promise of even larger stability bounds by utilizing an implicit-explicit residual smoothing scheme (Enander, 1993).

The specific form of residual smoothing used in some of the calculations is known as forward-backward residual smoothing (FB-RS) (Zhu, Lacor, and Hirsch, 1993). In FB-RS, Eqn. (3-39) can be factored into the form

$$(1 + \epsilon_f \delta_x^-) (1 - \epsilon_b \delta_x^+) \bar{P}_j = P_j \quad (3-43)$$

where we now have two separate smoothing parameters, ϵ_f and ϵ_b (forward and backward), to utilize. Equation (3-43) is implemented in a two-step procedure as

$$\begin{aligned} -\epsilon_f \tilde{P}_{j-1} + (1 + \epsilon_f) \tilde{P}_j &= P_j \\ (1 + \epsilon_b) \bar{P}_j - \epsilon_b \bar{P}_{j+1} &= \tilde{P}_j \end{aligned} \quad (3-44)$$

For the three-dimensional equations Eqn. (3-43) is written as

$$\begin{aligned} (1 + \epsilon_{f, Lx} \delta_x^-) (1 - \epsilon_{b, Lx} \delta_x^+) P_{ijk}^{(1)} &= P_{ijk}^n \\ (1 + \epsilon_{f, Ly} \delta_y^-) (1 - \epsilon_{b, Ly} \delta_y^+) P_{ijk}^{(2)} &= P_{ijk}^{(1)} \\ (1 + \epsilon_{f, Lz} \delta_z^-) (1 - \epsilon_{b, Lz} \delta_z^+) P_{ijk}^{n+1} &= P_{ijk}^{(2)} \end{aligned} \quad (3-45)$$

where $\epsilon_{f, Lx}$, $\epsilon_{f, Ly}$, $\epsilon_{f, Lz}$, $\epsilon_{b, Lx}$, $\epsilon_{b, Ly}$, and $\epsilon_{b, Lz}$ are the *local* smoothing parameters corresponding to the three different sweeping directions and which can be chosen to give different smoothing schemes depending on the state of the flow (i.e., subsonic/supersonic).

The local smoothing parameters necessary to satisfy stability constraints are given, for example, in the x -direction by

$$\begin{aligned}\epsilon_{f,Lx} &= \frac{1}{2} |(sgn(u) + 1) \cdot \epsilon_f + (sgn(u) - 1) \cdot \epsilon_b| \\ \epsilon_{b,Lx} &= \frac{1}{2} |(sgn(u) - 1) \cdot \epsilon_f + (sgn(u) + 1) \cdot \epsilon_b|\end{aligned}\tag{3-46}$$

where now ϵ_f and ϵ_b are the *global* forward and backward smoothing parameters. The global parameters may be related to each other as

$$\epsilon_b = \tau \cdot \epsilon_f\tag{3-47}$$

where $0 \leq \tau \leq 1$. Another relation which may be used is based on the Mach number of the flow in the direction of smoothing and is given by

$$\epsilon_b = \begin{cases} \left| \frac{u-c}{u+c} \right| \epsilon_f & \text{if } |u| < c \\ 0 & \text{otherwise} \end{cases}\tag{3-48}$$

The forward smoothing parameter must still be found empirically and the optimal value changes with the value of the desired CFL number to be used. Equation (3-48) is the relation used in the present calculations, with $\epsilon_f = 1$ or $\epsilon_f = 0.5$ for first or second order accurate calculations respectively.

FB-RS increases the convergence rate by allowing the use of higher CFL numbers. In general, as the CFL number is increased, the convergence rate does not increase and, in fact, at some point the scheme becomes unstable. There is an optimal CFL number which results in the highest convergence rate, but this must be empirically found.

Using FB-RS in conjunction with Runge-Kutta integration and local time stepping, a reduction in the required computation time by a factor in excess of 2 was realized over pure local time stepping alone (no Runge-Kutta integration).

The numerical simulations performed in the following chapters used the HLL approximate Riemann solver, with the MUSCL differencing technique of Eqn. (3-29) using characteristic variables. Some calculations performed in this desertion utilized residual

smoothing. It was found that residual smoothing was much more difficult to use on highly contorted grids, and as such was not used in computations where the projectile has fins.

Where residual smoothing was utilized with local time stepping, CFL numbers of 7.5 and 5.8 were obtainable for first- and second-order solutions respectively. It was found that if a global time step was utilized, the value of the CFL numbers could be at least double those used with local time stepping.

Typically, a computation proceeded for a fixed number of iterations (time steps) using a first-order solution so that the initial flow transients would not present problems (the initial flow field was initialized to freestream conditions). After this fixed number of time steps, the second-order solution was utilized until the solution converged.

Chapter 4: Ideal 3-D Projectile Flow Field

This chapter presents high spatial resolution tube wall pressure data from experiments utilizing the HITS or inserts in which the projectile is thought to be centered in the tube and therefore allows one to gather clues about the structure of the *ideal* three-dimensional flow field between the projectile and the tube wall. To facilitate the investigation of the ideal flow field, three-dimensional non-reacting inviscid numerical simulations are performed to compare to the experimental results. The combination of experimental data and numerical simulations allows the determination of the general flow structure between the projectile and tube wall and, hence, the effects of the fins on the flow field. In addition, the simulations allow one to determine the approximate pressure distribution on the projectile surface, which, at this time, cannot be measured in the laboratory.

4.1 Subdetonative Experimental Results

During the experimental investigation of flow field between the projectile and the tube wall, eleven experiments were performed with the HITS and another ten were performed using the inserts, all of which were performed with the methane-based gas typically used in the first stage of the ram accelerator, i.e., $2.7\text{CH}_4 + 2\text{O}_2 + 5.8\text{N}_2$ or a non-reacting equivalent, $2.7\text{CH}_4 + 7.8\text{N}_2$. Gas dynamic phenomena in the sub-, trans-, and superdetonative regimes were investigated. All but three experiments were performed with 4-fin projectiles, with 5-fin projectiles comprising the three exceptions. Subdetonative regime experiments with the HITS and inserts were performed to record the tube wall pressure data in an attempt to determine the three-dimensional nature of the flow field. Of

these experiments, four produced adequate results which enabled the determination of the flow field between the projectile and the tube wall. A full listing of all experiments is presented in the Appendix.

The tube wall pressure data from one of the first of such experiments using the HITS with eight transducers placed at two adjacent instrumentation stations (20 mm separation) is shown in Fig. 4-1. The Mach number of the projectile was 4.2 (1540 m/s) or 88% of the C-J detonation speed of the gas mixture which had an initial pressure of 24 atm. The traces show the recorded tube wall pressure (normalized by the freestream value) versus time for each transducer. The traces are numbered and correspond to the orientation diagram placed above, which shows the orientation of the projectile fins relative to the sensors as the projectile passed through the tube section. Every-other pressure trace has been shifted in time such that the data appears as though all the pressure probes were located at the same axial location in the HITS (this was also done for experiments which utilized the inserts).

The initial pressure rise in each trace (going from left to right, or in the direction of increasing time) is due to the reflection from the tube wall of the initial conical shock wave generated by the projectile nose cone. The subsequent pressure variations in each trace are due to further reflections of shock waves between the tube wall and the projectile, disturbances by the projectile fins, and/or the effects of combustion. Ideally, in the subdetonative regime, a normal shock should be stabilized somewhere on the projectile body and should be evident by a step change increase in the recorded tube wall pressure.

The orientation diagram reveals that the fins passed directly over transducers 2, 4, 6, and 8, thus we are able to directly determine their effect on the tube wall pressure which the transducers record as the projectile fins travel directly over them. An outline of a projectile with the correct length relative to the time scale has been placed at the bottom of the pressure traces so that the location of the projectile body relative to the pressure on the tube wall may be shown (assuming steady flow). Traces 2, 4, 6, and 8 reveal that at the point where the projectile fins first encounter the tube wall there is a large pressure rise of over 30 times the freestream value. This is where the flow has most probably stagnated and perhaps may be reacting, thereby creating the large pressure rise. Traces similar to 2, 4, 6, and 8 have been seen in experiments which utilized the standard instrumentation of

the 2 m long tube sections, but since the orientation of the projectile fins relative to the transducer was not known and there usually was only one pressure transducer per instrumentation station, the cause could only be speculated upon. The recorded tube wall pressure in traces 1, 3, 5, and 7 are more typical of what one would see if the projectile were truly axisymmetric in shape, i.e., there are no large pressure spikes with values over 30. At this point it is difficult to determine the cause of the variations in tube wall pressure over the rest of the projectile length, while downstream of the projectile base the variations in recorded tube wall pressure are most probably due to combustion phenomena.

An innovative method to help visualize the tube wall pressure data is shown in Fig. 4-2. This figure represents the recorded tube wall pressure as being proportional to the radial distance from the surface of a tube which represents the tube wall (in a reference frame travelling with the projectile). Every other dark line on the surface of this figure correspond to the pressure traces of Fig. 4-1, and have the correct circumferential orientation, with the lines between actual data having been linearly interpolated in the circumferential direction. The pressure traces from the experiment have been mapped onto a cylinder with the local radius corresponding to the measured tube wall surface pressure. The length of the cylinder corresponds to time or axial position along the tube wall. Another way to think of this figure is as if the projectile were travelling down a very thin, but flexible tube which deforms radially outward proportional to the interior surface pressure, with the radial deformation of the tube being greatly exaggerated. The radial position of the surface between actual data has been linearly interpolated. The surface shading is also proportional to the pressure.

Figure 4-3 shows the same data as that of Fig. 4-2, but has a projectile placed inside the cylinder with the correct axial location and fin orientation. The cylinder has been cut along the centerline of a fin and along the centerline of a channel (the space between adjacent fins) to show the effect of the projectile geometry on the tube wall pressure. The effect of the fin is clearly shown by the large pressure rise at the point where the fin leading surface* intersects with the tube wall.

*The width of the front surface of a fin is not thin compared to the width of a channel and hence is not called a leading edge.

A second experiment was also performed in the subdetonative regime with a four-fin projectile at a Mach number of 4.0 (1440 m/s) or 82% of the C-J detonation speed of the gas mixture, which had an initial pressure of 18 atm. The recorded tube wall pressure data from the eight pressure transducers located at two adjacent instrumentation stations in the HITS are shown in Fig. 4-4. The data is also shown in Fig. 4-5 with the same format as that of Fig. 4-3 for the previous experiment. The data from this experiment is very similar to the previous, but the pressure rises due to the fin is now approximately 40.

One of the experiments with a 5-fin projectile was also performed in the subdetonative regime at a Mach number of 5.3 (1560 m/s) or 89% of the C-J detonation speed of the gas mixture, which had an initial pressure of 28 atm. The recorded tube wall pressure from the eight pressure transducers located at two adjacent instrumentation stations in the HITS are shown in Fig. 4-6. The reconstructed tube wall pressure data in the same format as Fig. 4-3 is shown in Fig. 4-7. The tube wall pressure distribution for the 5-fin projectile is qualitatively the same as that of a 4-fin projectile, except of course for the extra pressure rise from the addition fin.

In an attempt to determine the effects of combustion on the flow field, a projectile was accelerated to the desired sub-detonative velocity in a reacting first stage mixture, and then was transitioned to a non-reacting mixture with the same thermodynamic properties as the reacting one. This was accomplished by simply replacing the oxygen directly with nitrogen, with the resulting mixture of $2.7\text{CH}_4 + 7.8\text{N}_2$. The projectile then coasted through the non-reacting mixture at a Mach number of 3.9 (1410 m/s), where a pair of inserts were placed. The recorded tube wall pressure data from the 16 pressure transducers are shown in Fig. 4-8 (trace 2 is flat due to a faulty transducer). The reconstructed tube wall pressure data is shown in Fig. 4-9. A comparison between the reacting and non-reacting flows can now be made. The peak pressure caused by the fin in the non-reacting experiment is roughly two-thirds to one-half of those recorded in the reacting experiments. This suggests that the flow is reacting in the region where the fin first intersects the tube wall, even in the subdetonative regime. Also notice that the flow field behind the projectile has shock reflections that seem to be quite symmetric about the planes defined by two opposing fins.

Upon closer inspection of the preceding three experiments, there is found to be a pressure rise along the centerline of the channels that is found to be much larger than that pre-

dicted from axisymmetric calculations. For example, shown in Fig. 4-10 is a comparison of the tube wall pressure resulting from an axisymmetric simulation with experimental data from the tube wall along the centerline of a channel (trace 15 from Fig. 4-8). One can see that the second large pressure rise recorded in the experiment is much larger than that computed from the axisymmetric calculation. To help determine the cause of this discrepancy and understand the structure of the entire flow field, fully three-dimensional, inviscid and non-reacting numerical simulations of a projectile with fins were performed.

4.2 Numerical Simulations

In an effort to understand the experimental results of the preceding section, the three-dimensional finite-volume Euler code described in Chapter 3 was developed and utilized to numerically simulate the inviscid, non-reacting flow between the projectile and the tube wall. The flow field behind the projectile was not simulated. It was not desired to precisely model all of the flow physics, such as chemical non-equilibrium, viscous, real gas, and unsteady flow phenomena, but instead to obtain a general idea of the shock structure of the flow. Certainly viscous and chemical non-equilibrium effects are not insignificant, but may be ignored in this instance and still obtain quite useful information.

In all of the numerical simulations the freestream conditions were taken to be at standard conditions, with the ratio of specific heats, γ , taken as 1.365. A second-order accurate solution to the flow field was then obtained. For the fully three-dimensional simulations, only one-eighth of the projectile geometry needs to be simulated, as shown in Fig. 4-11. This geometry is then a 22.5° slice through the axis of the projectile from the centerline of a channel to the centerline of an adjacent fin.

The typical grid used is quite complicated due to the presence of the fin and the fact that a structured grid system is used. In order to capture the flow as it interacts with the flat leading surface of the fin, the grid must be made to follow this surface to the tube wall. This presents a problem in that there is in fact no space between the fin and the tube wall for the grid to continue on. To alleviate this problem, a 1 mm gap has been put between the tube wall and the outer dimension of the fin. The tube is still 38.1 mm in diameter, but now

the outer fin diameter is 36.1 mm. This is shown in Fig. 4-12, which shows a cross section of the grid (a cross plane) at the very end of the projectile. The cross sections of the grid at 1/4, 1/2, 3/4 and 1 projectile length are shown in Fig. 4-13 for a 149x29x29 cell grid in the axial, circumferential, and radial directions respectively. This number of cells is approximately eight times the number used in previous numerical simulations (Hinkey, Burnham and Bruckner, 1992). Elliptic smoothing of the grid has been utilized in order to obtain a more uniform, orthogonal grid spacing.

A numerical simulation of a 4-fin projectile travelling at 1400 m/s (Mach 4.0) was performed to *qualitatively* compare with the data from the three 4-fin experiments of section 4.1. Line plots of the calculated tube wall pressure versus distance along the tube wall for the length of a projectile (153 mm) are shown in Fig. 4-14. Five different line plots are shown which correspond to the tube wall pressure taken at five different circumferential angles from the centerline of a fin to the centerline of the adjacent channel ($\pi/16$ increments in angle). The pressure distribution along the centerline now has the same type of pressure rise as found in the experimental data of Fig. 4-10. The pressure distribution along the centerline of the fin shows a double rise in pressure as a result of the shock system continuing to reflect between the tube wall and the leading surface of the fin. This variation in pressure is not seen in the experiments which utilized a combustible gas, but the data shown in Fig. 4-8, which used a non-reacting gas, does show a hint of the double rise in pressure. This suggests that the gas may be reacting in this region.

Although only one-eighth of the flow field was simulated, the full three-dimensional flow field was reconstructed using symmetry about the tube axis and the planes along the centerline of the channel and fin. The resulting tube wall pressure distribution is shown in Fig. 4-15 with the same format as the experimental data in Figs. 4-2, 4-5, and 4-9. The projectile has been included to give the correct length scale and fin orientation. The pressure rise due to the reflection from the tube wall of the initial conical shock generated by the nose cone is seen. There is a large pressure rise (pressure ratio of approximately 20) where the fin first meets the tube wall. The shock waves generated by the fin seem to intersect at the centerline of the channel. The reflected shocks from the centerline of the channel then seem to reflect again from the fins very near the end of the projectile. The projectile surface pressure distribution is shown in Fig. 4-16 and shows the effects of the

reflected shocks from the tube wall and the fins. The reflection from the tube wall of the initial conical shock reflects from the projectile just upstream of the base of the nose cone and does not interact with the leading surface of the fins. The system of shock reflections generated by the initial conical shock and the shocks from the leading surface of the fin reflect off of the surface of the projectile behind the nose cone/body joint about one-fourth of the way down the length of the body. It has been seen in photographs of projectiles that this is a region where there seems to be soot marks and erosion of the surface.

The same projectile geometry has been simulated at a Mach number of 5.1 (1850 m/s) as a comparison to the Mach 4.0 result. Line plots of the calculated tube wall pressure versus distance along the tube wall for the length of a projectile are shown in Fig. 4-17. Similarly to Fig. 4-14, the five different line plots correspond to the tube wall pressure taken at five different circumferential angles from the centerline of a fin to the centerline of the adjacent channel ($\pi/16$ increments in angle). The pressure distribution along the centerline of the channel at this higher Mach number still has a similar pressure rise found in the experimental data of Fig. 4-10 while the shape of the pressure distribution has changed slightly due to the higher free stream Mach number. The pressure distribution along the centerline of the fin no longer has the double pressure rise, but has a single pressure spike near 25 atm. Three-dimensional plots of the tube wall and projectile surface pressure distribution are shown in Fig 4-18 and Fig. 4-19 respectively. The flow is basically quite similar to the Mach 4 result, but the positions of the shock reflections have been moved towards the rear of the projectile and the pressure rise due to the fin leading surface has risen to a value of approximately 20. A significant difference between the Mach 4.0 and 5.1 flow fields is that the first reflection off of the projectile body by the conical shock which has reflected from the tube wall, occurs downstream of the base of the nose cone. This allows the conical shock which reflected from the tube wall to intersect the leading surface of the fins, which will increase the heat transfer rate significantly at the point of reflection.

In both of the previous numerical simulations, the actual pressure rise where the fin leading surface contacts the tube wall may actually be higher due to the fact that in the numerical simulations there was the 1 mm gap between the tube wall and the fin and the flow Mach number never dropped below Mach 1. In actuality it would be expected that the

flow would stagnate at this point, although the increase in the pressure may not be significantly more due to the expansion of the flow over the sides of the leading surface of the fin.

4.3 Comparison Between Experiment and Simulation

Now that we have both experiments and matching numerical simulations they may be directly compared to each other. The most striking difference between the simulations and the experiments is that the recorded pressure where the fin leading surface contacts the tube wall is significantly higher in the experiments which used a reacting gas than in the non-reacting simulations. At approximately Mach 4 the experimental pressure ratio is near 40 compared to 20 for the numerical simulations. A repeat of the simulation performed at Mach 4.0 was performed with a 0.5 mm fin gap (instead of 1 mm) and the pressure rise due to the fin increased to approximately 35, which is much closer to the experimentally observed values of 30 to 40 atm. One would expect that real gas and viscous effects would help to *decrease* the pressure from the ideal calculated values if the flow were non-reacting. Some of the difference between the experimental and numerically calculated pressure is probably due to the errors in the recorded tube wall pressures discussed in Chapter 1, although if the recorded tube wall pressure was reduced by 25 to 35%, this would still be too high. This lends evidence to the speculation that the flow is reacting where the leading surface of the fin contacts the tube wall. If any combustion is occurring at the contact point between the tube wall and the fin it appears to not affect the flow field too much. The experiment in which an equivalent non-reacting gas was used (Fig. 4-8) shows a pressure rise which is much closer to the numerical simulations and without hence adds weight to the assertion that the gas is indeed reacting in this region of the flow.

The presence of the anomalous pressure rise along the centerline of the channel seen in experiments can now be explained as being a result of the interaction of the shocks generated by the leading surfaces of the fins. These shocks happen to intersect at approximately the same location as one of the reflections of the initial conical shock from the nose

cone. Thus it appears that the reflected shock from the tube wall is higher than would be expected from a truly axisymmetric calculation.

The previous calculations were intended to generate a general knowledge about the ideal three-dimensional flow between the projectile surface and the tube wall. More detailed viscous calculations using an ideal, chemically reacting gas and an unstructured grid are necessary to gain a complete and detailed understanding to the flow field.

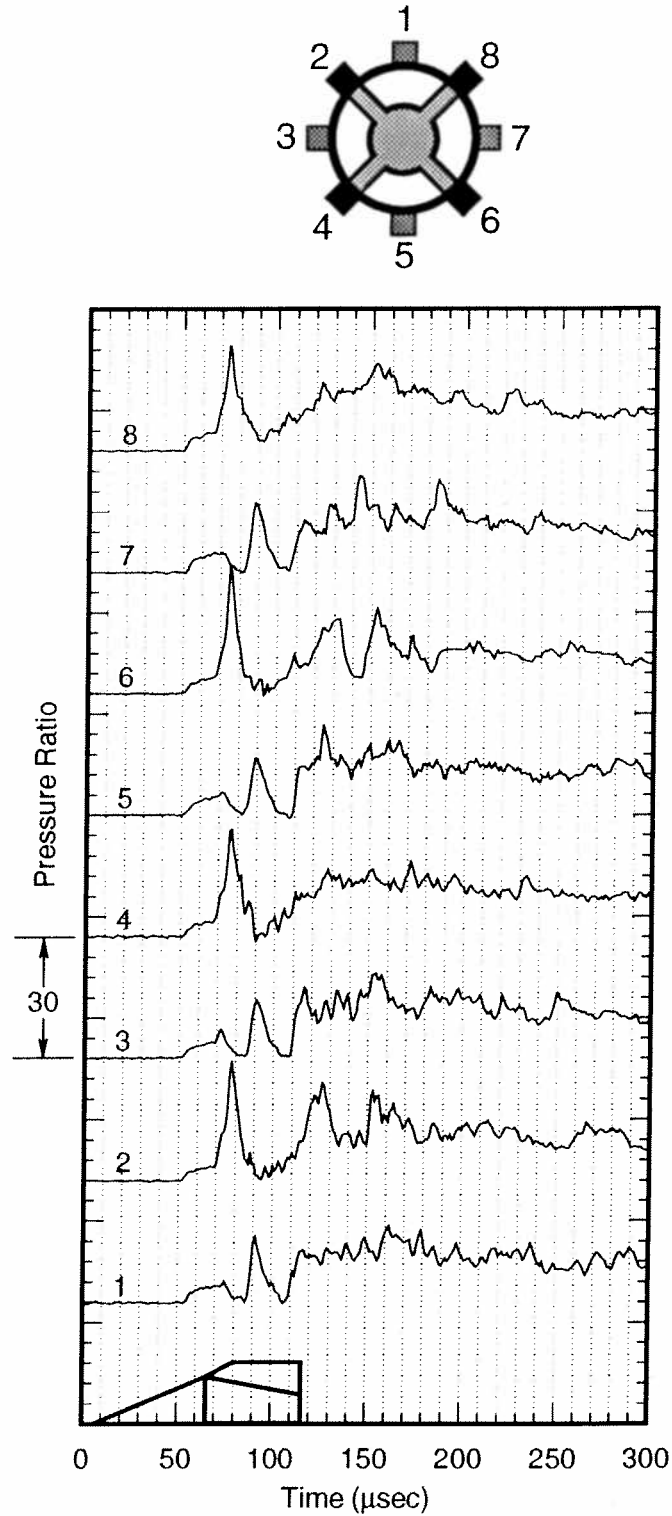


Figure 4-1: Tube wall pressure data from a 4-fin projectile showing the influence of the fins on the flow field. Subdetonative regime, 1540 m/s (Mach 4.2) or 88% of the C-J detonation speed. Gas mixture of $2.7\text{CH}_4 + 2\text{O}_2 + 5.8\text{N}_2$.

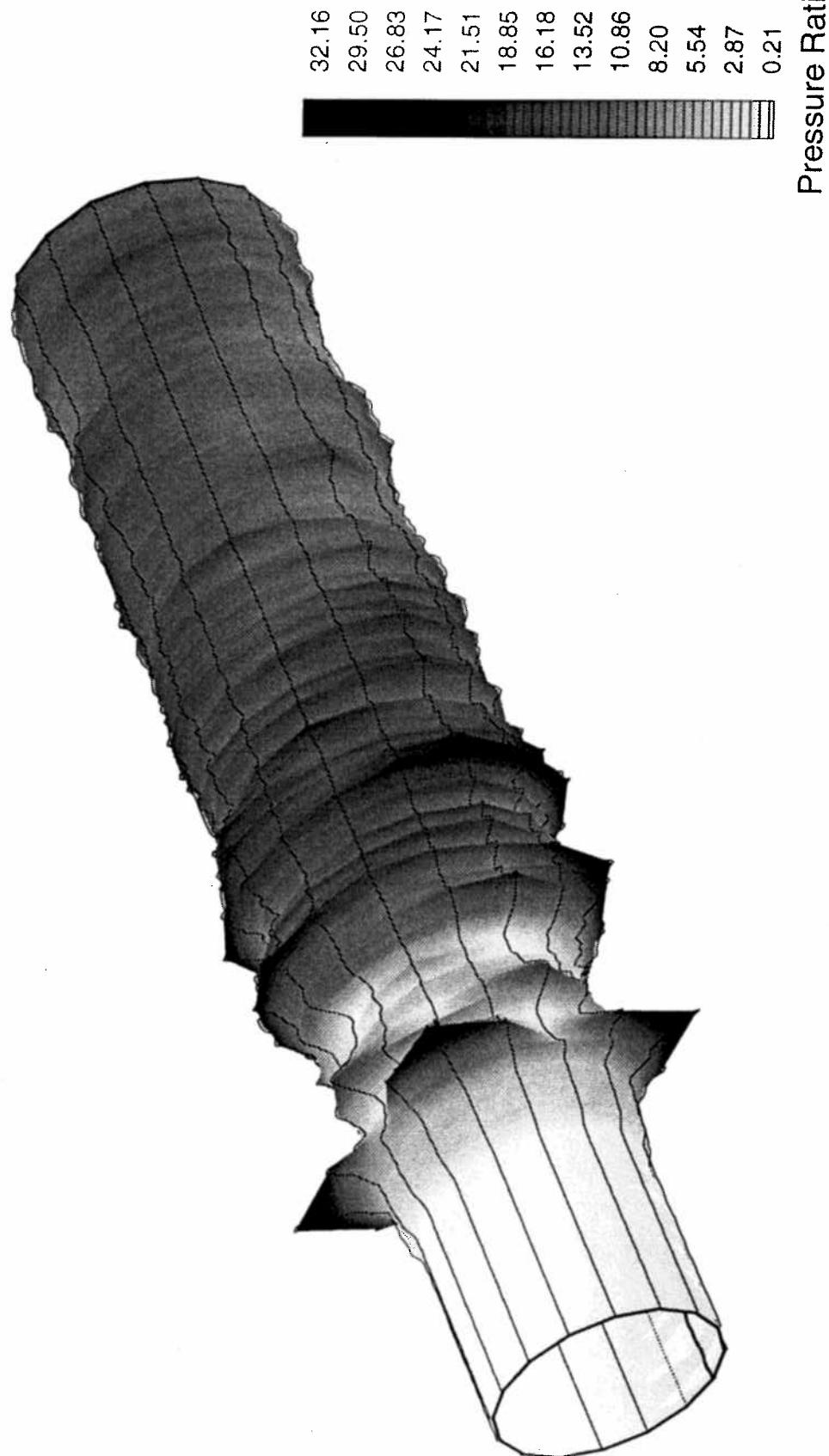


Figure 4-2: Representation of the tube wall pressure from Fig. 4-1 as being proportional to surface shading and radial distance from the surface of a cylinder representing the tube wall. A gas mixture of $2.7\text{CH}_4 + 2\text{O}_2 + 5.8\text{N}_2$, subdetonative regime, 1540 m/s (Mach 4.2) or 88% of the C-J detonation speed.

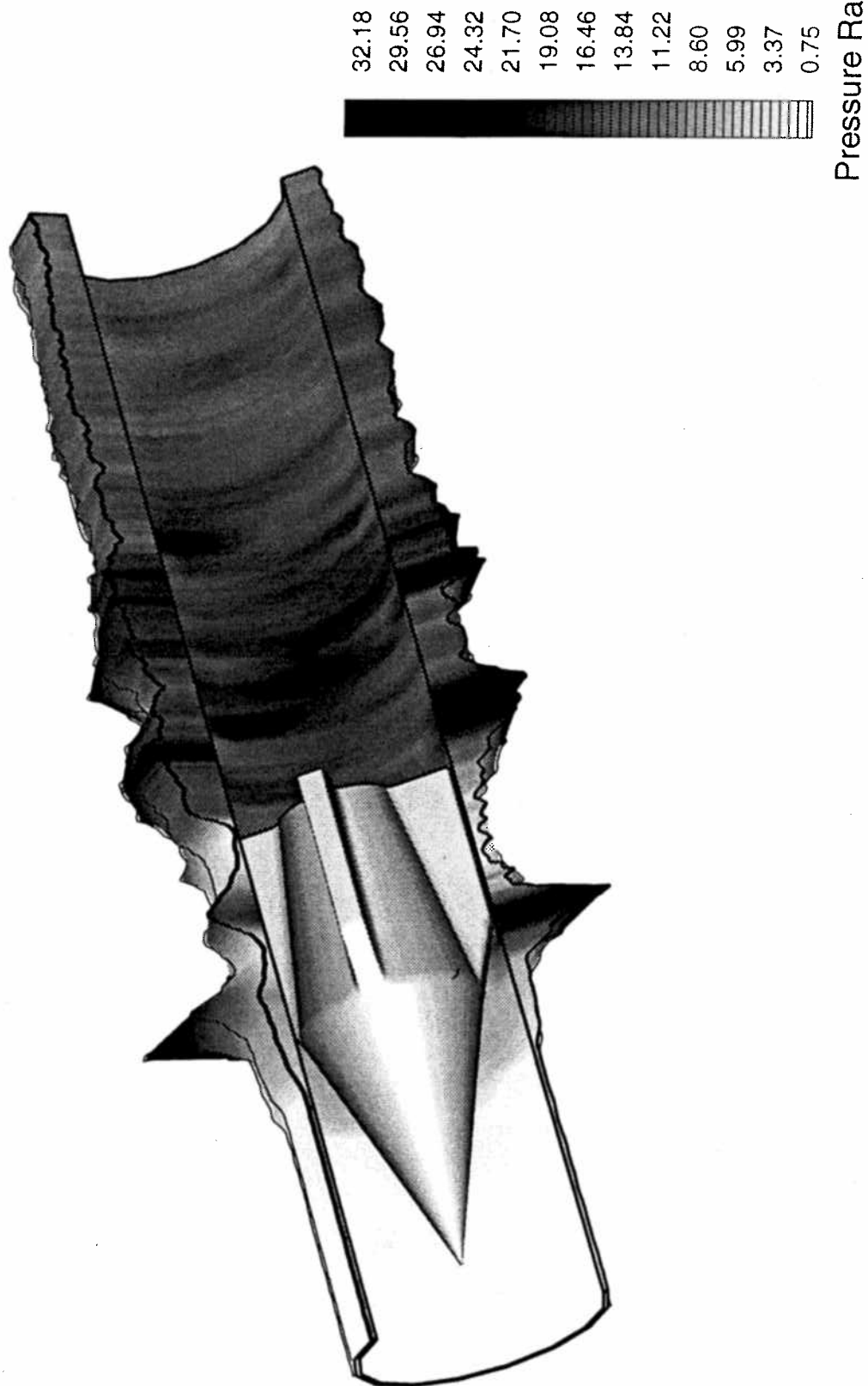


Figure 4-3: Same data as shown in Fig. 4-2, but with the cylinder cut away along the centerline of a fin and along the centerline of a channel (the space between adjacent fins). Projectile shown for fin orientation and scale.

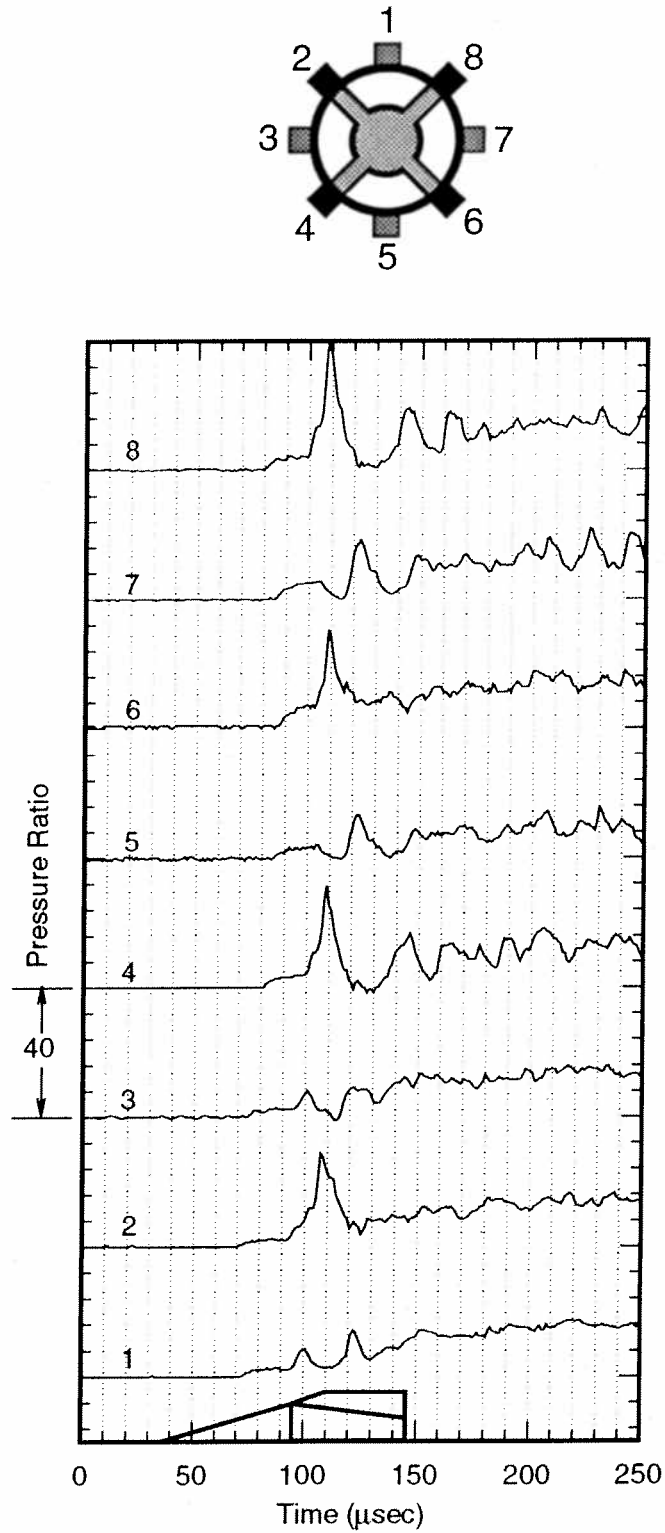


Figure 4-4: Tube wall pressure data from a 4-fin projectile showing the influence of the fins on the flow field. Subdetonative regime, 1440 m/s (Mach 4.0) or 82% of the C-J detonation speed. Gas mixture of $2.7\text{CH}_4 + 2\text{O}_2 + 5.8\text{N}_2$.

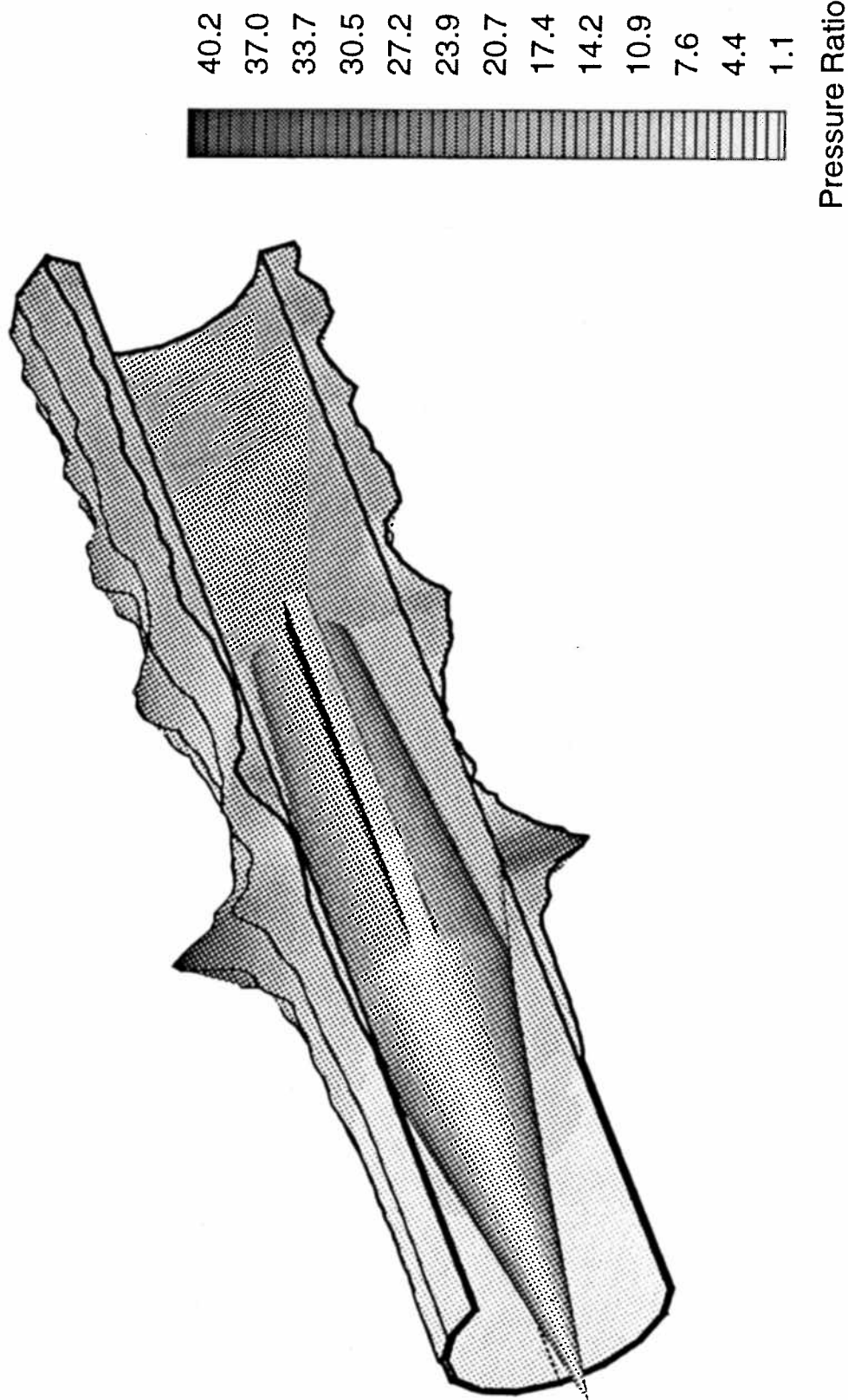


Figure 4-5: Representation of the tube wall pressure from Fig. 4-4 as being proportional to surface shading and radial distance from the surface of a cylinder representing the tube wall. A gas mixture of $2.7\text{CH}_4 + 2\text{O}_2 + 5.8\text{N}_2$, subdetonative regime, 1440 m/s (Mach 4.0) or 82% of the C-J detonation speed. Projectile shown for fin orientation and scale.

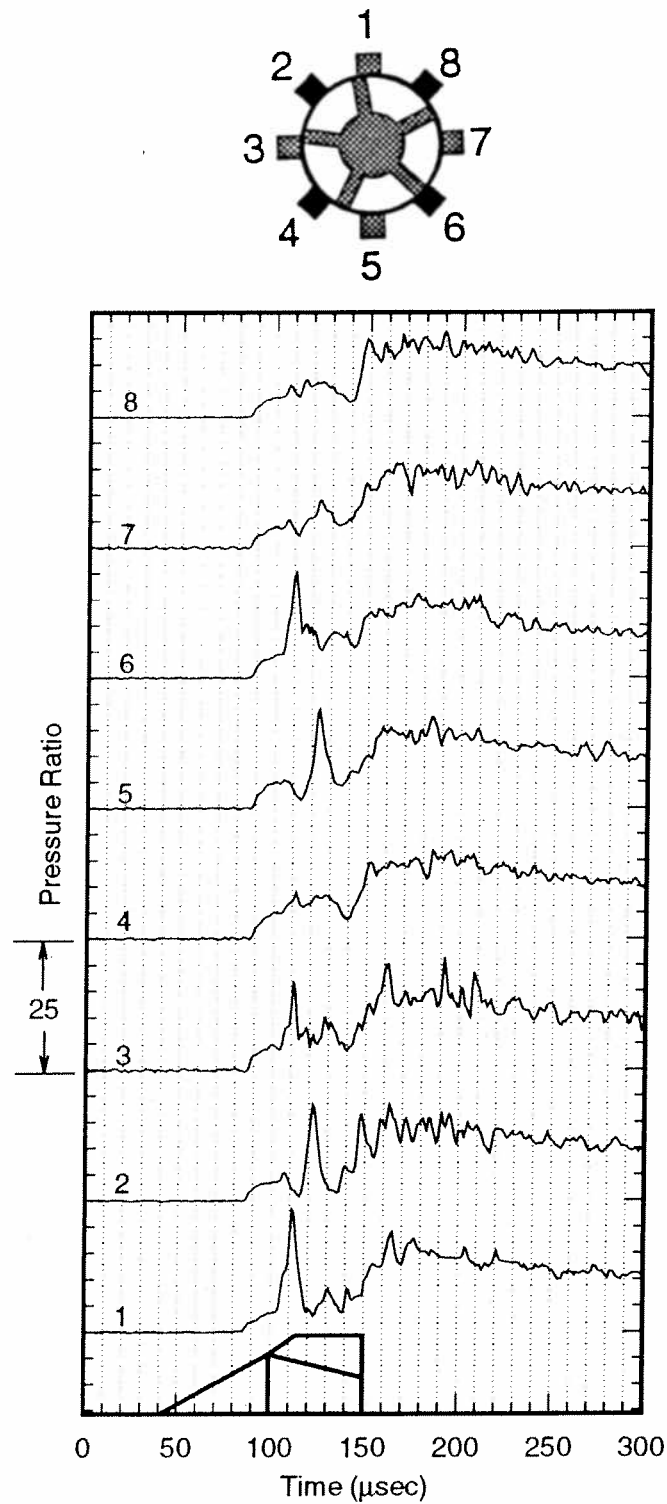


Figure 4-6: Tube wall pressure data from a 5-fin projectile. Subdetonative regime, 1560 m/s (Mach 5.3) or 89% of the C-J detonation speed. Gas mixture of $2.7\text{CH}_4 + 2\text{O}_2 + 5.8\text{N}_2$.

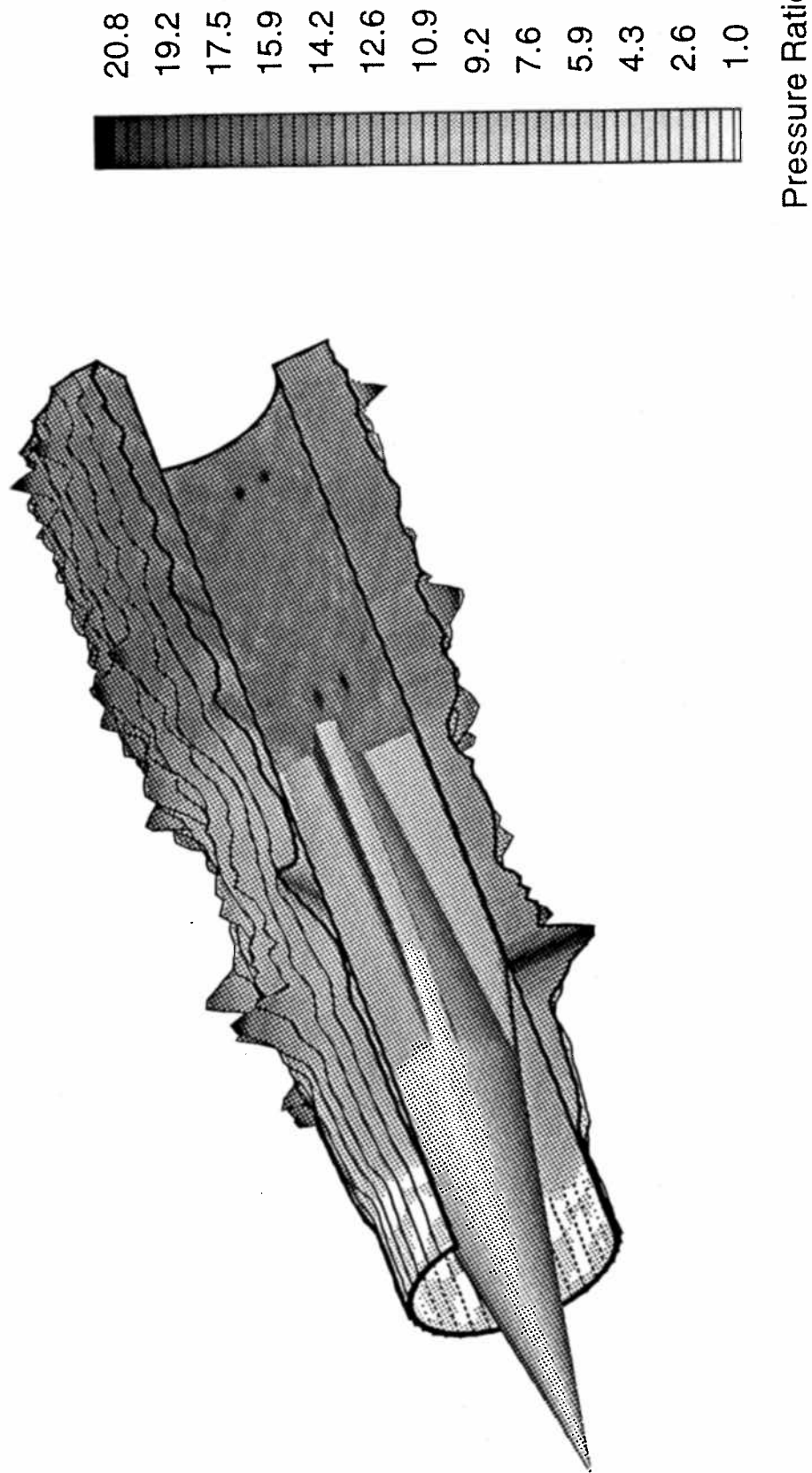


Figure 4-7: Representation of the tube wall pressure from Fig. 4-6 as being proportional to surface shading and radial distance from the surface of a cylinder representing the tube wall. A gas mixture of $2.7\text{CH}_4 + 2\text{O}_2 + 5.8\text{N}_2$, subdetonative regime, 1560 m/s (Mach 5.3) or 89% of the C-J detonation speed. Projectile shown for fin orientation and scale.

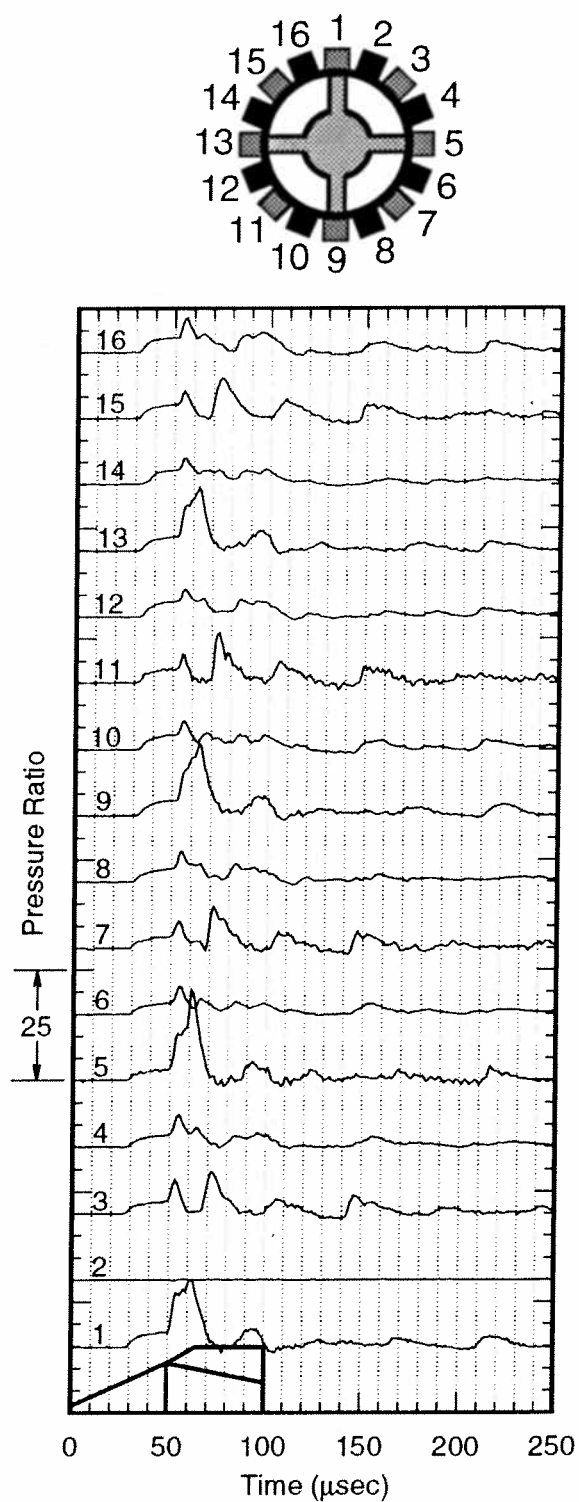


Figure 4-8: Tube wall pressure data from a 4-fin projectile travelling at Mach 3.9 (1410 m/s) or 81% of the C-J detonation speed in a non-reacting mixture of $2.7\text{CH}_4 + 7.8\text{N}_2$. Note the regularity of the shock pattern in the flow behind projectile.

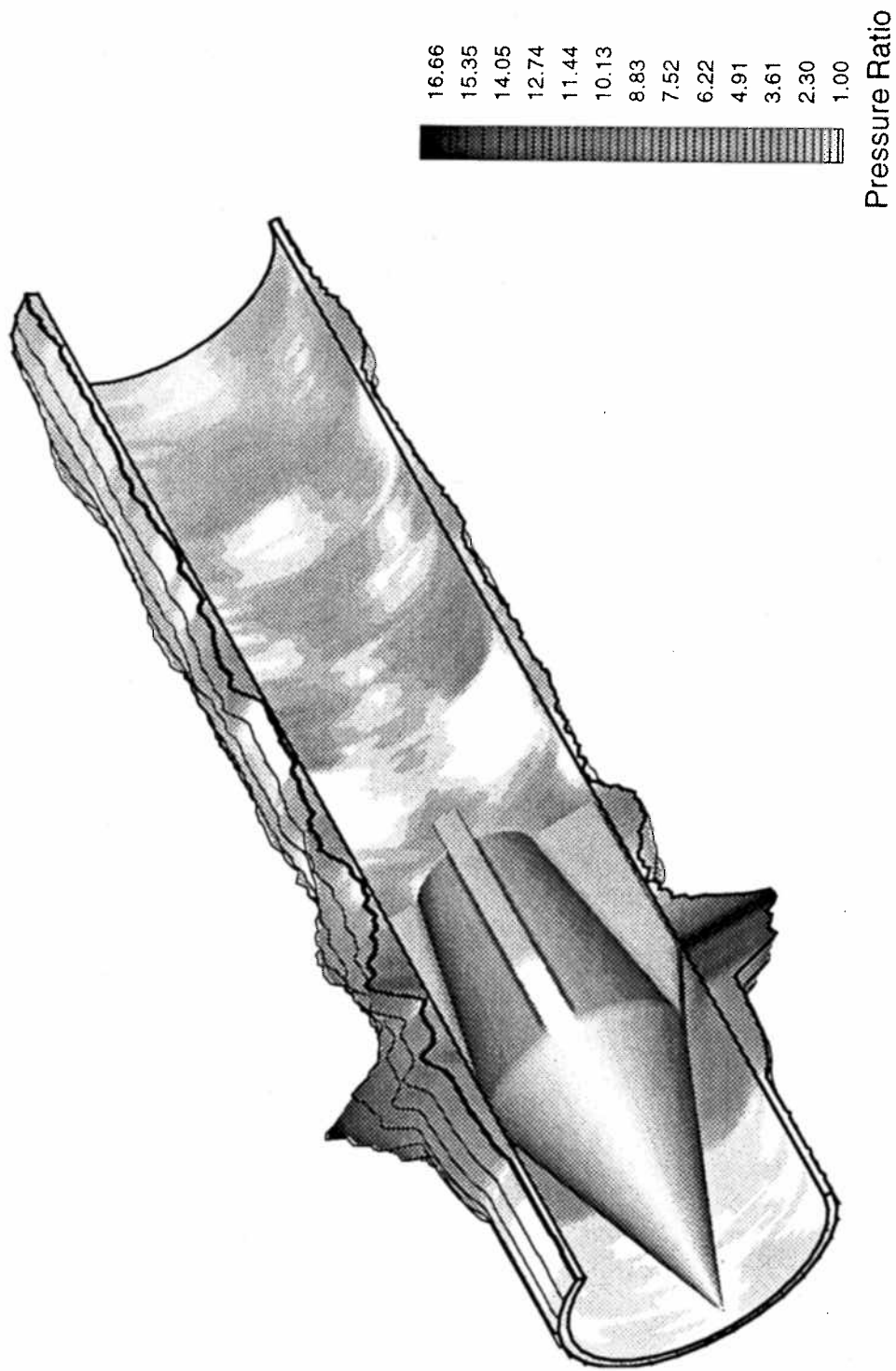


Figure 4-9: Representation of the tube wall pressure from Fig. 4-8 as being proportional to surface shading and radial distance from the surface of a cylinder representing the tube wall. A non-reacting mixture of $2.7\text{CH}_4 + 7.8\text{N}_2$, subdetonative regime, 1410 m/s (Mach 3.9) or 81% of the C-J detonation speed of the equivalent reacting mixture. Projectile shown for fin orientation and scale.

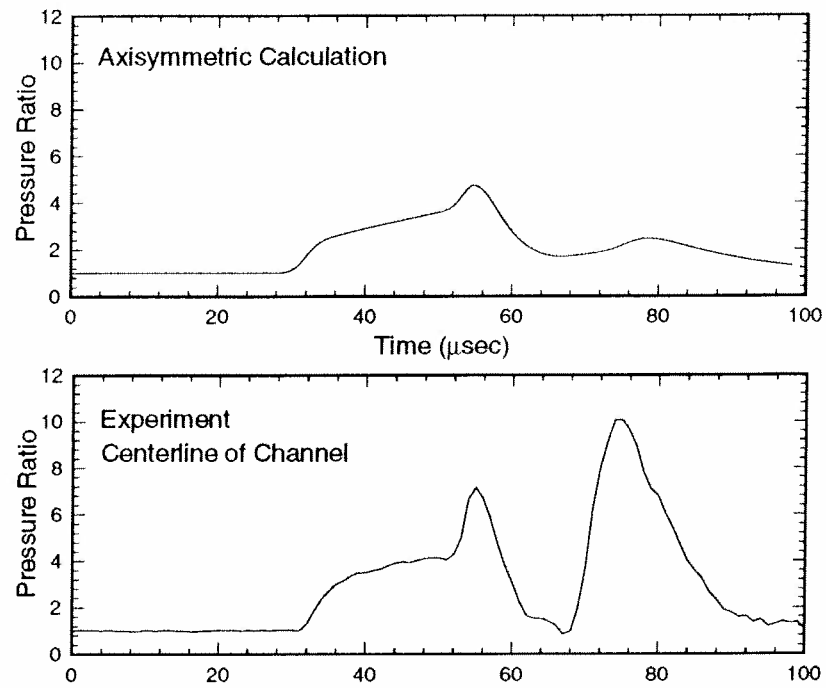


Figure 4-10: Comparison of the experimental tube wall pressure along the centerline of a channel (trace 15 from Fig. 4-8) with that calculated using an axisymmetric simulation.

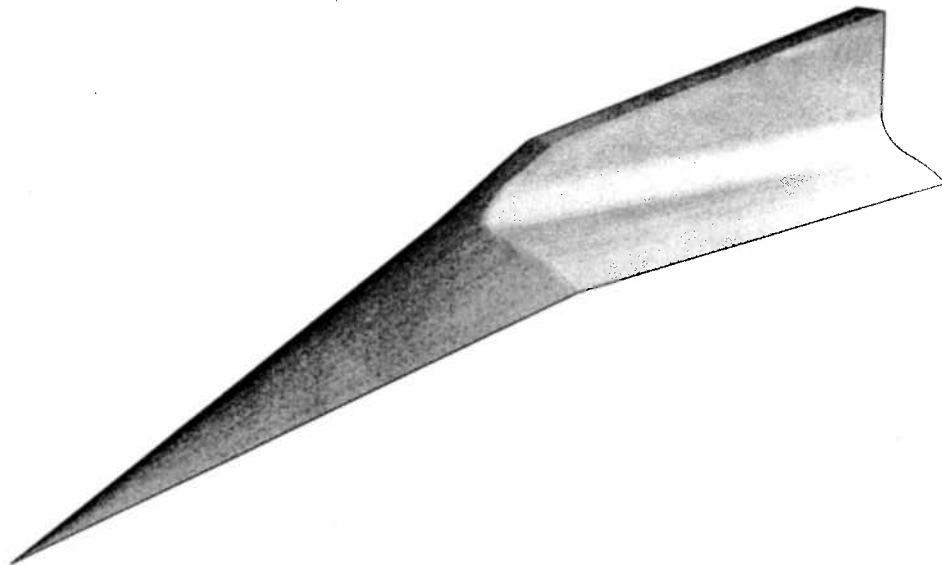


Figure 4-11: Three-dimensional view of the projectile geometry used in the numerical simulations of the ideal three-dimensional flow field.

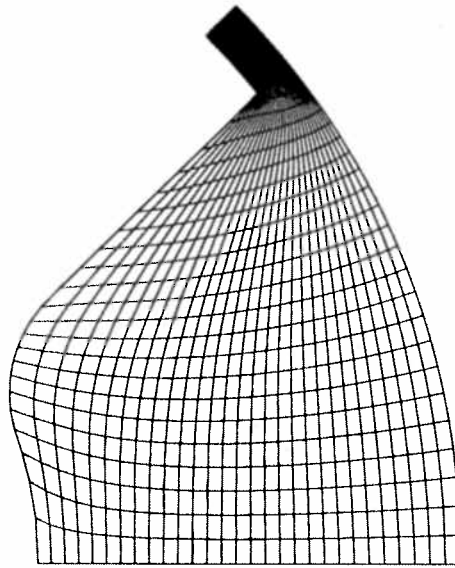


Figure 4-12: Cross plane grid showing the 1 mm gap between the projectile fin and the tube wall.

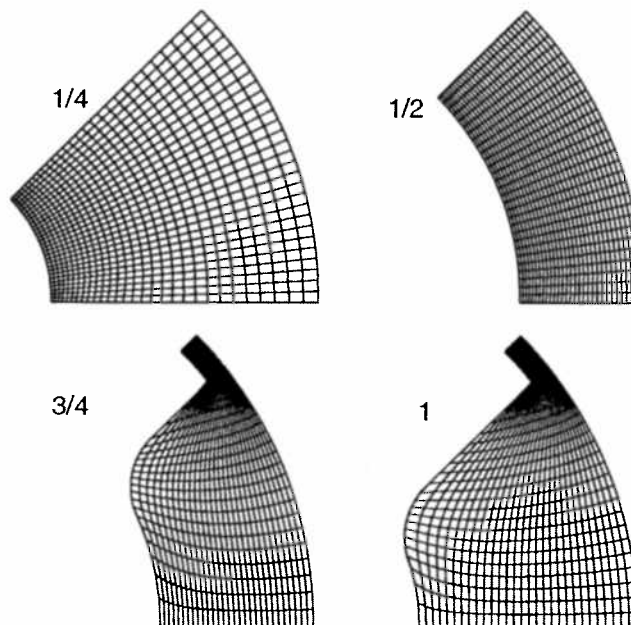


Figure 4-13: Cross plane grids at the 1/4, 1/2, 3/4, and 1 projectile lengths.

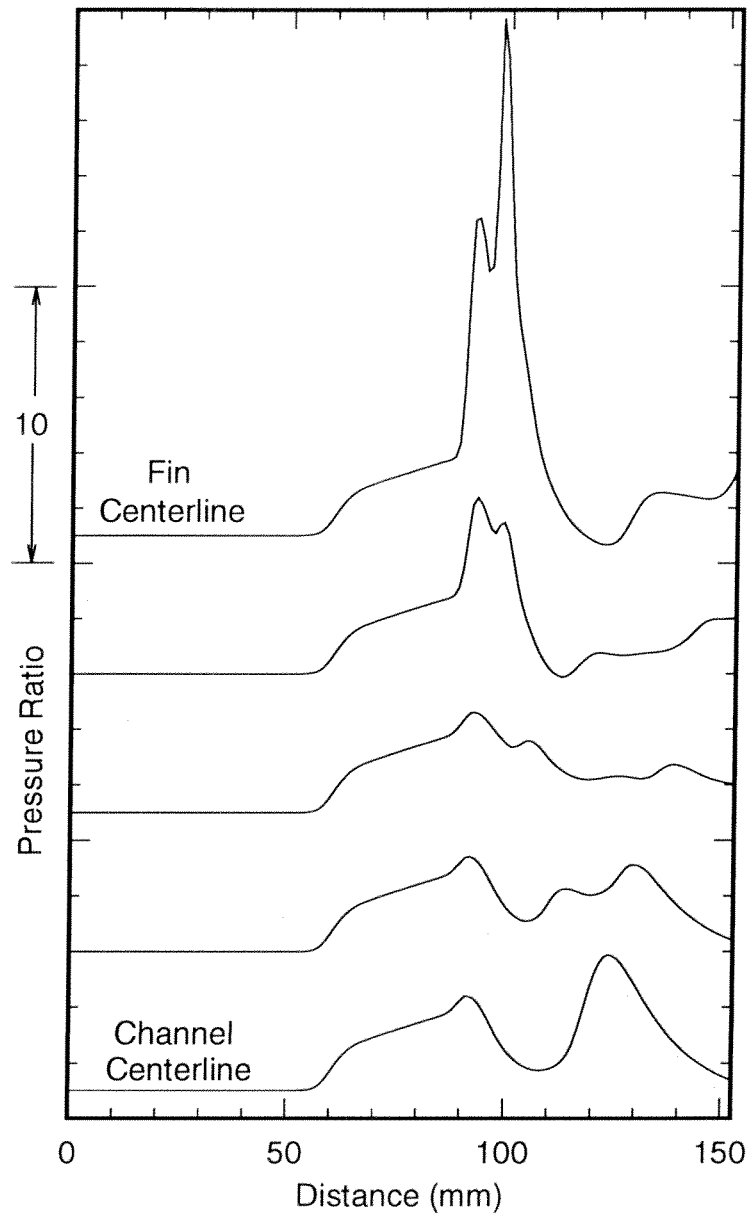


Figure 4-14: Line plots of the calculated tube wall pressure of a 4-fin projectile as a function of distance at 5 different circumferential angles from the centerline of a fin to the centerline of a channel. Projectile velocity of 1400 m/s (Mach 4.0) in a non-reacting mixture of $2.7\text{CH}_4 + 2\text{O}_2 + 5.8\text{N}_2$.

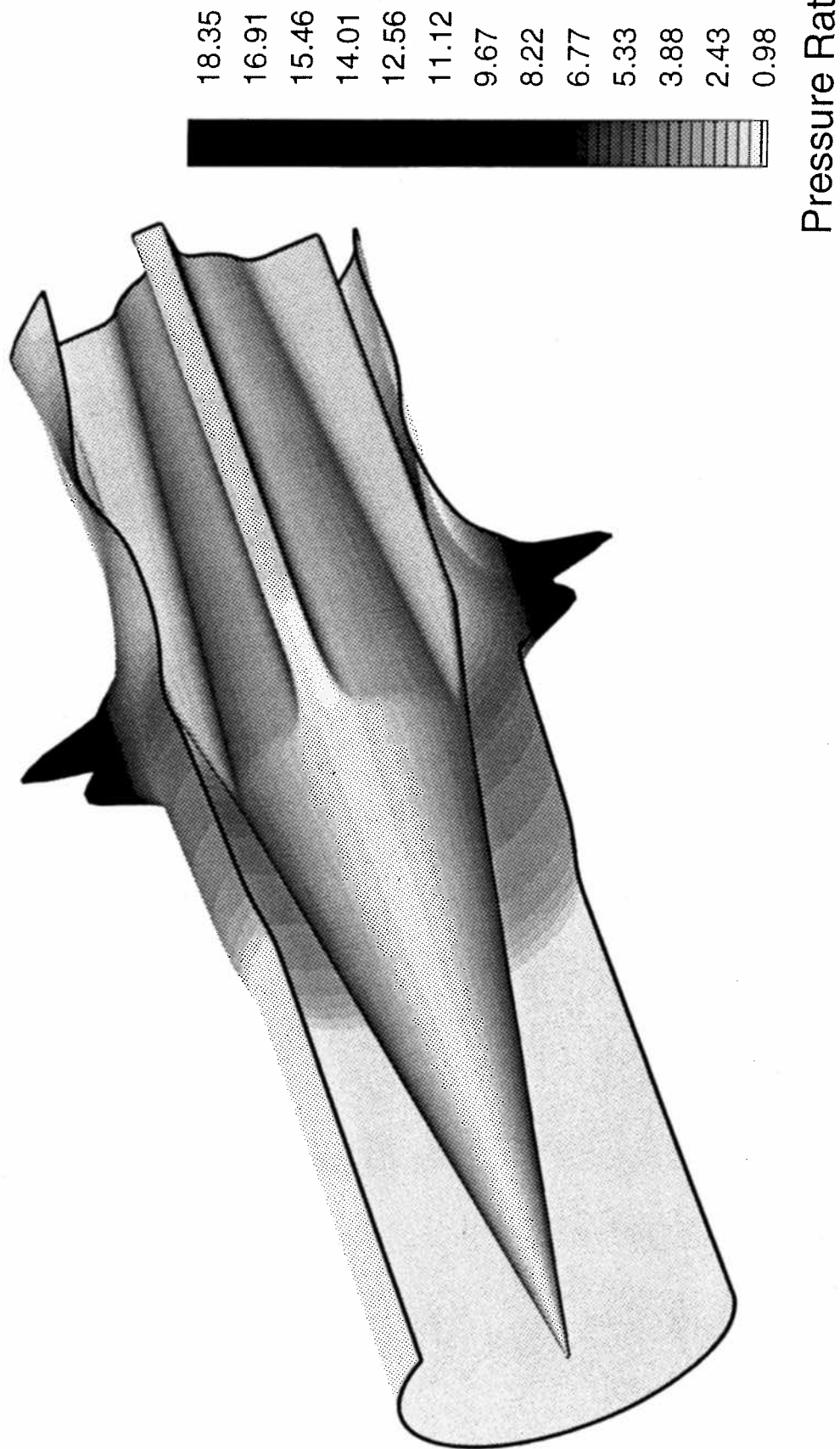


Figure 4-15: Tube wall pressure distribution from the numerical simulation of a 4-fin projectile traveling at 1400 m/s (Mach 4.0) in a non-reacting mixture of $2.7\text{CH}_4 + 2\text{O}_2 + 5.8\text{N}_2$.



Figure 4-16: Calculated projectile body surface pressure distribution of a 4-fin projectile travelling at 1400 m/s (Mach 4.0) in a non-reacting mixture of $2.7\text{CH}_4 + 2\text{O}_2 + 5.8\text{N}_2$.

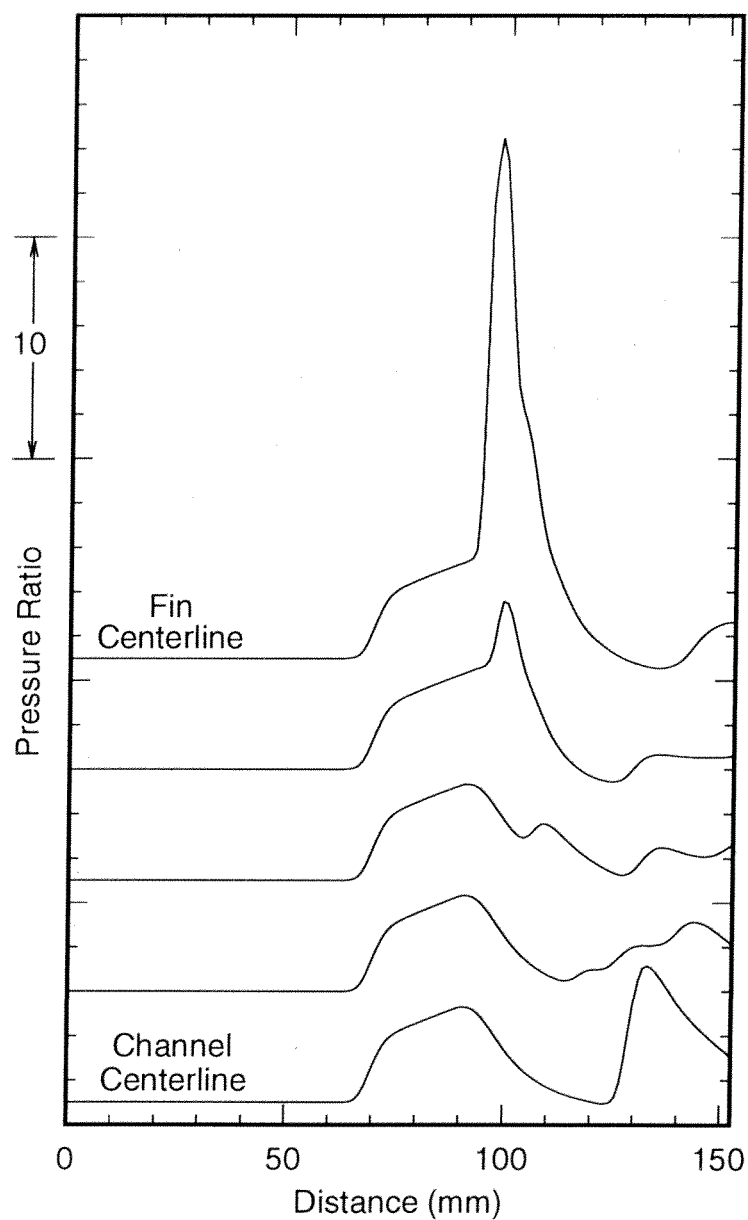


Figure 4-17: Line plots of the calculated tube wall pressure of a 4-fin projectile as a function of distance at 5 different circumferential angles from the centerline of a fin to the centerline of a channel. Projectile velocity of 1850 m/s (Mach 5.1) in a non-reacting mixture of $2.7\text{CH}_4 + 2\text{O}_2 + 5.8\text{N}_2$.

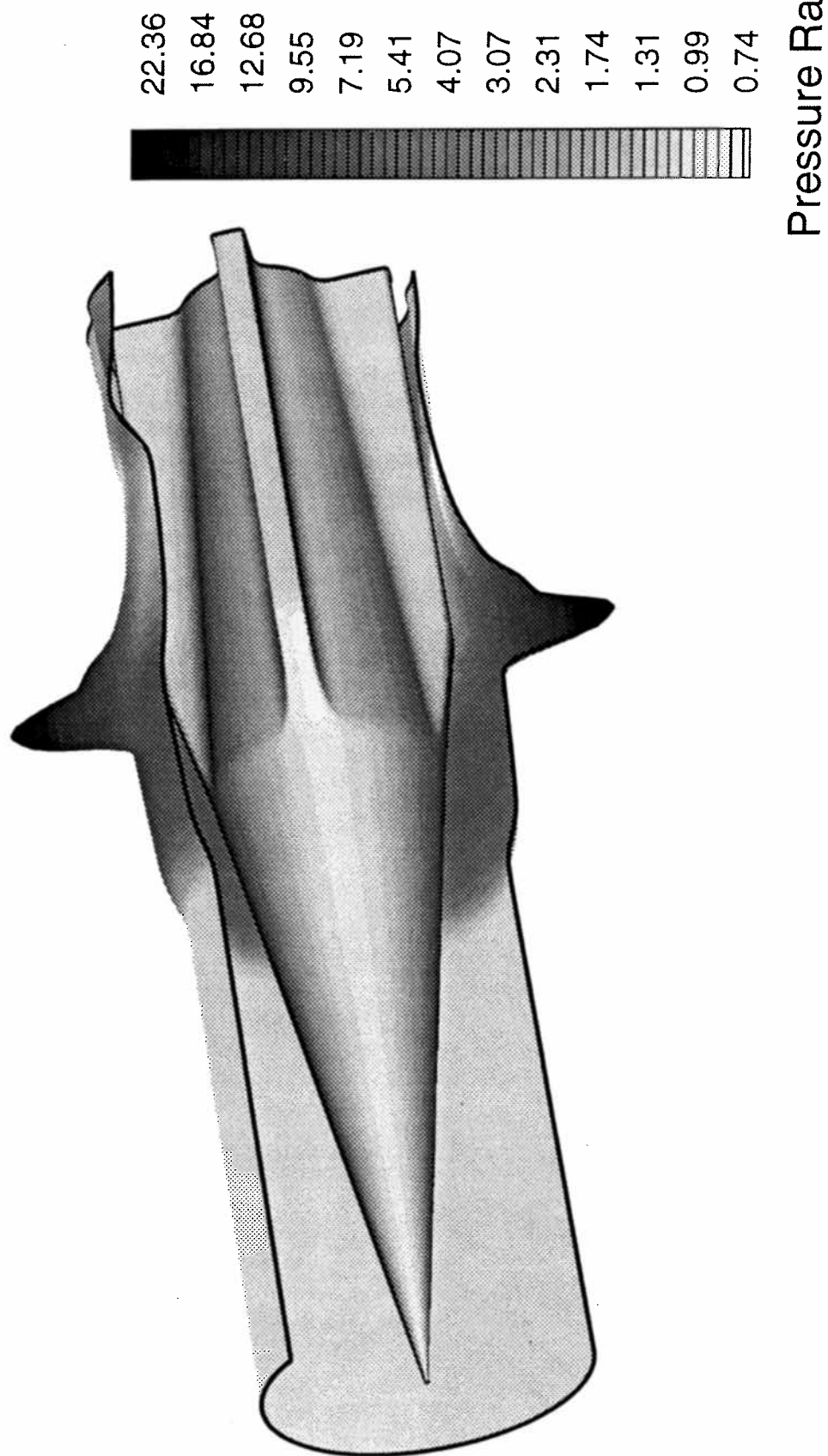


Figure 4-18: Calculated tube wall pressure distribution for a 4-fin projectile travelling at 1850 m/s (Mach 5.1) in a non-reacting mixture of $2.7\text{CH}_4 + 2\text{O}_2 + 5.8\text{N}_2$.

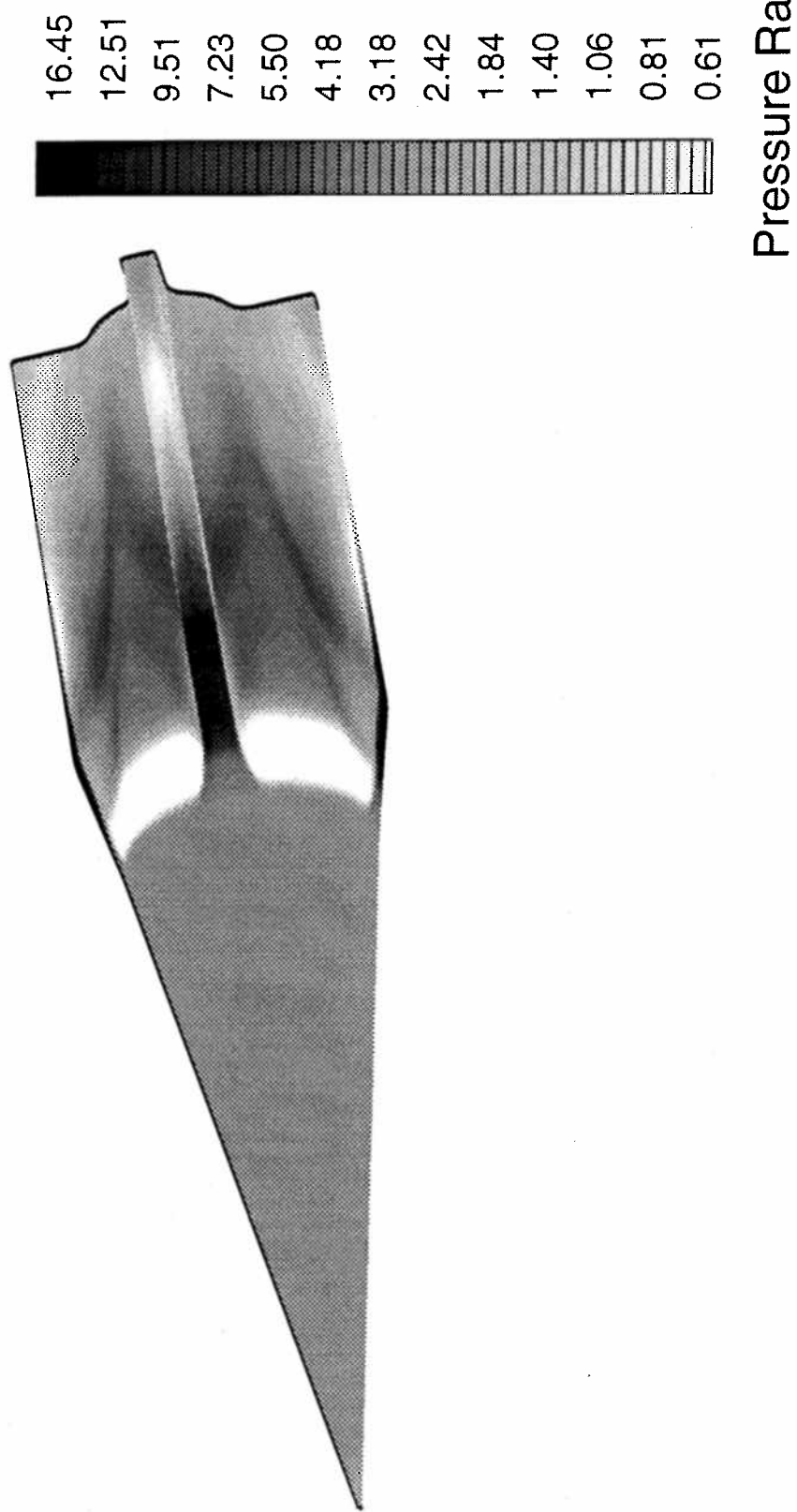


Figure 4-19: Calculated projectile body pressure distribution of a 4-fin projectile travelling at 1850 m/s (Mach 5.1) in a non-reacting mixture of $2.7\text{CH}_4 + 2\text{O}_2 + 5.8\text{N}_2$.

Chapter 5: Non-Ideal 3-D Projectile Flow Fields

This chapter presents data from experiments in the sub-, trans- and superdetonative regimes which exhibit non-ideal or anomalous tube wall pressure data. The idea of projectile canting is introduced along with experimental data which illustrates this phenomenon. Numerical simulations of canted axisymmetric projectiles are performed in an attempt to determine the orientation of the projectile axis with respect to the tube axis. Additional numerical simulations of canted projectiles with fins are then performed to determine the effects of the fins on the flow field. Finally, the implications of the observed and simulated non-ideal flow fields are discussed.

5.1 Experiments Exhibiting Non-Ideal Pressure Records

The experimental data presented in Chapter 4 were chosen because they generally exhibited what was thought to be data from an “ideal” flow field. If the projectile fins pass directly over the pressure transducers, the projectile flow field could be reconstructed using symmetry arguments, but if this does not occur, in general the flow field is difficult to reconstruct. If the recorded tube wall pressure from transducers which are separated by integer multiples of 90° appear to be similar in appearance, the flow field could be assumed to be identical in all four of the channels between the fins. The variation in arrival time and amplitude of the initial conical shock at the tube wall with circumferential position is also an indication of how well the projectile is centered in the tube. In addition, the amount of symmetry in the flow field behind the projectile may also be an indication of the

state of the flow field. Anomalous tube wall pressures were recorded in all the regimes investigated, particularly in the trans- and superdetonative regimes.

The first set of data to be presented which shows anomalous tube wall pressures, is from the subdetonative regime in which a 4-fin projectile travelling at 1400 m/s (Mach 3.9) or 80% of the C-J detonation speed in a reacting mixture of $2.7\text{CH}_4 + 2\text{O}_2 + 5.8\text{N}_2$ at an initial tube fill pressure of 28 atm. The HITS was utilized and the resulting eight pressure traces are shown in Fig. 5-1. The maximum difference in arrival time of the initial shock wave is approximately $7\mu\text{sec}$ (or 10 mm). The orientation diagram at the top of the figure shows that none of the projectile fins passed over any of the transducers, resulting in each channel of the projectile having two transducers recording the tube wall pressure in it. Note that traces 3 and 4, which are in the same channel, indicate that a strong shock (nearly a normal shock) exists very close to the rear of the projectile. However, the other six traces do not indicate this, and in fact show a significant pressure increase just downstream of the throat of the projectile. Traces 3 and 4 indicate "clean" supersonic flow in their respective channel, as indicated by the lower tube wall pressures, which agrees well with the previous numerical simulations of Chapter 4. The effect on a projectile would be a large pressure difference between chambers, resulting in significant lateral forces and perhaps unfavorable aerodynamic moments. This implications of this will be discussed later in section 5.4.

Upon reviewing data from several experiments, another phenomenon was discovered in which the recorded tube wall pressures varied greatly in character from one sensor to the next in the region of flow behind the projectile (i.e., the character of the recorded tube wall pressure varied as one goes circumferentially around the tube). This is quite nicely illustrated in Fig. 5-2(a) and Fig. 5-2(b), where the tube wall pressure traces from two sets of transducers in the HITS are shown for a projectile travelling at 1850 m/s (Mach 5.1) or 106% of the C-J detonation speed with an initial tube fill pressure of 28 atm. One set of eight transducers were in stations b and c, while the other set of eight were 60 mm directly downstream from the first set and were in stations f and g (please refer to Fig. 2-2). The initial conical shock reflection appears to be fairly uniform, but a subtle difference in arrival times of approximately 4 ms (8 mm) is found upon closer inspection. With respect to the character of the pressure traces, one immediately notices that, for instance, traces 3

and 5 in Fig. 5-2(a) exhibit very large pressure variations in the flow behind the projectile, while the remainder of the traces show quite smooth pressure profiles. It was thought that perhaps either the large pressure variations or the smooth traces might have been a result of faulty pressure sensors (the smooth ones being insensitive to pressure variations and/or the others being vibration/shock sensitive). The second set of transducers were originally intended as "backups" for the first set in case a faulty transducer was encountered in the first. Upon inspection of the second set of data it was found, as is evident in Fig. 5-2(b), that they correlate exactly with the first set of data. One can almost correlate each pressure variation between the two sets of data (keeping in mind that the sets of transducers were separated by 60 mm). This set of data and others from similar experiments proved that in fact the large variations in pressure and the smooth pressure traces were caused by real phenomena and were not probe artifacts. The pressure variations are nearly steady relative to the projectile and are most probably related to combustion phenomena, since experiments with non-reacting gases (see Fig. 4-8) did not show a similar kind of shock structure behind the projectile (this will be expanded upon later). One would expect in the ideal case that the pressure traces of Figs. 5-2(a) and 5-2(b) would show some kind of symmetry, i.e., transducers separated by 90° or 180° would have similar pressure profiles because they would be "looking" at equivalent portions of the flow field. This again is not the case. Traces 3 and 5 are separated by 90° and have similar character, but trace 4, which separates 3 and 5, has a very smooth character. So it appears that transducers separated by only 45° have recorded quite dissimilar phenomena which does not systematically repeat itself about the circumference of the tube wall.

In an attempt to study the general flow field and in particular these pressure variations with even greater circumferential resolution, an experiment was performed in the superdetonative regime utilizing the inserts. Figure 5-3 shows the resulting 16 pressure traces from an experiment in which a 4-fin projectile was travelling at 1960 m/s (Mach 5.4) or 112% of the C-J detonation speed with an initial tube fill pressure of 30 atm. The variation in the character of the pressure traces is still present, but now one can see that the pressure variations tend to line up, i.e., a pressure peak tends to occur at the same position (or time) behind the projectile as the corresponding peak in the next trace and similarly with the pressure valleys. There still seems to be a rather abrupt change from a smooth trace to one

exhibiting large pressure variations, suggesting that the scale at which this change occurs is no larger than the circumferential distance between adjacent transducers, approximately 6.5 mm (nearly twice the width of a projectile fin) over a total tube circumference of 120 mm. It is also quite interesting to note that one can not detect any influence of the fins on the flow field, even though the projectile fins passed quite close to transducers 4, 8, 12, and 16.

The initial conical shock reflection appears to be fairly uniform, but a subtle difference in arrival times of approximately 4 ms (8 mm) is found upon closer inspection. The second reflected shock appears to cycle from being noticeable in traces 2 through 15 and disappears in traces 1 and 16 lending further evidence that the projectile is perhaps not centered in the tube.

Figure 5-4 shows the data from Fig. 5-3 in the same format as Fig. 4-2. This format distinctly shows the shock structure of the flow behind the projectile as well as the apparent absence of any influence of the fins on the flow field. The pressure variations behind the projectile seem to form "ring-like" structures.

The 16 tube wall pressure traces from an additional experiment in the superdetonative regime with a 4-fin projectile travelling at 2020 m/s (Mach 5.6) or 115% of the C-J detonation speed with an initial tube fill pressure of 32 atm is shown in Fig. 5-5. In this experiment the inserts were utilized and again the pressure variations behind the projectile appear to line up and, like the previous experiments, the character of the traces changes circumferentially. It was not possible to determine the orientation of the projectile in this experiment (no notches were left in the orientation rings) and no fin effects are distinguishable in the pressure traces.

The initial reflected conical shock wave appears to be fairly uniform with a 5 μ sec (10 mm) difference in arrival time. Again the second reflected shock is evident, but is of a much larger amplitude than in the previous experiment. The strength of the second shock also cycles in amplitude from a pressure ratio of 5 at trace 12 to a pressure ratio of 15 at trace 1, further suggesting that the projectile is not centered in the tube. To aid in the interpretation of the data in Fig. 5-5, the tube wall pressure distribution was reconstructed in the same format used in Fig. 4-2 and is shown in Fig. 5-6. A projectile is shown beside the reconstructed tube wall pressure distribution to provide scale only, since the projectile ori-

entation could not be determined. Note the large pressure of the second reflected shock wave and the variation of its amplitude at different azimuthal locations. The pressure variations behind the projectile are also evident and seem to form distinct structures.

It is also interesting to note that this projectile unstarted* approximately 0.4 to 0.8 m (200 to 400 μ sec) after passing through the pair of inserts. The large amplitude of the second reflected shock may in fact be the signature of a high Mach number unstart mechanism. The large pressure rise due to the second reflected shock in Fig. 5-6 may be the beginning of the unstart of the diffuser as has been similarly seen in starting experiments where the projectile has entered the ram accelerator section at a Mach number too low to start the diffuser (Burnham, 1993). In this case a normal shock is disgorged from the projectile throat and travels in the direction of projectile motion, leaving the flow behind it subsonic and possibly combusting the propellant mixture. In the present experiment the projectile was intact after the unstart and therefore catastrophic structural failure (collapse of the hollow body and nose) did not cause the unstart. A similar pressure rise has also been seen in numerical simulations at velocities significantly above the C-J detonation speed of the mixture and is caused by combustion on the nose cone of the projectile steepening the initial and reflected conical shock waves (Soetrisno, Imlay, and Roberts, 1992). Figure 5-7 shows a comparison of the tube wall pressure distribution from a numerical simulation (Soetrisno, Imlay, and Roberts, 1992) with experimental data from Fig. 5-6. The viscous, chemically reacting numerical simulation is of an axisymmetric projectile travelling at 1840 m/s (Mach 5.0) or 104% of the C-J detonation speed of a mixture consisting of $2.5\text{CH}_4 + 2\text{O}_2 + 5.5\text{N}_2$ at 31 atm initial tube fill pressure. Although the chemistries, velocities, and initial freestream pressures are not identical, the general character of the flow behind the projectile seems to be captured by the simulation. The pressure spike after the first reflection of the conical shock from the tube wall and the pressure variations behind the projectile qualitatively correlate well. The pressure ratios are not directly comparable due to the different Mach numbers of the two cases. The pressure spike after the reflection of the initial conical shock in the numerical simulations is caused by the steep-

*The term "unstart" as used in this text is a generic term for the cessation of ram acceleration due to a shock wave being disgorged from the projectile diffuser. This shock wave may occur for several reasons under various circumstances.

ening of the reflection from the nose cone by shock induced combustion. At higher superdetonative Mach numbers the projectile in the simulation did not unstart, even though the flow completely reacted after the first conical shock, due the high freestream Mach number. This suggests the unstart was initiated by another mechanism.

5.2 Projectile Canting

5.2.1 Definition and Examples of Canted Projectiles

In the previous section, it was shown that the arrival time of the initial conical shock wave varied circumferentially. It is thought that this variation is due to what is known as projectile canting. The projectile is said to be “canted” when the major axis of the projectile is not parallel with the tube axis, resulting in the nose cone of the projectile having a non-zero angle of attack. This situation is illustrated in Fig. 5-8(a-c) where Fig. 5-8(a) shows a projectile with its axis colinear with the tube, Fig. 5-8(b) shows a projectile with its axis parallel to, but not colinear with the tube axis (translated only), and Fig. 5-8(c) with the projectile canted (a combination of rotation and translation).

The phenomenon of canting manifests itself most noticeably in the variation of the time of arrival at the tube wall of the initial shock wave generated by the projectile nose cone. There is also a variation of the magnitude of the reflection from the tube wall of the initial shock over different circumferential angles of the tube wall. The difference in arrival time and reflected shock magnitude is conceptually illustrated by Fig. 5-9, which shows a canted axisymmetric projectile with the resulting difference in arrival time of the initial shock wave and the difference in the magnitude of the resulting tube wall pressure for opposite sides of the tube. It has been generally observed that the circumferential position where the initial shock wave arrives the earliest in time is also where the weakest reflected shock occurs and where the initial shock arrives later in time is where the reflected shock strength is the greatest. Cases which do not exactly exhibit this behavior are thought to be due to the projectile being canted in the tube in a manner which results in no plane of symmetry of the flow.

An experimental example of projectile canting is shown in Fig. 5-10 for a projectile travelling at 1560 m/s (Mach 4.3) or 89% of the C-J detonation speed in a reacting mixture of $2.7\text{CH}_4 + 2\text{O}_2 + 5.8\text{N}_2$. The initial tube fill pressure was 28 atm. Figure 5-10 is a series of line plots of the pressure data from eight transducers placed in the HITS. Traces 3 and 7 show the most variation in arrival time (approximately 19 μsec or nearly 30 mm) and magnitude of the reflected shock pressure ratio (1.5 to 2 for trace 7 as compared to approximately 6 for trace 3). To aid in recognizing these differences the same data as Fig. 5-10 is shown in Fig. 5-11 but with the time scale shortened. The difference in arrival time of the initial shock is accentuated in Fig. 5-11 which has lines from trace to trace connecting the times at which the initial shock waves arrive. The resulting "s" shape is quite distinct. If a projectile were not canted, but was simply translated to one side of the tube, this "s" shape would still persist; however, the initial magnitude of the reflection of the initial conical shock would remain unchanged. This is obviously not the case with the data of Fig. 5-10.

In an effort to study the non-reacting flow field at superdetonative velocities, an experiment was performed in a non-reacting mixture ($2.7\text{CH}_4 + 7.8\text{N}_2$) with a 4-fin projectile which was accelerated using 6 m of reacting mixture, both at 33 atm initial pressure. The projectile velocity was 1920 m/s (Mach 5.3) or 110% of the C-J detonation speed of the equivalent reacting gas as it passed through a pair of inserts. The resulting 16 line plots are shown in Fig. 5-12. Figure 5-13 is the same data as Fig. 5-12, but with the time scale expanded to accentuate the variation in the arrival time of the initial shock wave. It is readily apparent that the projectile is canted in the tube since the arrival time of the shock generated by the nose cone and the magnitude of the reflected shock vary considerably from trace 3 to trace 11. Also, less apparent, is the non-uniformity or lack of symmetry of the shocks in the tube behind the projectile, as compared to those which were shown in Fig. 4-9 (the sub-detonative, non-reacting flow field experiment). There also are no large pressure rises corresponding to the leading surface of the fins, except for the minor pressure spikes in traces 1 and 4 where the projectile fins passed over these transducers as shown in the projectile orientation diagram above the line plots. It was determined that the projectile fins passed over transducers 1 and 4 and hence the projectile was canted

toward transducers 2 and 3. This is possible if the projectile was canted similarly to the projectile shown in the orientation diagram of Fig. 5-12.

It turns out that if one inspects all of the experimental data utilizing either the HITS or inserts, all projectiles are canted by at least a small amount and, in general, as projectile velocities increase, the difference in the axial position where the conical shock initially reflects from the tube wall also increases. The projectile is most likely physically able to cant as a result of the projectile fin geometry being altered by bending due to large, aerodynamically generated, forces and moments, frictional wear, melting and erosion by hot gases or a combination of all three. In its present design (a length to diameter ratio of about four) the projectile is aerodynamically unstable and hence this instability may be the root cause of canting. In fact the subdetonative experiment presented in Fig. 5-1 gives one clue as to the mechanism by which a projectile may initially become canted. The observed pressure difference from channel to channel may not occur at all times, but once having occurred it may pre-dispose the projectile to cant to one side of the tube, possibly for the remainder of the experiment.

5.2.2 Method to Determine Position of Canted Projectiles

As alluded to previously, many experiments seem to show the distinct features of canting, and a method has been developed to determine *approximately* to what degree these projectiles were canted in the tube. Specifically, it is desired to determine the angle of attack of the projectile and its physical position relative to the tube. Through the use of a combination of the Taylor-Maccoll solution for conical flow (Taylor and Maccoll, 1937) and experimental data, the approximate angle of attack of the nose cone (and hence the projectile) and the amount by which the nose tip of the projectile is translated from the centerline of the tube can be *estimated*.

The procedure is based on the assumption that the projectile angle of attack is not large and hence the Taylor-Maccoll solution for determining the cone angle for a given shock angle is approximately valid at all circumferential angles of the cone. It is assumed that the projectile is canted in the tube in such a way as there exists a half-plane of symmetry along the axis of the tube, i.e., it is assumed that the projectile is rotated and translated in a single common plane that defines this plane of symmetry. It is also assumed that the

gas behaves ideally and is calorically perfect (i.e., a fixed ratio of specific heats), with the freestream properties evaluated at standard conditions. The method also depends upon accurate reading of the experimental tube wall pressure data and, hence, the accuracy of the pressure transducers.

The method is implemented as follows: First, the difference in arrival time of the shock from the nose cone is measured at opposing pressure transducers and the maximum value found is used. It is assumed that the transducers which produce the maximum difference in arrival time, together with the tube axis, define the plane in which the projectile is canted. This may not exactly be the case since there is 45° between transducers in the HITS and 22.5° between transducers in the inserts and, hence, the actual maximum difference in arrival time may occur as much as one-half the separation angle from one of these sets of opposed transducers. Next, from this pair of opposing transducers the pressure ratio of the reflected shock wave is measured for each one. This pressure ratio is the pressure *immediately* behind the point where the reflected shock is located, since in conical flow the pressure will continue to rise after the shock has reflected from the tube wall. Schematically this is presented in Fig. 5-14 which depicts a cone travelling supersonically in a tube at an angle of attack with the nose tip translated from the centerline of the tube.

The measured tube wall pressure ratio immediately behind the reflected shock on the side of the cone with the largest effective angle of attack is denoted as P_u (upper wall), while that of the opposite side is denoted by P_l (lower wall) as denoted in Fig. 5-14. The corresponding incident and reflected shock wave angles from the upper and lower walls are denoted by θ_{ui} , θ_{ur} , θ_{li} , and θ_{lr} respectively. The diameter of the tube is denoted by D , the angle of attack of the cone is α , and the amount by which the tip of the nose cone is displaced from the centerline of the tube is Δy .

The amount by which the nose tip of the projectile is translated from the centerline of the tube, Δy , is found by using both θ_{ui} and θ_{li} , the difference in position of arrival of the initial shock wave, Δx , and the geometry shown in Fig. 5-14.

The value of Δx is defined as

$$X_U - X_L = \Delta X \quad (5-1)$$

and from trigonometry X_U and X_L can be related to θ_{ui} and θ_{li} by

$$\tan \theta_{ui} = \frac{D/2 + \Delta y}{X_U} \quad (5-2)$$

and

$$\tan \theta_{li} = \frac{D/2 - \Delta y}{X_L}. \quad (5-3)$$

The previous three equations are then combined to give

$$\Delta y = \frac{\frac{D}{2} (\tan \theta_{ui} - \tan \theta_{li}) + \Delta x \tan \theta_{ui} \tan \theta_{li}}{\tan \theta_{ui} + \tan \theta_{li}}. \quad (5-4)$$

The value of Δx can be found by performing a Galilean transformation where

$$\Delta x = V_{\infty} \cdot \Delta t \quad (5-5)$$

and V_{∞} is the projectile velocity and Δt is the maximum measured difference in the arrival time at the tube wall of the initial shock wave generated by the nose cone of the projectile.

The measured tube wall pressure ratio immediately behind the reflected shock is substituted into the oblique shock relations which are solved for immediately behind the initial and reflected shocks at the tube wall as shown in Fig. 5-15.

The procedure is to first guess an initial value for θ_i and solve

$$\tan(\delta) = 2 \cot \theta_i \left[\frac{M_{\infty}^2 \sin^2 \theta_i - 1}{M_{\infty}^2 (\gamma + \cos 2\theta_i) + 2} \right] \quad (5-6)$$

for δ . Then M_{na} is solved for using

$$M_{na} = \left[\frac{M_{\infty}^2 \sin^2 \theta_i + \frac{2}{\gamma - 1}}{\frac{2\gamma}{\gamma - 1} M_{\infty}^2 \sin^2 \theta_i - 1} \right]^{1/2} \quad (5-7)$$

and then M_1 is found from

$$M_1 = \frac{M_{na}}{\sin(\theta_i - \delta)}. \quad (5-8)$$

The angle θ_r is then solved for using

$$\tan(\delta) = 2 \cot \theta_r \left[\frac{M_1^2 (\sin \theta_r)^2 - 1}{M_1^2 (\gamma + \cos 2\theta_r) + 2} \right] \quad (5-9)$$

in an iterative manner since this is an implicit equation for θ_r . Then M_{nb} is calculated from

$$M_{nb} = M_1 \sin \theta_r \quad (5-10)$$

and $M_{n\infty}$ from

$$M_{n\infty} = M_{\infty} \sin \theta_i. \quad (5-11)$$

The pressure ratios P_1/P_{∞} and P_2/P_1 are then found from

$$\frac{P_1}{P_{\infty}} = 1 + \frac{2\gamma}{\gamma+1} (M_{n\infty}^2 - 1) \quad (5-12)$$

and

$$\frac{P_2}{P_1} = 1 + \frac{2\gamma}{\gamma+1} (M_{nb}^2 - 1) \quad (5-13)$$

The overall pressure ratio P_2/P_{∞} is then the product of the previous two equations, i.e.,

$$\frac{P_2}{P_{\infty}} = \frac{P_2}{P_1} \cdot \frac{P_1}{P_{\infty}}, \quad (5-14)$$

which is in fact what would be measured at the tube wall immediately behind the reflected shock for an initial shock angle of θ_i . The secant method is then used to find a value of θ_i which generates a calculated pressure ratio which matches the measured pressure ratio. This procedure is done for both the “upper” and “lower” walls to get values for θ_{ui} and θ_{li} which are then used in Eqn. (5-4) to obtain Δy .

To determine the angle of attack of the cone, α , we must utilize the Taylor-Maccoll solution that relates the cone half-angle to the initial shock angle, θ_{ui} or θ_{li} , for a given freestream Mach number and ratio of specific heats of the gas. Both θ_{ui} and θ_{li} are used in the Taylor-Maccoll solution to determine separate effective cone half-angles. The known projectile nose cone half-angle, δ_c , are then subtracted from the resulting calculated cone half-angles, δ_u and δ_l , to produce two estimates for the angle of attack of the cone $\delta_u - \delta_c$ and $\delta_l - \delta_c$.

It has been found (and will be shown later) that the angle of attack calculated using the upper wall variables (P_u and θ_{ui}) seemed to produce a better estimate of the cone angle of attack. This may be due to two factors: the breakdown of the assumption that the Taylor-Maccoll solution is valid for the flow on the lower part of the cone as a result of viscous effects and the previously mentioned overshoot in the recorded tube wall pressure. The determination of Δy is more robust since it relies on the oblique shock relations rather than the Taylor-Maccoll solution and the error is largely dependant upon reading the pressure ratios and arrival times of the initial shock from the experimental data.

5.2.3 Estimate of the Degree of Projectile Canting

The first set of experimental data to be analyzed is that which was shown in Fig. 5-10. The maximum difference in arrival time of the initial shock at the tube wall was measured to be 19 μsec . With a projectile velocity of 1560 m/s this is equivalent to a difference in arrival position of the initial shock at the tube wall, Δx , of approximately 30 mm. The measured pressure ratios at the tube wall are $5.5 \leq P_u \leq 6$ and $1.5 \leq P_l \leq 2$ which give incident shock angles of $20.7^\circ \leq \theta_{ui} \leq 21.2^\circ$ and $14.8^\circ \leq \theta_{li} \leq 15.8^\circ$ respectively. These shock angles then give the amount of the nose tip translation as $7.2 \leq \Delta y \leq 8.5$ mm. The uncertainty in the estimate for Δy is approximately ± 0.6 mm. The ranges in uncertainty are derived from the inaccuracies in reading the pressure data and determining exactly when the shock from the nose cone first contacts the tube wall and do not take into account the uncertainty in knowing the plane of canting/translation. The corresponding effective cone half-angles given by the Taylor-Maccoll solution using θ_{ui} and θ_{li} are $14.6^\circ \leq \delta_u \leq 15.2^\circ$ and $6.7^\circ \leq \delta_l \leq 8.5^\circ$ respectively. The corresponding effective cone angles of attack are $4.6^\circ \leq \delta_u - \delta_c \leq 5.2^\circ$ and $-1.5^\circ \leq \delta_l - \delta_c \leq -3.3^\circ$ respectively. So there is a considerable differ-

ence in the calculated angle of attack of the cone depending on whether P_u or P_l is used in the calculation. The more accurate value is probably P_u since the amount of error involved in reading it from the experimental data is much less and the previously mentioned overshoot in the recorded pressures may be less at higher pressure ratios.

The second experiment which exhibited the signs of canting (Fig. 5-12) had a maximum difference in arrival time of the initial shock at the tube wall was measured to be 13 μ sec. At a velocity of 1920 m/s this is equivalent to a Δx of approximately 25 mm. The measured pressure ratios are $6.5 \leq P_u \leq 7$ and $3 \leq P_l \leq 3.5$ which give incident shock angles of $17.4^\circ \leq \theta_{ui} \leq 17.8^\circ$ and $14.1^\circ \leq \theta_{li} \leq 14.7^\circ$ respectively. These shock angles then indicate a nose tip translation as $4.5 \leq \Delta y \leq 6.1$ mm. The corresponding effective cone angles given by the Taylor-Maccoll solution using θ_{ui} and θ_{li} are $12.7^\circ \leq \delta_u \leq 13.1^\circ$ and $8.8^\circ \leq \delta_l \leq 9.5^\circ$ respectively. We see that the corresponding effective cone angles of attack are $2.7^\circ \leq \delta_u - \delta_c \leq 3.1^\circ$ and $-0.5^\circ \leq \delta_l - \delta_c \leq -1.2^\circ$ respectively. Again there is a considerable difference in the calculated angle of attack of the cone depending on whether P_u or P_l is used in the calculation.

5.3 Numerical Simulations of Canted Projectiles

5.3.1 Numerical Validation of the Theory of Projectile Canting

The two experiments described in the previous section have illustrated that projectiles appear to be canted while travelling (either accelerating or coasting) through the tube. To validate the calculated estimates of the projectile orientation and to investigate the flow field of a canted projectile, numerical simulations of the non-ideal (canted) flow fields were performed.

The general geometry initially used to simulate a canted projectile is shown in Fig. 5-16 and represents one-half of the flow field for a three-dimensional axisymmetric projectile without fins. No projectile fins are modelled since only the arrival time and magnitude of the initial reflection of the shock generated by the nose cone are desired and not the influence of the fins which occurs farther to the rear of the projectile. As noted earlier it is assumed that there exists a plane of symmetry along the axis of the tube and that it is the

same plane in which the projectile is rotated and translated. Only one-half of the three-dimensional flow field is solved, although the code is capable of simulating the full flow field if necessary.

To validate the hypothesis that the pressure ratio of the initial reflected shock wave varies over the tube wall for a canted projectile, two test cases were simulated whereby the projectile was either only simply translated or the projectile was fully canted (rotated and translated about the nose tip). For both simulations the gas has the thermodynamic properties of the mixture $2.7\text{CH}_4 + 2\text{O}_2 + 5.8\text{N}_2$ (but is non-reacting) and a Mach number of 4.0 (1450 m/s). Figure 5-17 shows the line plots of the calculated pressure along the upper and lower tube wall (directly opposite each other) for a projectile which is translated by 2 mm toward the bottom of the tube and has a zero angle of attack. A grid consisting of $149 \times 49 \times 49$ cells was used (axial, radial, and circumferential directions). The calculated arrival points of the initial conical shock differ between the upper and lower portion of the tube wall, but the initial magnitude of the reflections are identical, which is not what has been observed in the experiments. The case of true projectile canting is shown in Fig. 5-18 for a projectile with an angle of attack of 4° and the nose tip translated by 5 mm from the centerline of the tube. Note the differences in the arrival position of the initial shock and the initial magnitude of the reflected shock. These line plots are qualitatively similar to the experimental data previously thought to be caused by a canted projectile.

5.3.2 Simulation of Canted Axisymmetric Projectiles

It has now been computationally and experimentally demonstrated that projectiles are indeed canted and not just translated to one side in the tube. This enables a numerical replication of the experimental data with some degree of confidence. With the angle of attack and nose tip translation estimated from the experimental data we can attempt to verify these estimates and investigate the resulting three-dimensional flow field about the projectile nose cone and initial part of the projectile body. In order to utilize the finest computational grid possible in the region of interest only the first two-thirds of an axisymmetric canted projectile are simulated. The general geometry showing the initial two-thirds of the projectile body (without fins) is shown in Fig. 5-19. Some grid clustering is used near the tip of the nose cone to help resolve the conical shock in this region.

The first experimental data which are numerically simulated are that of Fig. 5-10 in which the projectile is again travelling at 1560 m/s (Mach 4.3). It was found that numerical simulations using the angle of attack calculated using P_u gave the best match to the data from the experiment. The values used for the numerical simulation were $\alpha = 4.5^\circ$ and $\Delta y = 7.5$ mm. The line plots of the calculated pressure distributions corresponding to the upper and lower walls are shown in Fig. 5-20 and are compared to the experimental data. The differences in arrival times agree well while the magnitudes of the shock waves are close, but not identical due to the previously mentioned errors in the recorded tube wall pressure (see Chapter 1). This is the best simulation possible without a prohibitive number of numerical iterations on the values of α and Δy . In addition it must be remembered that the transducers used in Fig. 5-10 may not have been exactly in the position where the maximum or minimum reflected shock pressure occurred or where the earliest or latest arrival time of the initial shock occurred (i.e. they may not have been exactly in the plane of symmetry of the canted projectile, but may have been close). In addition there are possible errors in the calibration constants for each probe. With these limitations it is surprising how well the simulation does match up with the experiment. Figure 5-21 shows the computed tube wall pressure distribution and reveals the variation in the arrival position and magnitude of the reflected shock over the tube wall. The surface shading is proportional to the pressure. Figure 5-22 shows the computed surface pressure of the projectile body along with the pressure distribution of the upper and lower symmetry planes between the tube wall and the projectile. Note how the stronger shock on the upper side of the projectile does not get a chance to reflect from the nose cone while the weaker lower shock reflects from the nose cone well ahead of the projectile throat. This may have deleterious effects on performance due to shock/boundary layer interactions and precombustion of the gas in the boundary layer.

The second experiment which was numerically simulated is that of Fig. 5-12 where the projectile was travelling at 1920 m/s (Mach 5.3) in a non-reacting mixture. It was again found that the angle of attack calculated using P_u gave the best match to the data from the experiment. The values used for the numerical simulation were $\alpha = 3^\circ$ and $\Delta y = 6.5$ mm. The line plots of the calculated pressure distributions corresponding to the upper and lower walls are shown in Fig. 5-23 and are compared to the experimental data. Again,

the differences in arrival times agree well while the magnitudes of the shock waves are not well simulated, but can be adequately accounted for by the error in the measured pressure caused by the overshoots discussed in Chapter 1. Figure 5-24 shows the computed tube wall pressure distribution and reveals the variation in the arrival position and magnitude of the reflected shock on the tube wall. Figure 5-25 shows the computed surface pressure of the projectile body along with the pressure distribution of the upper and lower symmetry planes between the tube wall and the projectile. As in the previous simulation shown in Fig 5-22 the stronger shock on the upper side of the projectile does not get a chance to reflect from the nose cone while the weaker lower shock reflects from the nose cone well ahead of the projectile throat. Again, this may have deleterious effects on performance due to shock/boundary layer interactions and precombustion of the gas in the boundary layer.

The two preceding numerical simulations assumed an inviscid, non-reacting flow field and it is quite surprising how well the simulations compare with the experiments. In reality the chemically reacting shock/boundary layer interaction on the surface of the nose cone will have significant effects, especially in the superdetonative regime. A repeat of these two calculation using a fully reacting Navier-Stokes code would be quite interesting, especially for the super-detonative experiment (assuming the flow for that experiment was reacting), since it would be able to determine if it is this viscous interaction which is responsible for the high Mach number unstarts of projectiles that occur in single stage mixtures.

5.3.3 Simulation of Canted Projectiles Including Fin Effects

The previous numerical simulations did not include fin effects since the projectile bodies were assumed to be axisymmetric in an attempt to verify the orientation of the projectile body relative to the tube. To determine the effects of fins on the flow field of a canted projectile, we now attempt to repeat these numerical simulations, but now the projectiles will have fins. To accomplish this one must know the orientation of the projectile fins relative to the plane in which the projectile is canted. This may be determined by inspection of the projectile fin orientation diagrams associated with each experiment.

In general one would expect that simulations of canted projectiles with fins must be done for the full 360 degrees of the tube, which would be quite an expensive simulation in

three-dimensions. This, as it turns out, is not necessary if one realizes that for the two experiments considered, the plane of canting occurs along the centerline of a channel (this seems to be true in general also). In the case of the subdetonative experiment, the projectile is canted towards transducer 7 (see Fig. 5-10, it has the earliest arrival time of the conical shock) and for the non-reacting super-detonative experiment the projectile is canted towards transducers 2 and 3 (see Fig. 5-12). This enables one to assume a plane of symmetry along the centerline of a channel, thus it is necessary to simulate only one-half of the tube, making the numerical problem much more tractable with respect to computation time and memory requirements.

There is another consideration which must be dealt with concerning the geometry of the fins of a canted projectile. In the simulations of the ideal flow field of Chapter 4, the gap between the fin and the tube wall was assumed to be 1 mm. For a canted projectile, if the fins keep their original dimensions, in particular their outer diameter, the fins would extend beyond the tube wall. In the experiments the fins are either bent, worn away or a combination thereof, which allows the projectile to cant. In the numerical simulations it will be assumed that the fins are only worn, not bent, and the 1 mm gap between the fin and the tube wall is maintained. This assumption also implies that the fin is not farther away from the tube wall, except in the case where the original fin outer diameter is pulled away from the tube wall due to the canting. This assumption precludes any wear on the fins due to a previous canting position, which may be the case for a projectile which is "balloting" in the tube.

The geometry for the simulations of the subdetonative experiment (Fig. 5-10) is shown in Fig. 5-26 and illustrates how the upper fin has been reduced in outer diameter to keep the 1 mm gap between the fin and the tube wall. The reduction in the outer diameter is most notable at the rear of the projectile for the upper fin. The lower fin was not reduced in outer diameter for it did not contact the tube wall (even if the 1 mm gap was removed). This suggests that either the projectile is in the process of balloting across the tube or it is being forced to one side of the tube, as shown in Fig. 5-26, by the pressure distribution on the surface of the projectile and/or by inertial forces (from the acceleration of the projectile). The calculation was accomplished with a 149x119x29 cell grid in the axial, circumferential and radial directions respectively.

The resulting calculated tube wall pressure distribution is presented in Fig. 5-27 with the surface shading being proportional to the pressure ratio. The upper and lower figures have been rotated along the axial direction so that both the upper and lower wall pressure distributions can be seen. Note that the pressure rise due to both fins is clearly seen with the upper fin producing a larger pressure rise than the lower fin. Also the non-uniformity of the initial shock wave is the same as the canted axisymmetric projectile calculations. The projectile surface pressure distribution is shown in Fig. 5-28 with the surface shading proportional to the calculated pressure ratio. As in the previous calculations with the canted axisymmetric projectile, the shock wave reflects from the nose cone on the lower wall. The flow between the fins is now more complicated than in the ideal case (non-canted or centered). The shock waves which reflect off of the body are now asymmetric with respect to the centerline of any of the channels. A set of five line traces of the tube wall pressure which have approximately the same angular position as those from the experiment of Fig. 5-10 is shown in Fig. 5-29. The characteristic "s" shape is quite evident, although the influence of the fins is much greater in the calculation than in the experiment. This may be due to the fin gap being much greater than the 1 mm used in the simulation.

The geometry for the simulation of the superdetonative experiment (Fig. 5-12) is shown in Fig. 5-30. As for the geometry for the subdetonative calculation, the reduction in the outer diameter is most notable at the rear of the projectile for the upper fin. The lower fin was also not reduced in outer diameter for it did not contact the tube wall (even if the 1 mm gap was removed). This again suggests that either the projectile is in the process of balloting across the tube or it is being forced to one side of the tube, as shown in Fig. 5-30. The calculation was accomplished with a 149x119x29 cell grid in the axial, circumferential and radial directions respectively.

The resulting calculated tube wall pressure distribution for the superdetonative experiment is presented in Fig. 5-31 with the surface shading being proportional to the pressure ratio. The upper and lower figures have been rotated along the axial direction so that both the upper and lower wall pressure distributions can be seen. Note that the pressure rise due to both fins is clearly seen with the magnitude of the pressure rise being approximately equal, although the shapes of the pressure distributions are very different. Also the non-uniformity of the initial shock wave is the same as the canted axisymmetric projectile cal-

culations. The projectile surface pressure distribution is shown in Fig. 5-32 with the surface shading proportional to the calculated pressure ratio. As in the previous calculations with the canted axisymmetric projectile, the shock wave reflects from the nose cone on the lower wall. The flow between the fins is now more complicated than in the ideal case (non-canted or centered). The shock waves which reflect off of the body are asymmetric with respect to the centerline of any of the channels. A set of five line traces of the tube wall pressure which have approximately the same angular position as those from the experiment of Fig. 5-12 is shown in Fig. 5-33. The characteristic "s" shape is evident, although the influence of the fins is much greater in the calculation than in the experiment. This may be due to the fin gap being much greater than the 1 mm used in the simulation.

The preceding calculations of canted projectiles with the fin effects included give an indication of the general character of the flow field that one might expect. As mentioned previously, if the simulations were to be repeated with a Navier-Stokes code which incorporates finite rate chemical kinetics, the flow may be quite different, especially at superdetonative velocities in a reacting gas (Soetrisno, Imlay, and Roberts, 1993).

5.4 Implications of Non-Ideal Projectile Flow Fields

5.4.1 Projectile Performance

The effects of projectile canting at sub- and transdetonative velocities are thought to be manifested in observed differences in acceleration performance between projectiles and the ability to successfully accomplish high velocity mixture transitions (staging). A canted projectile should have a higher drag and a lower diffuser efficiency than a centered projectile, although there has been no experimental attempt to establish a direct correlation between canting and acceleration performance. In theory, a 5-fin projectile should be more resistant to canting because if a pressure imbalance should occur in a channel, there is a fin directly opposite it on the other side of the projectile body which should oppose this force. A 4-fin projectile does not have this geometric advantage and the fins on the opposite side are subjected to side loads which may bend them.

A comparison of four-fin and five-fin projectiles can be made by examining their individual performance over the entire length of the 16 m stage during experiments performed with the HITS in place. This comparison was accomplished by plotting the projectile velocity as a function of distance along the tube for experiments which had a 28 atm fill pressure for the entire 16 m stage. From the theory of the thermally choked propulsion mode, the projectile should not achieve a velocity greater than that of the C-J detonation speed of the combustible mixture and should asymptotically approach this speed (Bruckner, Knowlen, and Hertzberg, 1991). A projectile which transitions from subdetonative to superdetonative speeds can therefore be assumed to be operating in a mode other than the thermally choked mode of propulsion. This discrepancy between theory and experiment can be explained by supersonic heat addition occurring on the projectile body, followed by mixed subsonic/supersonic heat addition behind the projectile which does not lead to thermal choking. All projectiles in the experiments of this study achieved a speed greater than 112% of the C-J detonation speed of the gas mixture.

A plot of projectile velocity versus distance along the ram accelerator tube for various experiments is shown in Fig. 5-34. Included are two experiments which used 5-fin projectiles as well as three experiments which used 4-fin projectiles. All of the experiments were carried out with a fill pressure of 28 atm. The four-fin projectile masses were 74 gm while the five-fin projectiles had masses of 84 gm. *With the same fill pressure, the four-fin projectiles should have a higher acceleration than the five-fin projectiles due to their lower mass.* Figure 5-34 shows that below approximately 1650 m/s (94% of the C-J detonation speed) the projectiles have similar velocity profiles. Since the 5-fin projectiles have approximately 12% more mass than the 4-fin projectiles, but have identical velocities, the 5-fin projectiles must be experiencing higher thrust levels than the 4-fin projectiles. The cause of this increased thrust may be related to the ability of the projectiles to resist canting (lower drag and/or better efficiency) or the 5-fin projectiles may have a smaller effective throat than the 4-fin projectiles. The former implying that the increased drag associated with the additional fin is more than compensated for by the increased diffuser efficiency over a canted projectile. The latter indicating that the projectile throat is in fact not located at the nose cone/body joint as thought, but effectively farther towards the rear of the projectile and the area of this effective throat it is affected by the number of fins.

Above 1650 m/s the 5-fin projectiles achieve higher velocities at a given distance in the stage. The cause of the increased thrust of the five-fin projectiles in the trans- and superdetonative regimes is not known, but also may be related to the presence of the extra fin. The fins of the projectile may act as flame holders which enable combustion to occur on the projectile body at transdetonative and superdetonative speeds. As shown by experiments and computational simulations, there is a region on the leading surface of the fins, near the tube wall, which experiences high pressure and temperature as a result of the flow nearly stagnating relative to the projectile. In this region the gas may react and maintain the combustion on the projectile body. The extra fin may add to the total amount of combustion on the body of the 5-fin projectile and hence exhibit increased thrust relative to 4-fin projectiles. This is in addition to the 5-fin projectiles theoretical ability to stay centered in the tube.

It also has been found that the incidence of transition failures increases with projectile velocity and may thus be related to the increase in projectile fin wear which inevitably occurs as the projectile travels through the tube. There also is anecdotal evidence that 5-fin projectiles are more robust at high speed transitions in multi-stage experiments.

5.4.2 Projectile Unstarts

At superdetonative velocities the effects of projectile canting are thought to contribute to the unstart phenomenon in which projectiles fail to continue to accelerate to velocities appreciably higher than 120% of the C-J detonation speed in a single stage of the present mixture (Hinkey, Burnham, and Bruckner, 1993). Axisymmetric Navier-Stokes, finite rate kinetics simulations of other researchers fail to unstart at significantly higher percentages of the C-J detonation speed (Soetrisno, Imlay, and Roberts, 1992), suggesting that canting may play a role. In fact, two-dimensional Navier-Stokes finite rate kinetics simulations of a planar projectile will produce an unstart *only* if the projectile is canted (Soetrisno, Imlay, and Roberts, 1993). Fin effects on a canted projectile for viscous reacting flow are not fully known at this time, with only preliminary numerical investigations having been performed (Soetrisno, Imlay, and Roberts, 1993). For multi-stage experiments, projectiles fail to reach speeds greater than the detonation velocity in the stages subsequent to the first.

The unstart phenomenon in a single stage mixture of $2.7\text{CH}_4 + 2\text{O}_2 + 5.8\text{N}_2$ was investigated by placing a pair of inserts near where a projectile would reach approximately 120% of the C-J detonation speed of the mixture. A series of experiments were required since the exact location where an unstart would take place could not be accurately known a priori and had to be iterated upon by adjusting the initial tube fill pressure.

The 16 line plots of the tube wall pressure measured using a pair of inserts from this experiment are shown in Fig. 5-35. The projectile was travelling at 2060 m/s (Mach 5.7) or 118% of the C-J detonation speed of the mixture with an initial tube fill pressure of 35 atm. Most noticeable is the very strong shock located in the vicinity of the projectile nose cone and an additional shock located about one-quarter of a projectile length behind the projectile. Also note that the pressure rise from the initial conical shock generated by the nose cone is still recognizable. The strong shock is in the process of disgorging from the diffuser of the projectile and is therefore traveling at a speed greater than the projectile. The pressure decreases immediately behind the shock due to the increase in the velocity of the subsonic flow to a choke point somewhere on the projectile body. It is this choking of the flow somewhere on the projectile body that disgorges the shock ahead of the projectile. The limited data from experiments near an unstart which have exhibited signs of wave steepening due to shock-induced combustion have shown signs of being only mildly canted. This may be due to the combustion augmented shock waves not corresponding the non-reacting nose cone angle of attack or the projectile is unable to cant any further.

Figure 5-36 is a line plot of the tube wall pressure from one of the transducers in Fig. 5-35 compared to the magnetic sensor and pressure data from an instrument station 22 cm directly upstream (opposite the direction of projectile motion). Figure 5-36 gives a sense of the development of the large amplitude shock wave since at the upstream station the wave is of smaller amplitude, the initial shock generated by the nose cone is more distinct, and the overall pressure distribution is closer to what would be expected at lower velocities, like the data shown in Fig 5-5. The magnetic sensor data definitively locates the position of the nose cone/body joint of the projectile relative to the pressure data and thus the position of the projectile relative to the pressure data obtained with the inserts is also known. Figure 5-36 and Fig. 5-5 qualitatively show the progression of the unstart process. The information from these experiments, combined with the previously mentioned two-

dimensional canted planar projectile numerical simulations strongly indicate that unstarts in the superdetonative regime are caused by a *combination* of projectile canting and shock induced combustion.

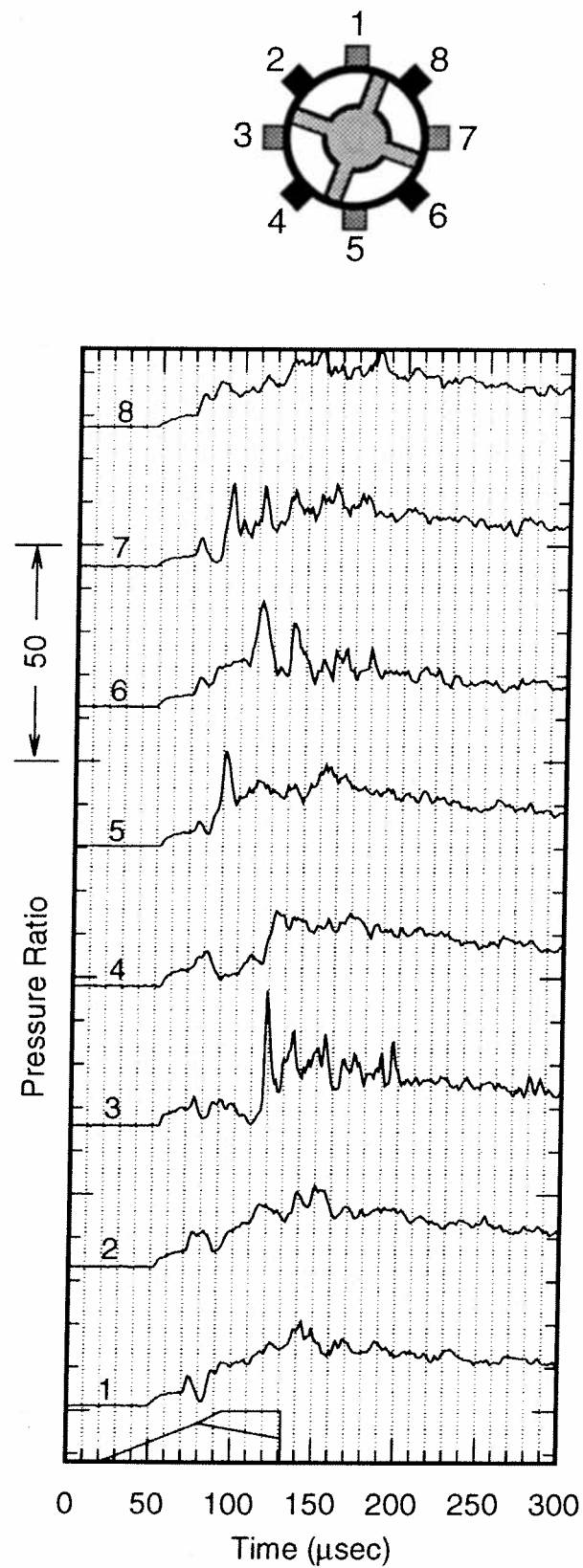


Figure 5-1: Tube wall pressure traces from the first set of pressure transducers in the HITS. Subdetonative regime, 1400 m/s (Mach 3.9) or 80% of the C-J detonation speed.

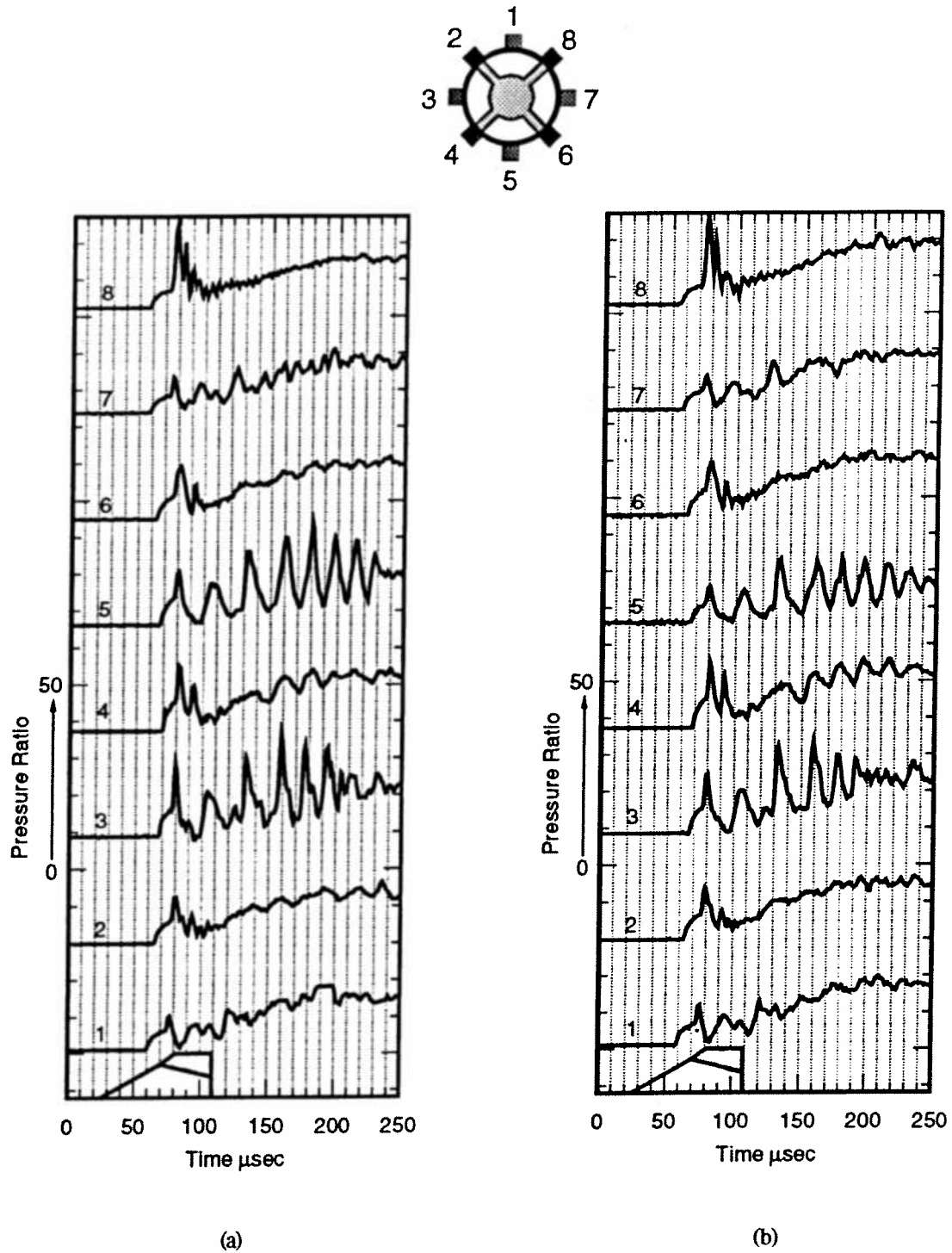


Figure 5-2: Tube wall pressure traces from the first set (a) and the second set (b) of pressure transducers in the HITS. Transdetonative regime, 1850 m/s (Mach 5.1) or 106% of the C-J detonation speed.

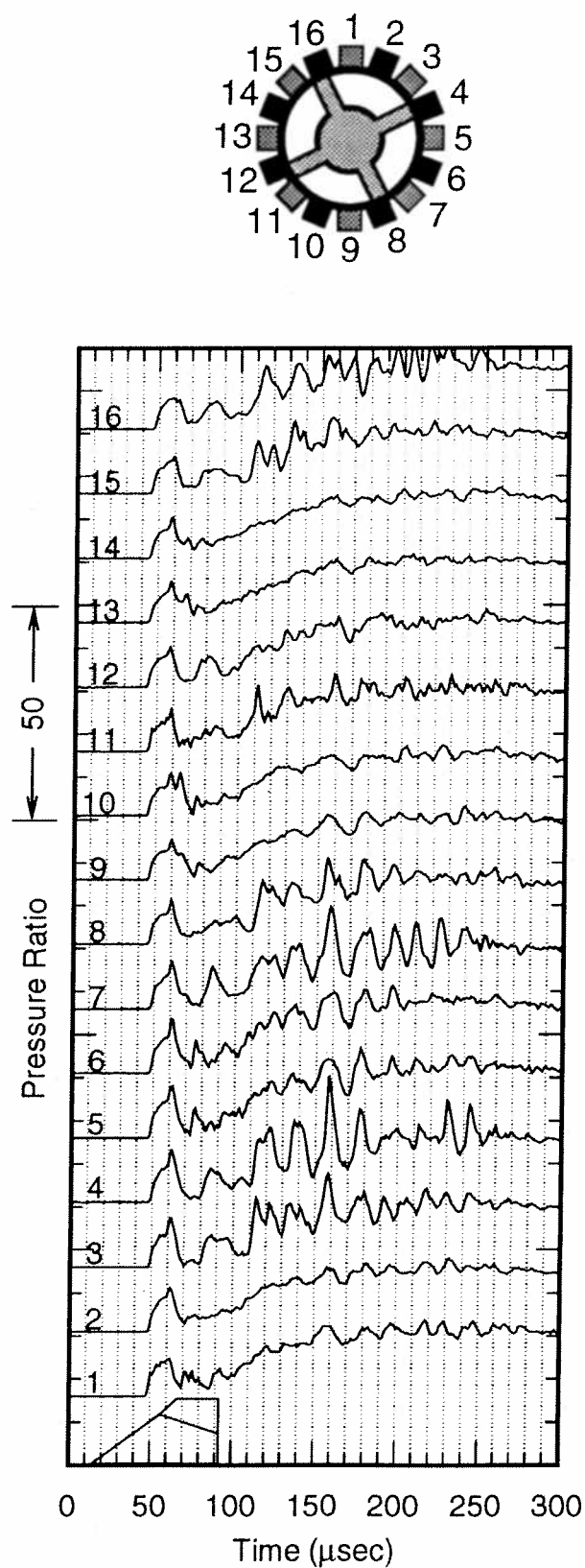


Figure 5-3: Tube wall pressure traces from the pressure transducers in the inserts. Superdetonative regime, 1960 m/s (Mach 5.4) or 112% of the C-J detonation speed.

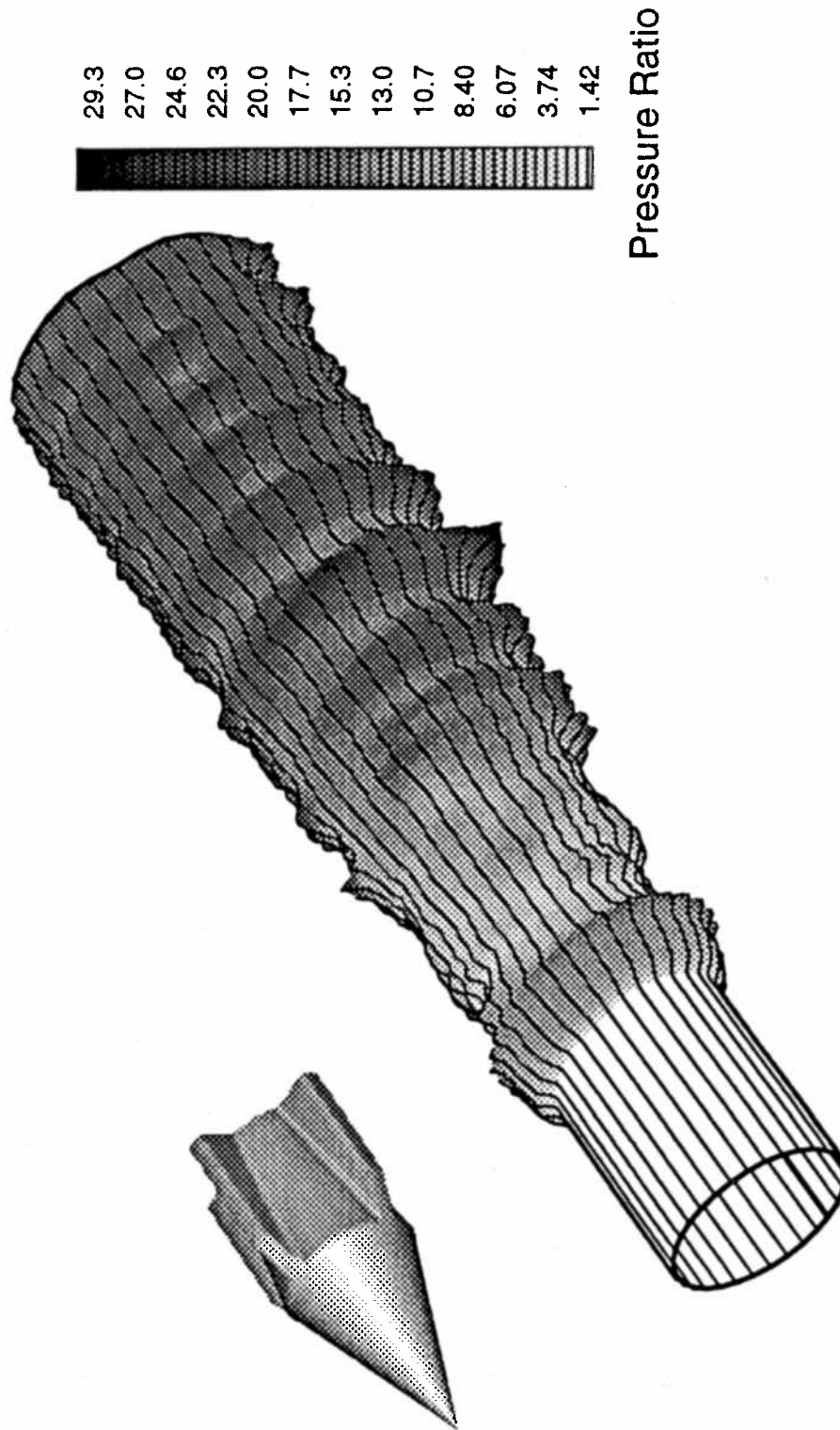


Figure 5-4: Reconstructed tube wall pressure distribution from the superdetonative regime, 1960 m/s (Mach 5.4) or 112% of the C-J detonation speed. Pressure data are proportional to surface shading and radial distance from the surface of a cylinder representing the tube wall. Pressure normalized by initial tube fill pressure.

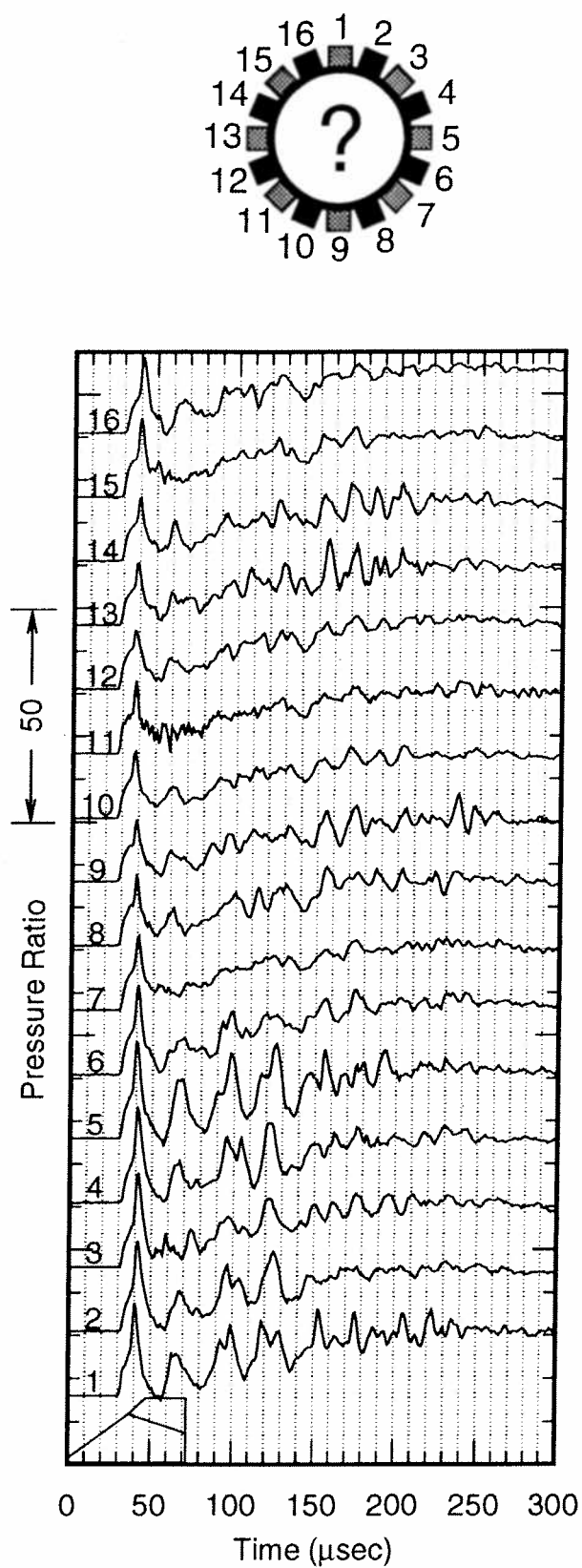


Figure 5-5: Tube wall pressure traces from the transducers in the inserts. Superdetonative regime, 2020 m/s (Mach 5.6) or 115% of the C-J detonation speed.

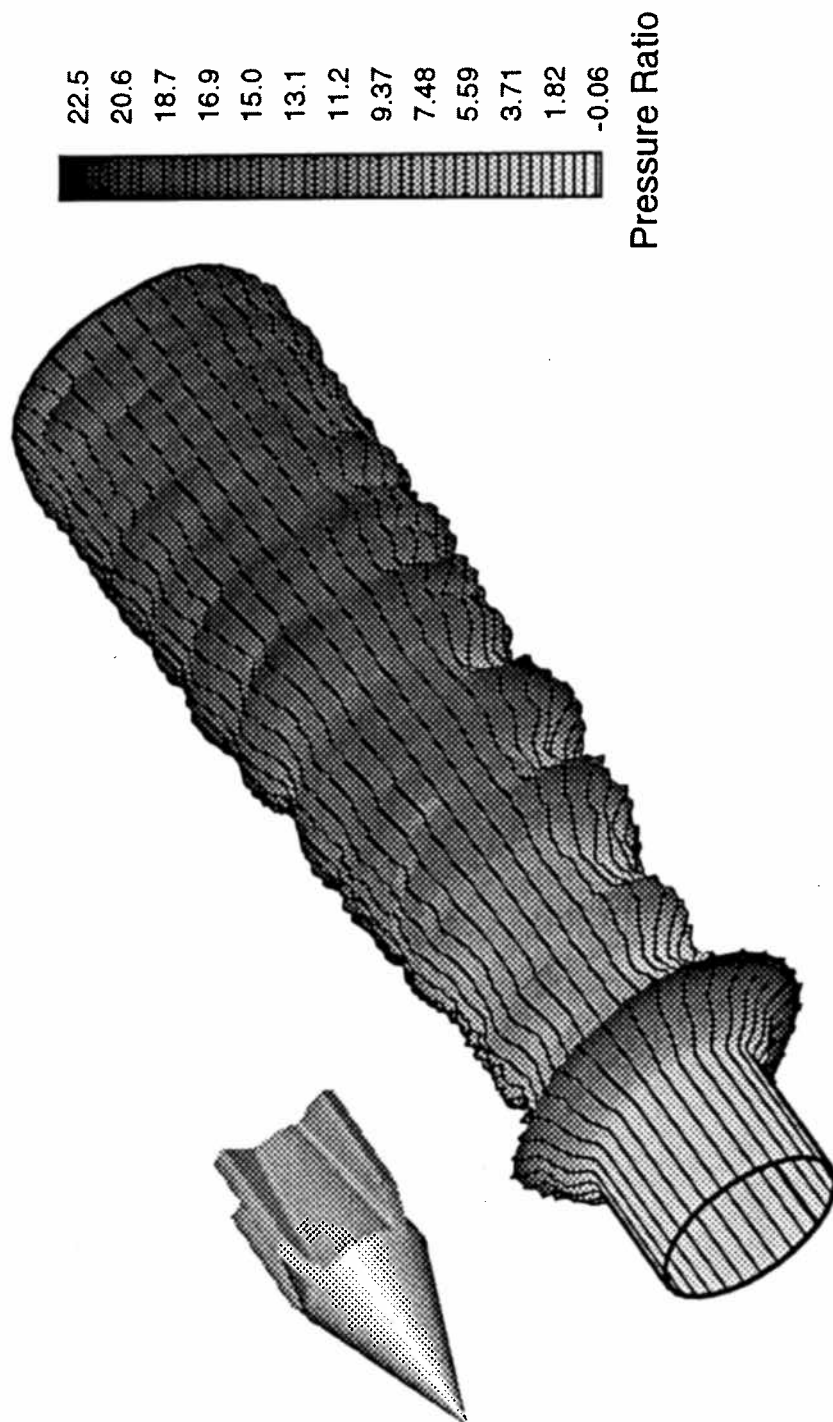


Figure 5-6: Reconstructed tube wall pressure distribution from the superdetonative regime, 2020 m/s (Mach 5.6) or 115% of the C-J detonation speed. Pressure data are proportional to surface shading and radial distance from the surface of a cylinder representing the tube wall. Pressure normalized by initial tube fill pressure.

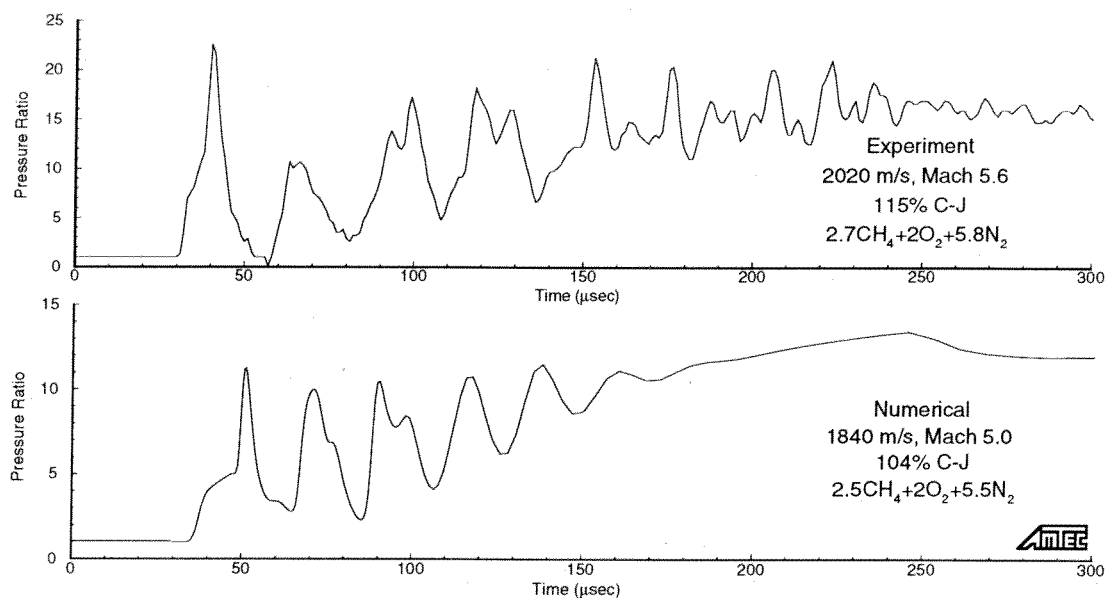


Figure 5-7: Qualitative comparison of a tube wall pressure trace from Fig. 5-5 with the numerical simulation of Soetrisno et. al (1992). Experimental conditions are 2020 m/s (Mach 5.6) or 115% of the C-J detonation speed with a mixture of $2.7\text{CH}_4 + 2\text{O}_2 + 5.8\text{N}_2$ at 32 atm. Numerical conditions are 1840 m/s (Mach 5.0) or 104% of the C-J detonation speed with a mixture of $2.5\text{CH}_4 + 2\text{O}_2 + 5.5\text{N}_2$ at 31 atm.

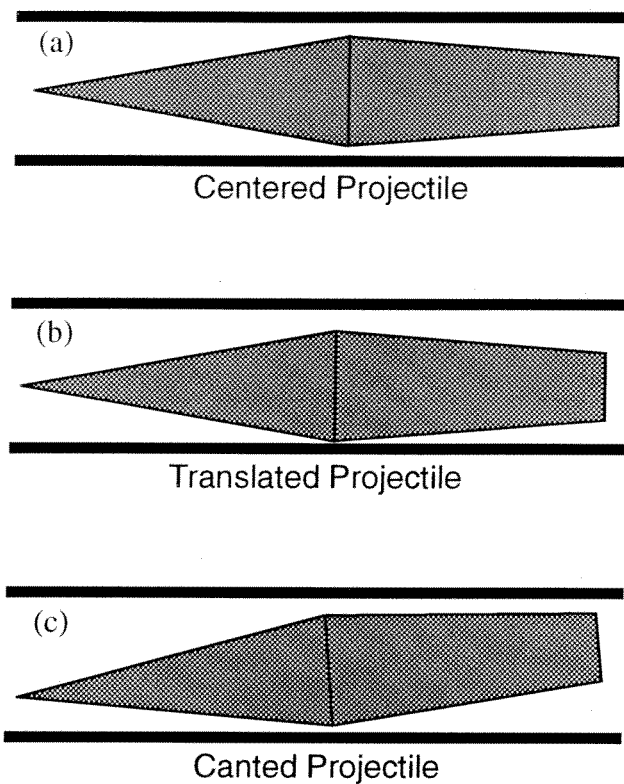


Figure 5-8: Three possible positions of a projectile relative to the tube wall.

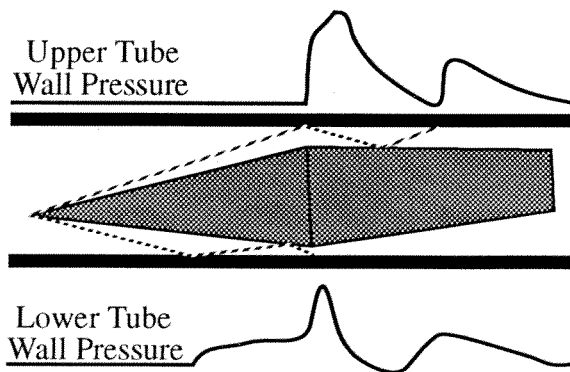


Figure 5-9: Illustration of the difference in arrival position of the initial shock and the magnitude of the reflection at the opposing sides of a tube for a canted projectile.

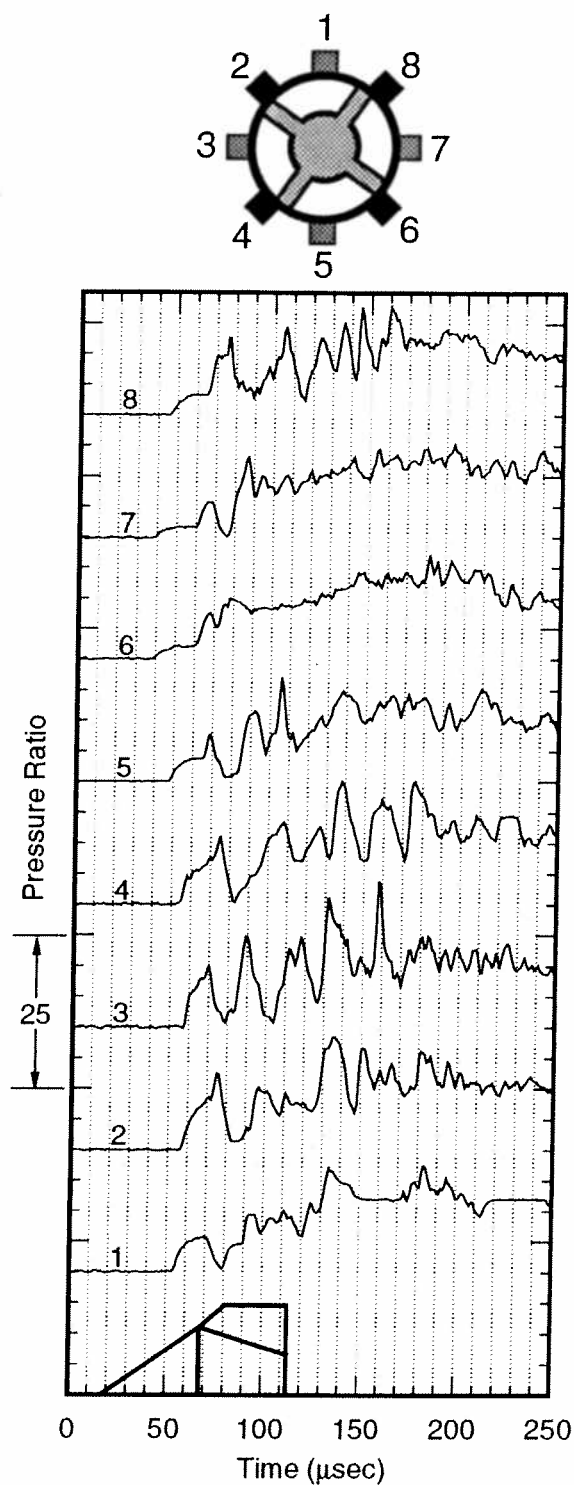


Figure 5-10: Tube wall pressure traces using the HITS illustrating a canted projectile. Subdetonative regime, 1560 m/s (Mach 4.3) or 89% of the C-J detonation speed. Reacting mixture of $2.7\text{CH}_4 + 2\text{O}_2 + 5.8\text{N}_2$.

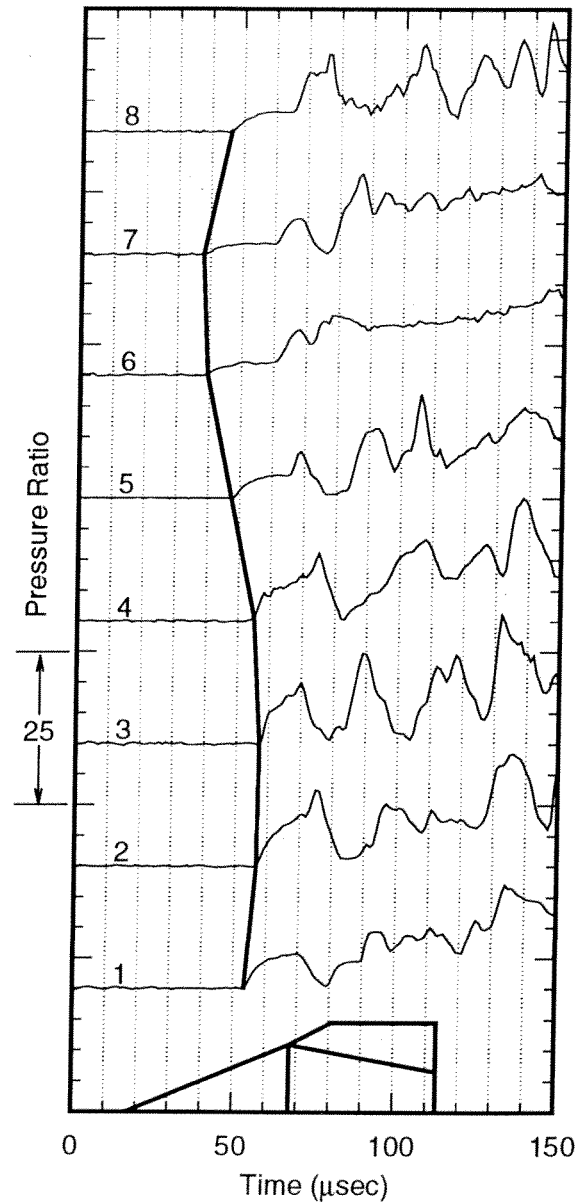


Figure 5-11: Tube wall pressure traces from Fig. 5-10 with the time scale expanded to accentuate the difference in arrival time of the initial shock wave. The arrival points of the initial shock wave have been connected by lines between traces for better visualization.

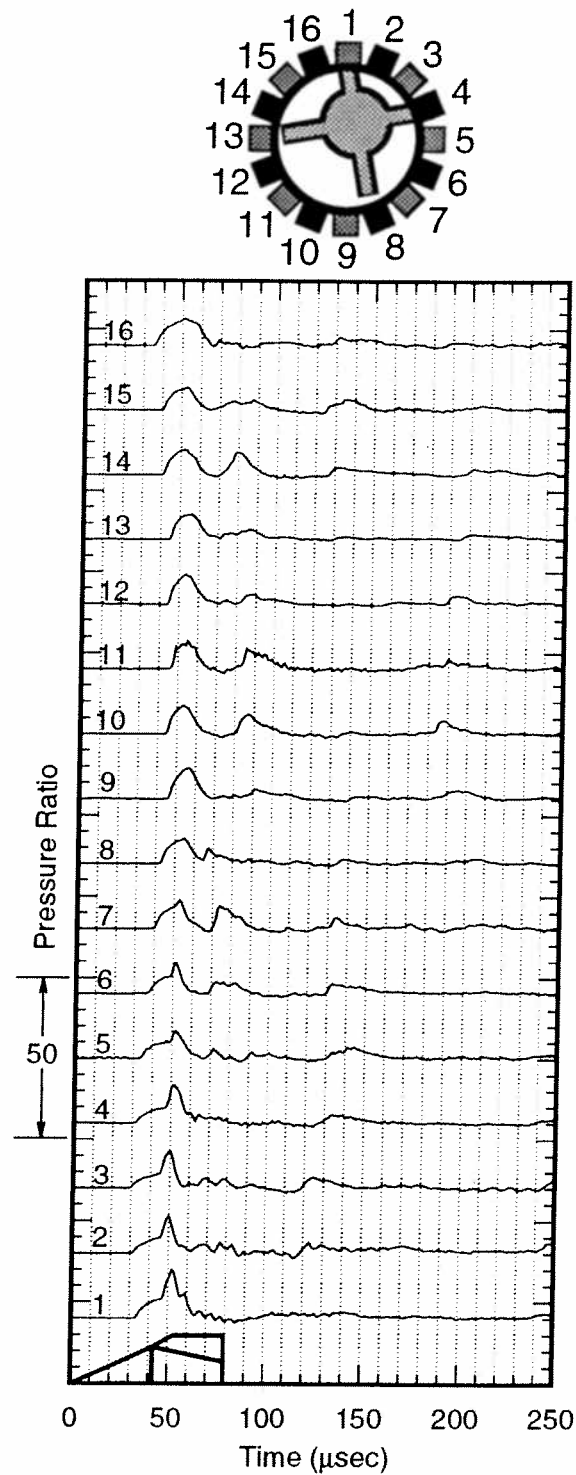


Figure 5-12: Tube wall pressure traces illustrating a canted projectile, superdetonative regime, 1920 m/s (Mach 5.3) or 110% of the C-J detonation speed of the equivalent reacting gas. A non-reacting gas mixture of $2.7\text{CH}_4 + 7.8\text{N}_2$.

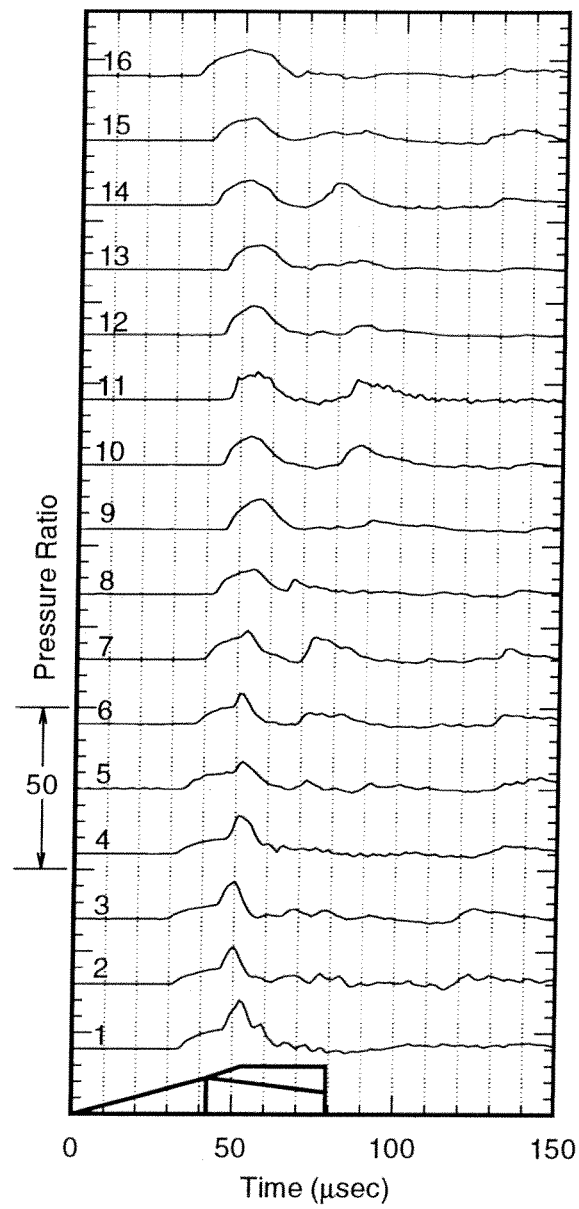


Figure 5-13: Tube wall pressure traces from Fig. 5-12 with the time scale expanded to accentuate the difference in arrival time of the initial shock wave and the variation in the magnitude of the reflected shock.

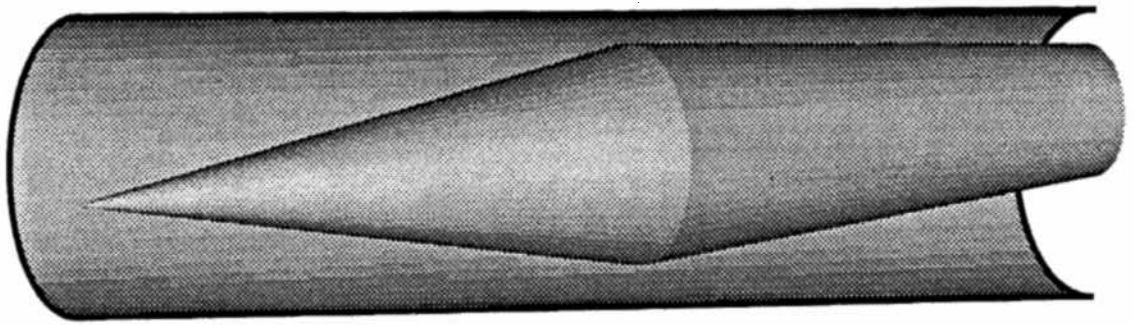


Figure 5-16: General geometry of a canted axisymmetric three-dimensional projectile and the tube wall used in the numerical simulations. One-half of the full tube is numerically simulated by assuming a plane of symmetry. The computational grid is $149 \times 49 \times 49$ cells in the axial, radial, and circumferential directions respectively.

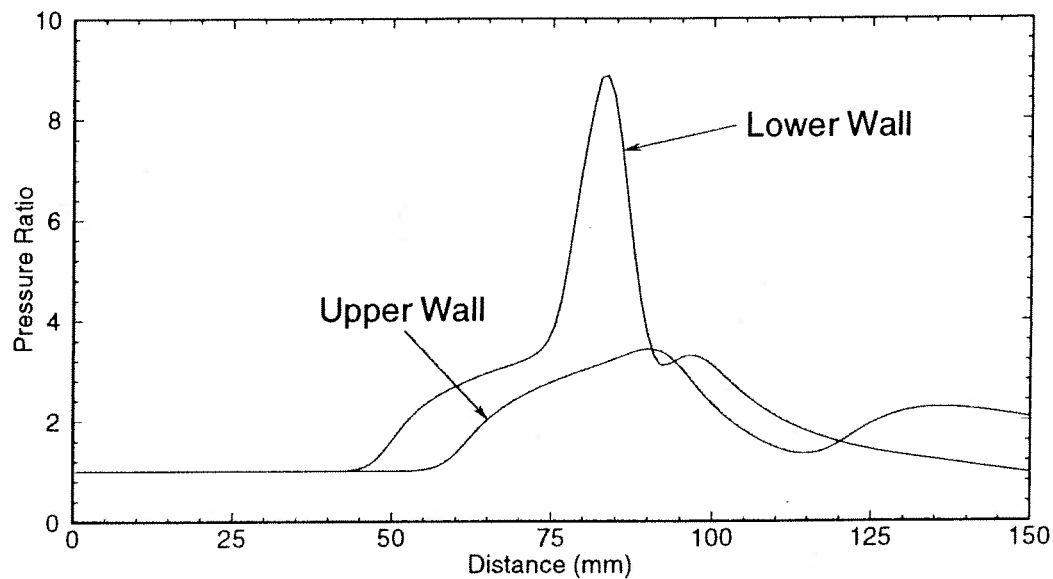


Figure 5-17: Calculated upper and lower tube wall pressure for an axisymmetric projectile which is translated by 2 mm (0° angle of attack) toward the lower wall. Mach 4.0 (1450 m/s) or 83% of the C-J detonation speed of the equivalent reacting gas mixture. The position where the initial shock wave reflects from the tube wall is different while the magnitude of the reflections are equal.

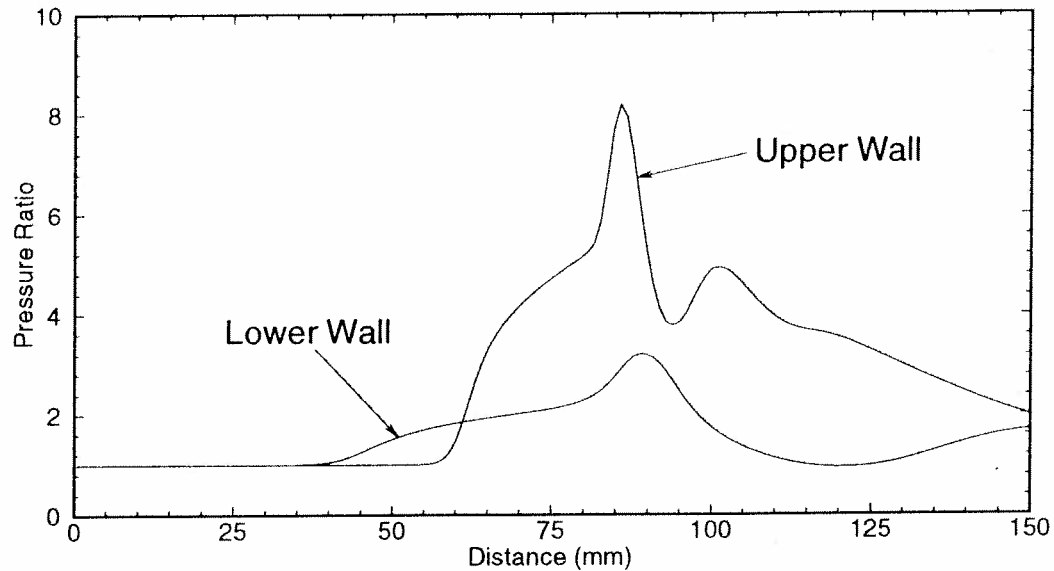


Figure 5-18: Calculated upper and lower tube wall pressure for a canted axisymmetric projectile. The nose tip is translated by 5 mm toward the lower wall with an angle of attack of 4° . Mach 4.0 (1450 m/s) or 83% of the C-J detonation speed of the equivalent reacting gas mixture. The positions where the initial shock wave reflects from the tube wall are different and the magnitude of the reflections are not equal.

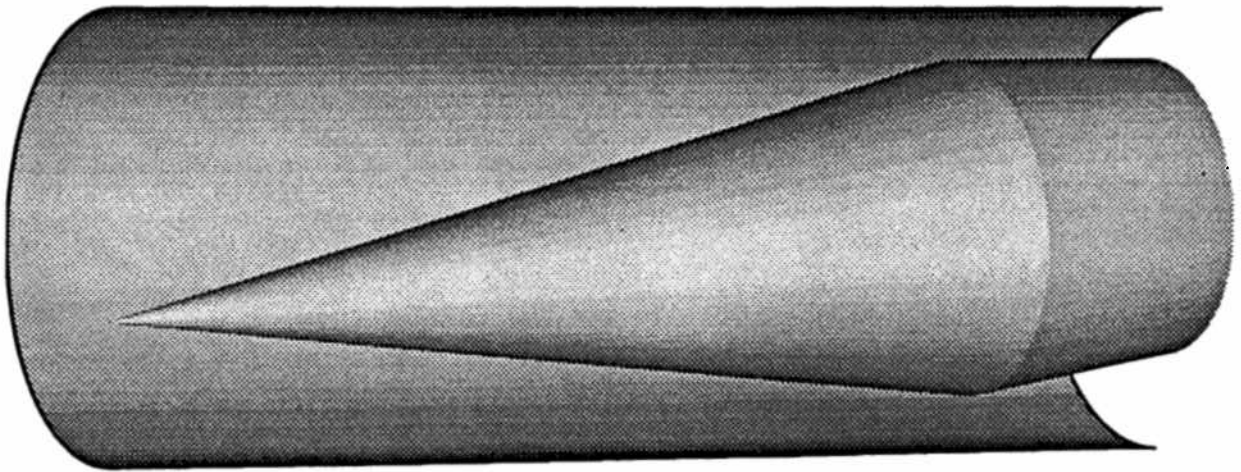


Figure 5-19: General geometry of a canted axisymmetric three-dimensional projectile and the tube wall used in the numerical simulations. One-half of the full tube is numerically simulated by assuming a plane of symmetry while only the first 2/3 of the projectile length (102 mm) is simulated. The computational grid is $149 \times 49 \times 49$ in the axial, radial, and circumferential directions respectively.

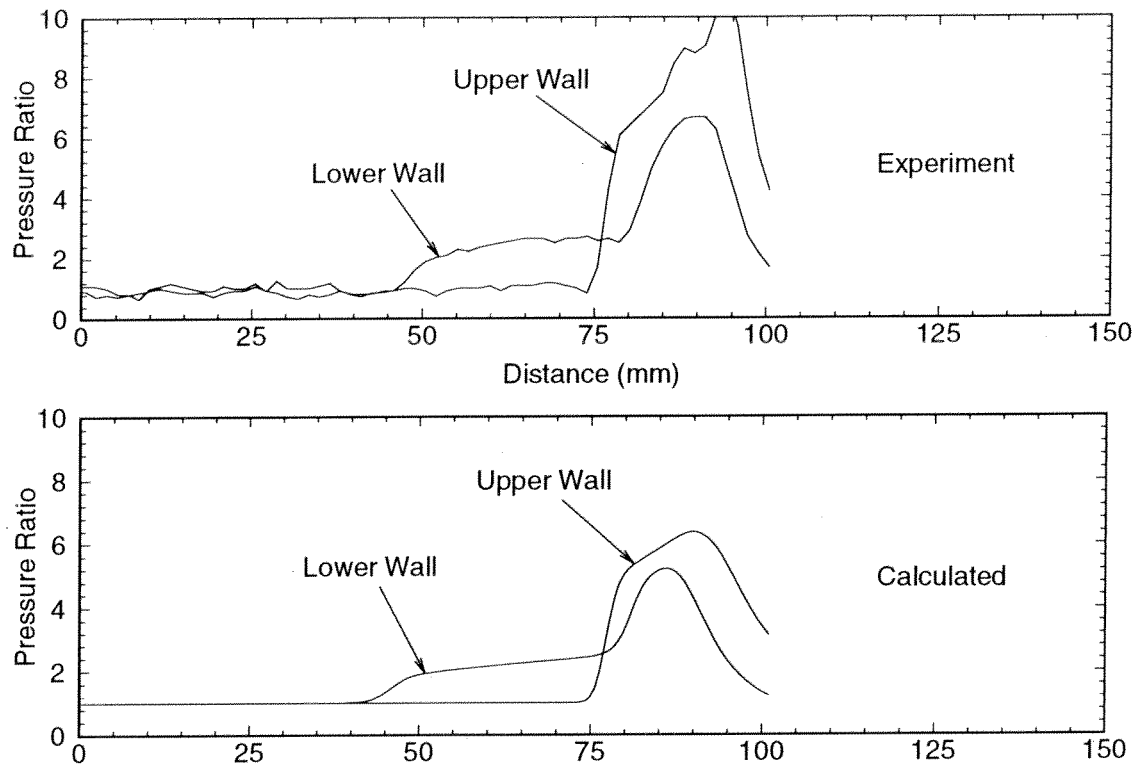


Figure 5-20: Comparison of calculated (bottom) to experimental (top) tube wall pressure traces for a canted projectile with an estimated angle of attack of 4.5° and a nose tip translation of 7.5 mm. Subdetonative regime, 1560 m/s (Mach 4.3) or 89% of the C-J detonation speed.

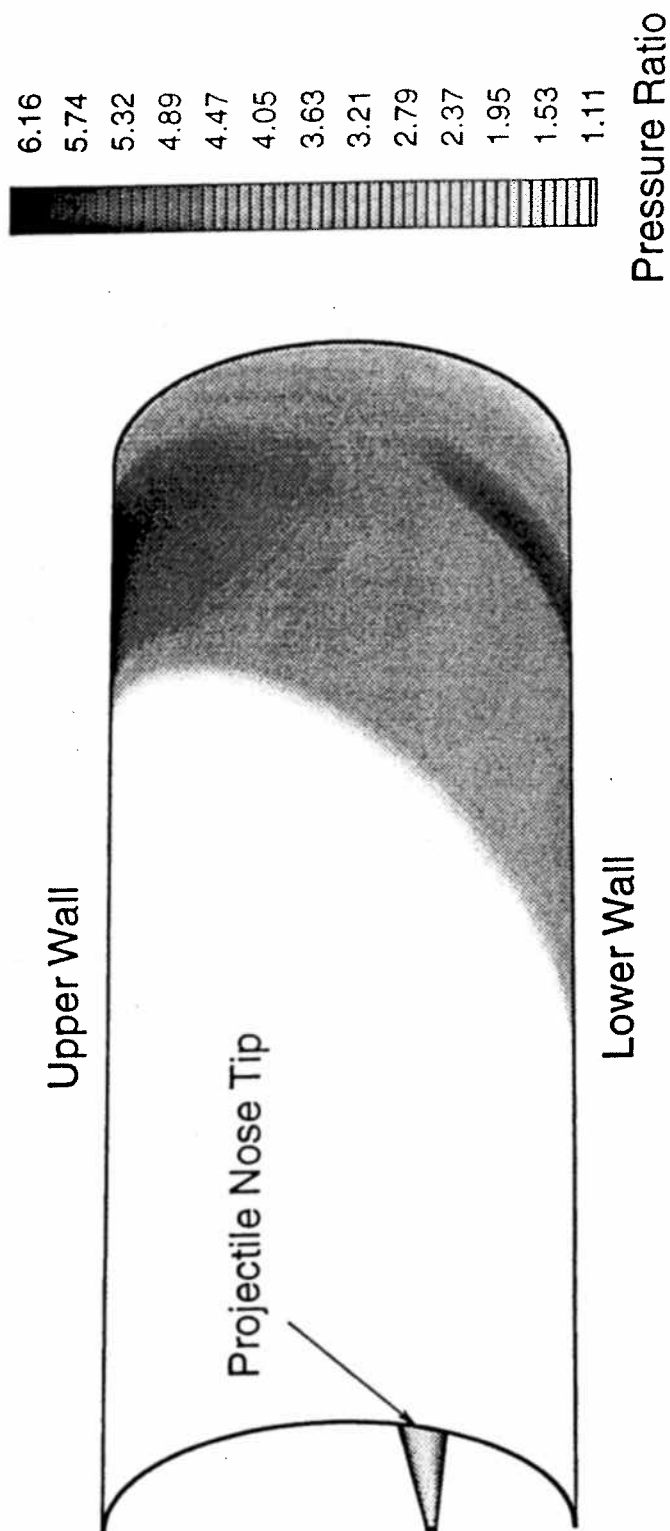


Figure 5-21: Three-dimensional surface plot of the calculated tube wall pressure distribution resulting from a canted axisymmetric projectile with an angle of attack of 4.5° and a nose tip translation of 7.5 mm. Subdetonative regime, 1560 m/s (Mach 4.3) or 89% of the C-J detonation speed. Surface shading is proportional to pressure.

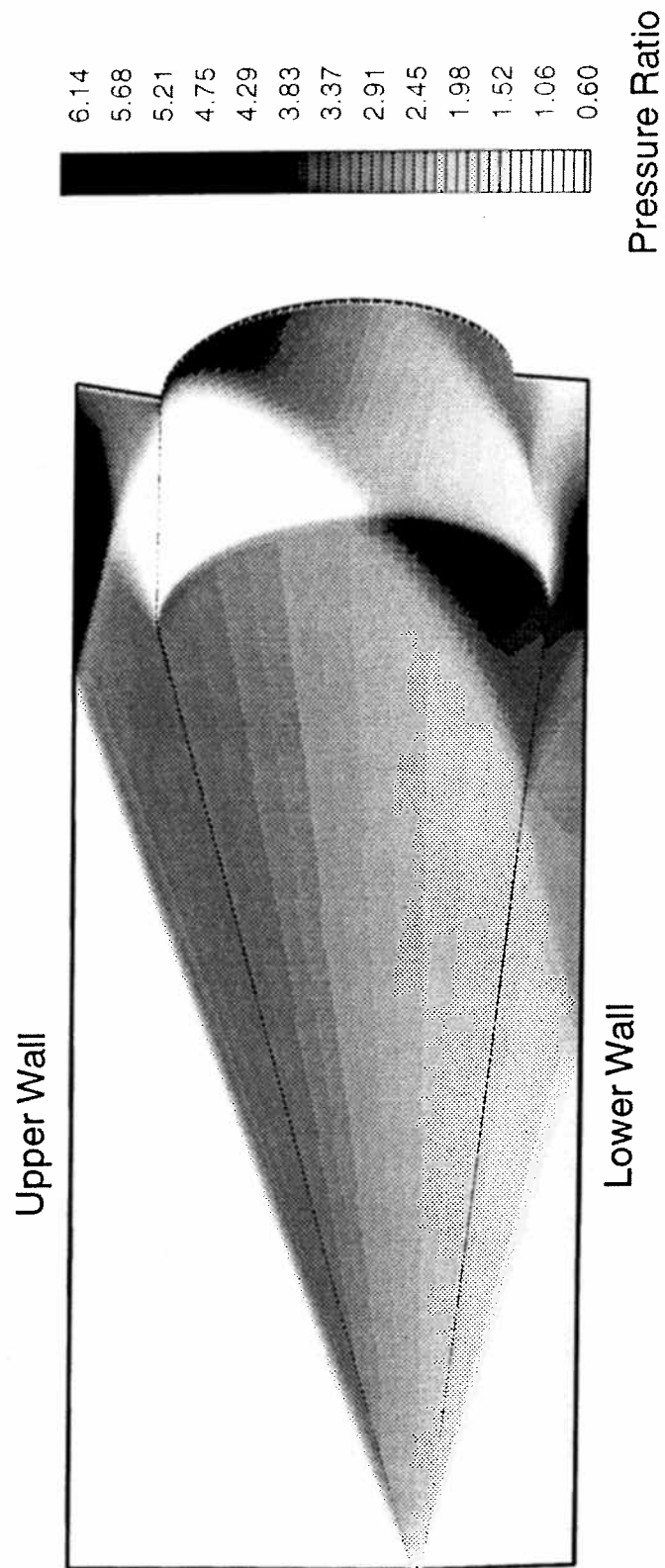


Figure 5-22: Three-dimensional surface plot of the calculated body surface pressure distribution of a canted axisymmetric projectile with an angle of attack of 4.5° and a nose tip translation of 7.5 mm. Pressure distribution of the upper and lower symmetry planes also shown. Subdetonative regime, 1560 m/s (Mach 4.3) or 89% of the C-J detonation speed. Surface shading is proportional to pressure.

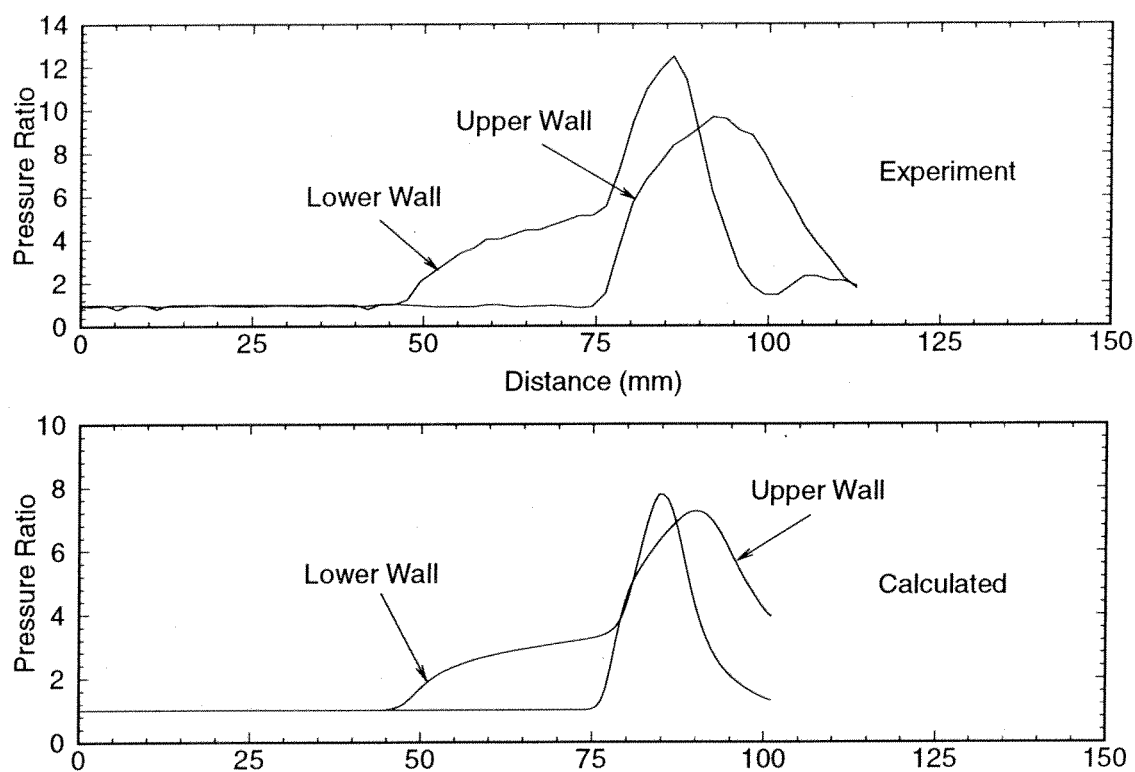


Figure 5-23: Comparison of calculated (bottom) and experimental (top) tube wall pressure traces for a canted projectile with estimated angle of attack of 3° and a nose tip translation of 6.5 mm. Superdetonative regime, 1920 m/s (Mach 5.3) or 110% of the C-J detonation speed. Non-reacting mixture of $2.7\text{CH}_4 + 7.8\text{N}_2$.

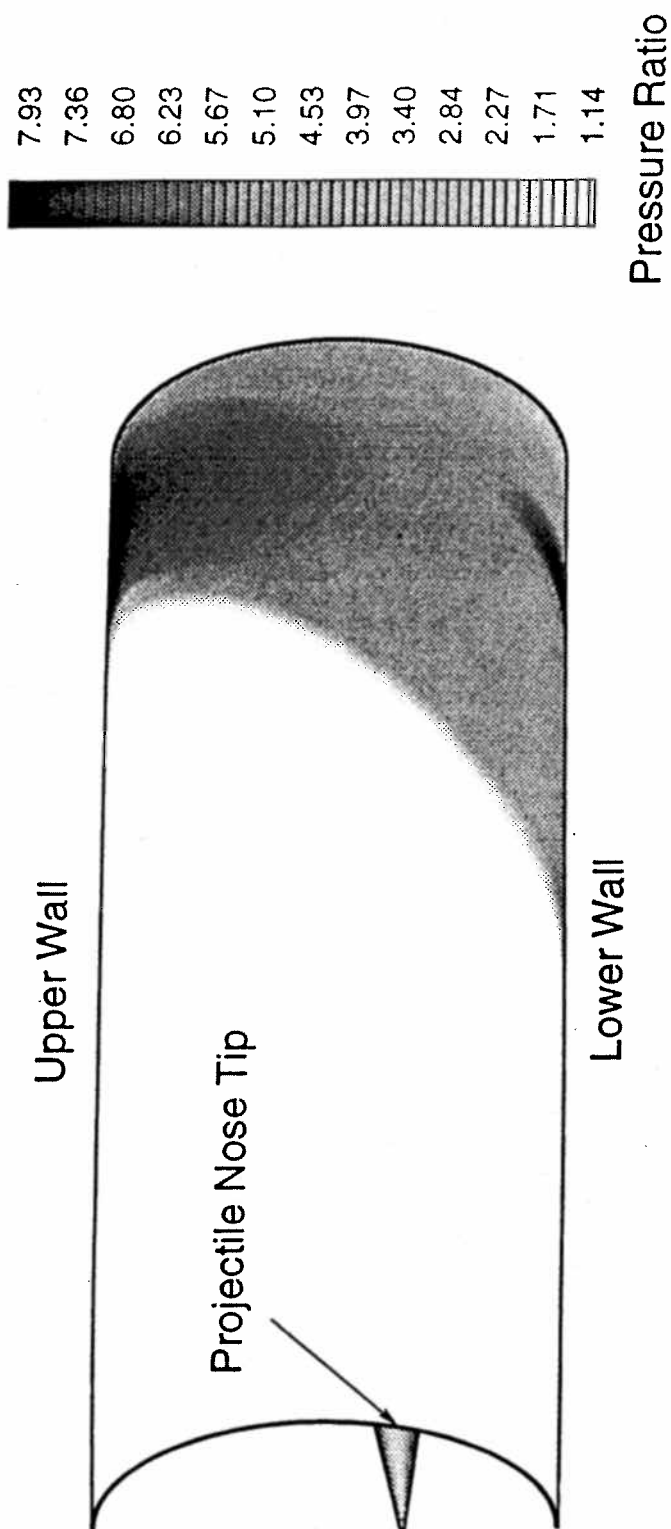


Figure 5-24: Three-dimensional surface plot of the calculated tube wall pressure distribution resulting from a canted axisymmetric projectile with an angle of attack of 3° and a nose tip translation of 6.5 mm. Superdetonative regime, 1920 m/s (Mach 5.3) or 110% of the C-J detonation speed. Surface shading is proportional to pressure.

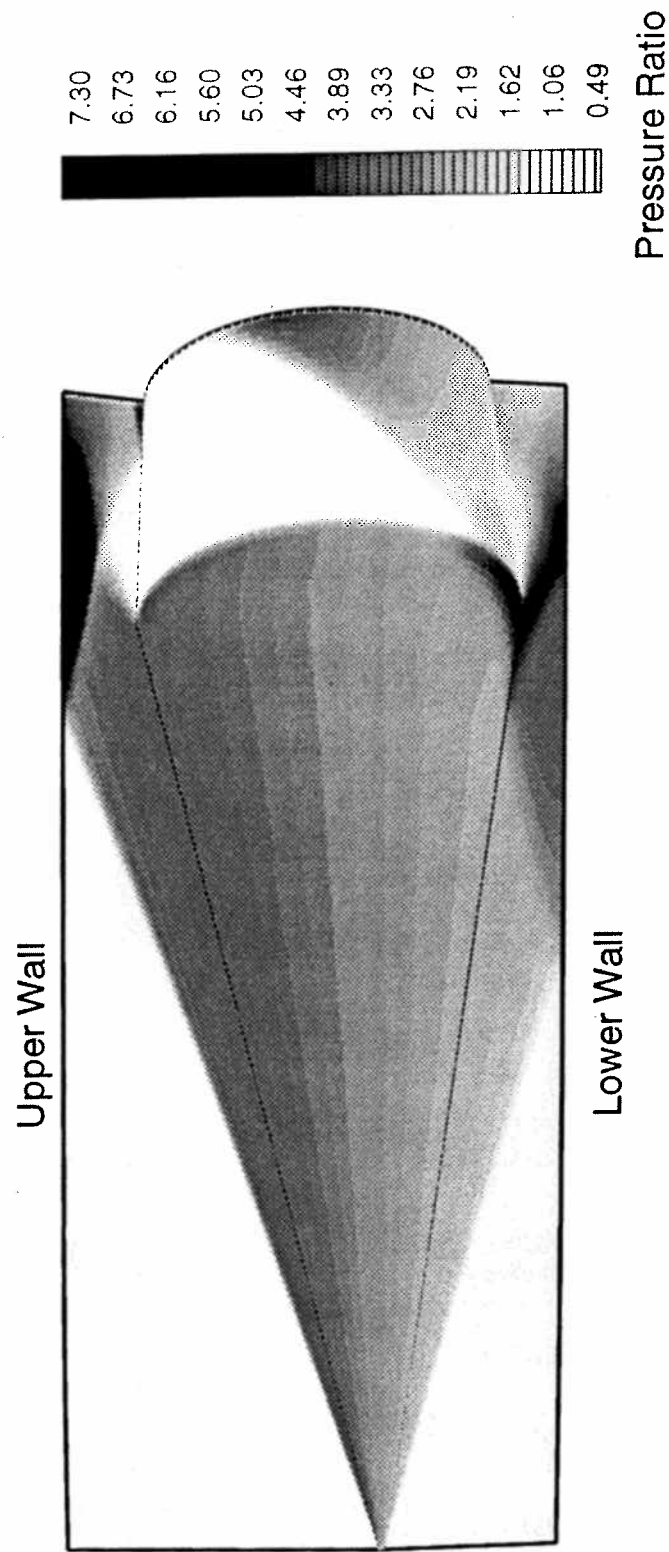


Figure 5-25: Three-dimensional surface plot of the calculated body surface pressure distribution of a canted axisymmetric projectile with an angle of attack of 3° and a nose tip translation of 6.5 mm. Pressure distribution of the upper and lower symmetry planes also shown. Superdetonative regime, 1920 m/s (Mach 5.3) or 110% of the C-J detonation speed. Surface shading is proportional to pressure.

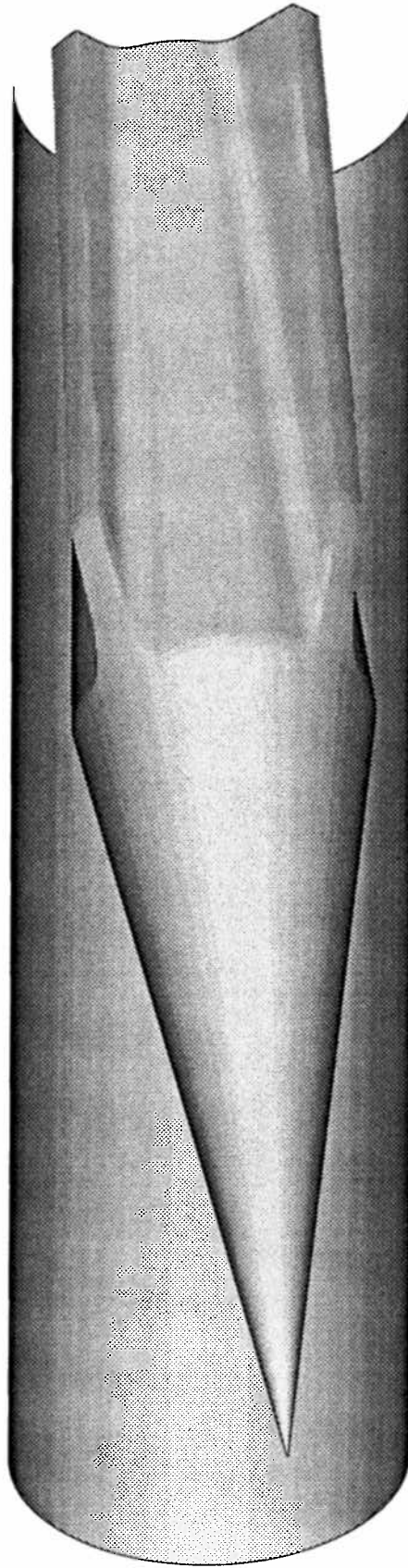


Figure 5-26: Projectile geometry used in the simulation of a canted projectile with fins which has an angle of attack of 4.5° and a nose tip translation of 7.5 mm. 149x119x29 cell grid in the axial, circumferential and radial directions respectively.

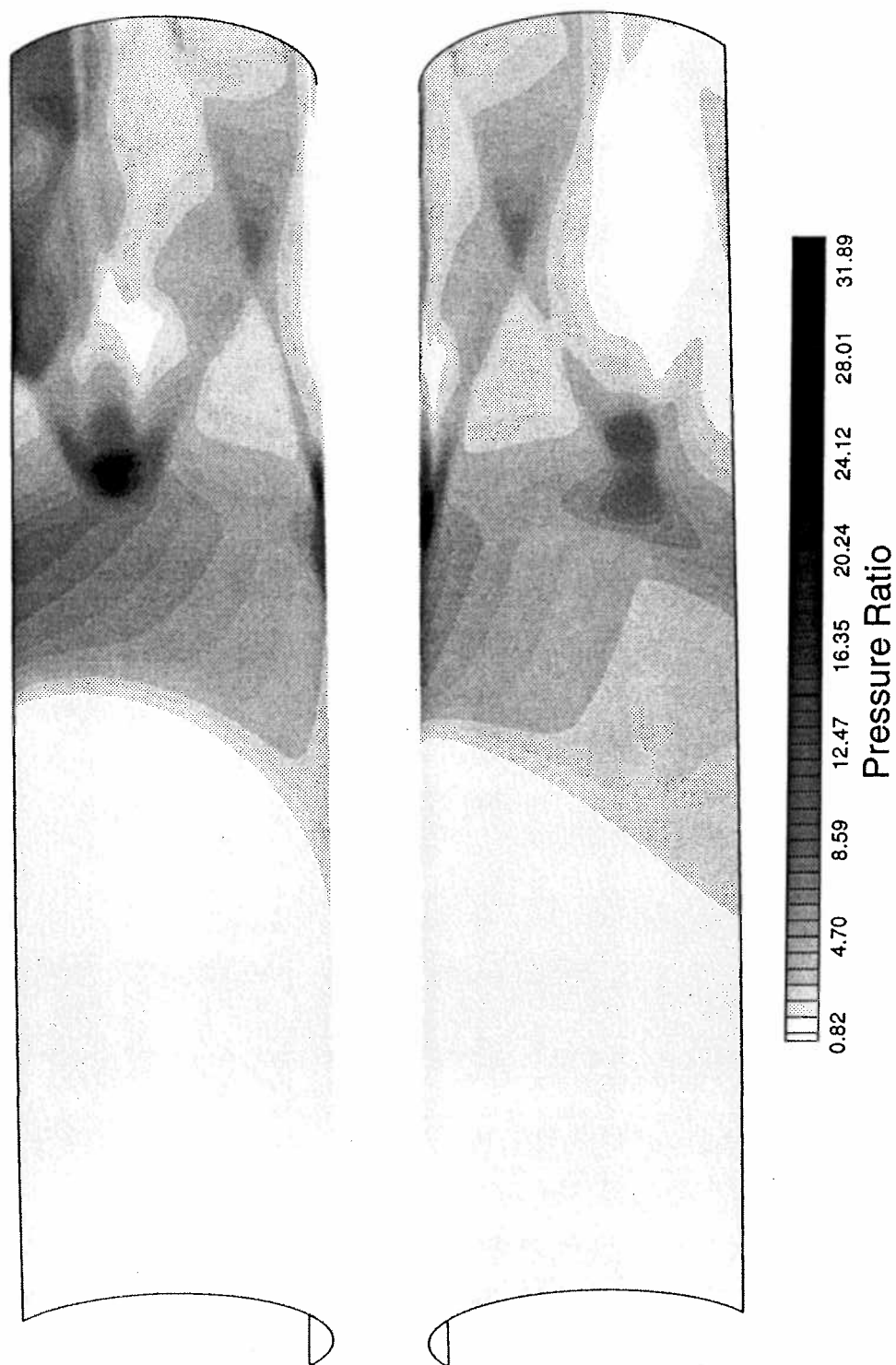


Figure 5-27: Three-dimensional surface plots of the calculated tube wall pressure distribution resulting from a canted projectile with fins which has an angle of attack of 4.5° and a nose tip translocation of 7.5 mm. Subdetonative regime, 1560 m/s (Mach 4.3) or 89% of the C-J detonation speed. Surface shading is proportional to pressure.

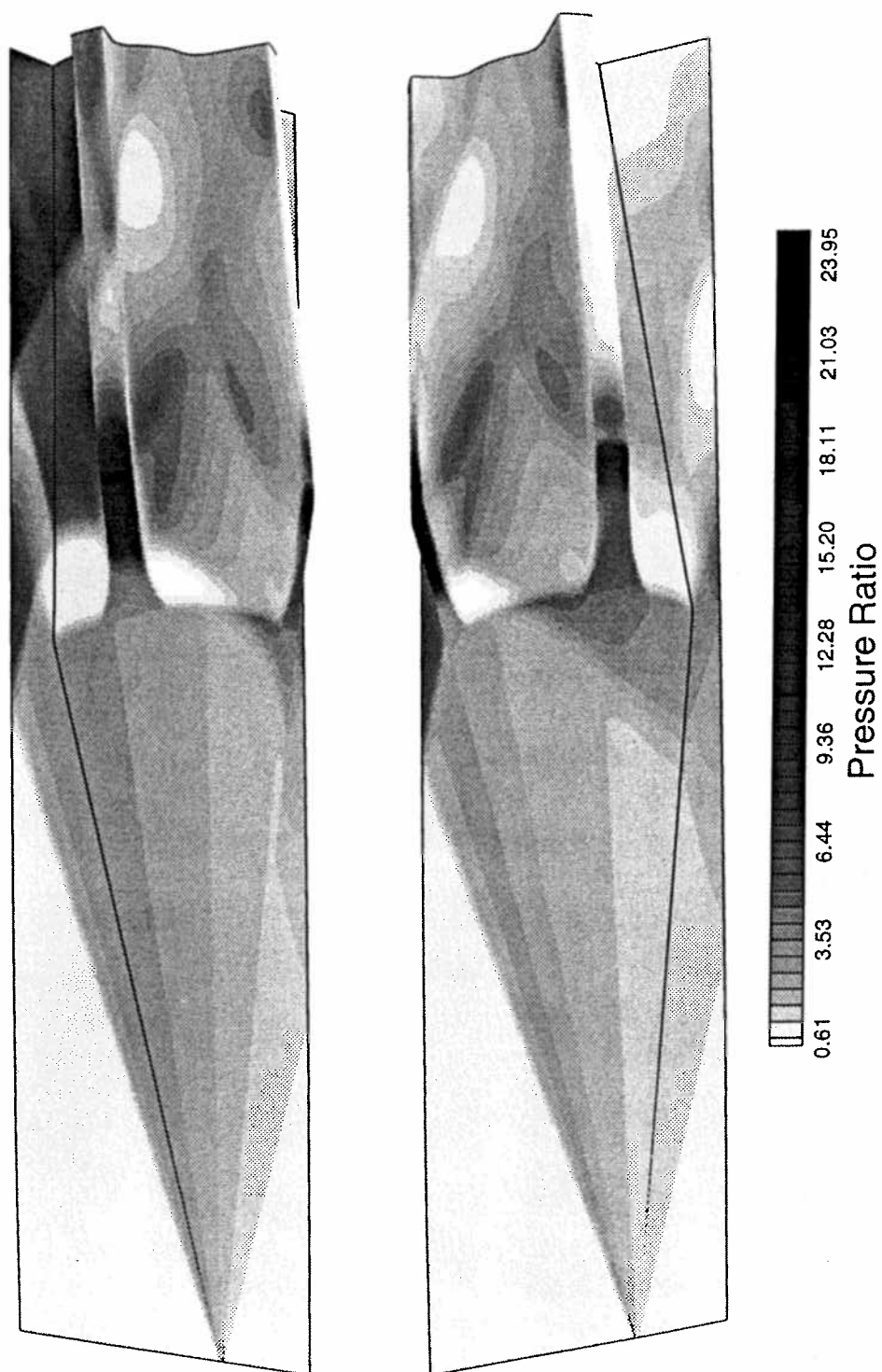


Figure 5-28: Three-dimensional surface plots of the calculated body surface pressure distribution of a canted projectile with fins which has an angle of attack of 4.5° and a nose tip translation of 7.5 mm. Pressure distribution of the upper and lower symmetry planes also shown. Subdetonative regime, 1560 m/s (Mach 4.3) or 89% of the C-J detonation speed. Surface shading is proportional to pressure.

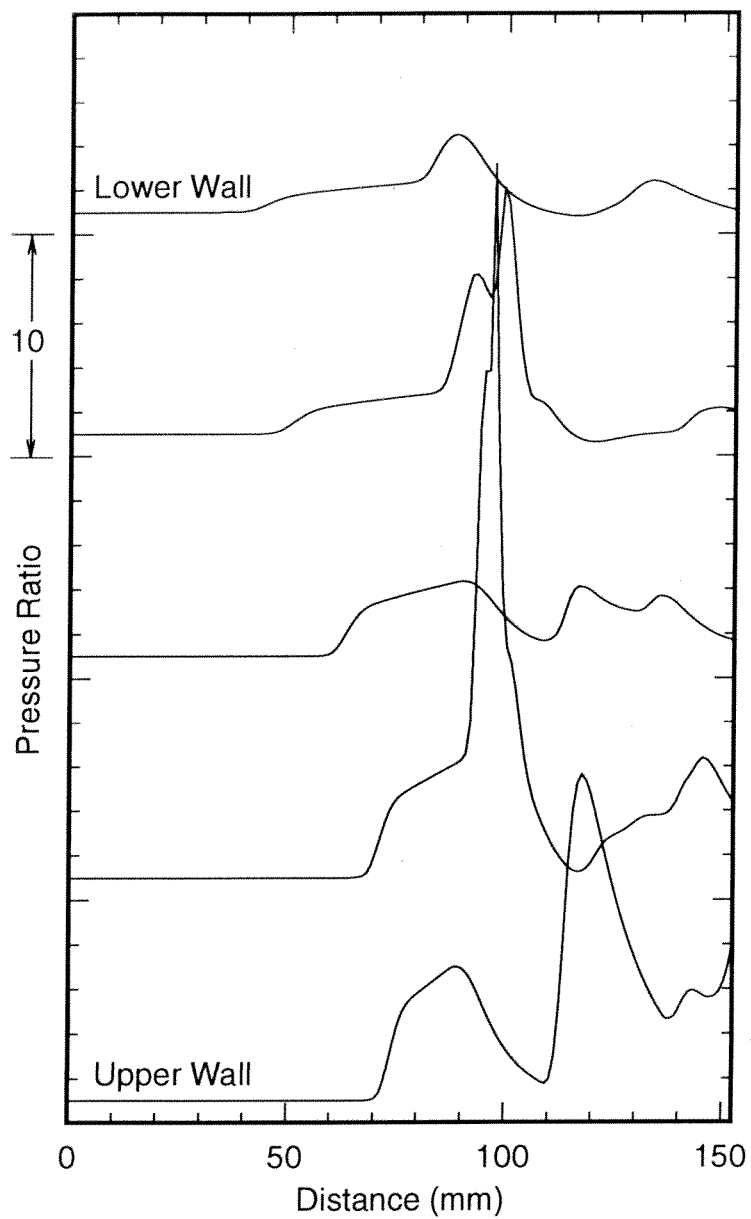


Figure 5-29: Line plots of the calculated tube wall pressure distribution of a canted projectile with fins which has an angle of attack of 4.5° and a nose tip translation of 7.5 mm. Subdetonative regime, 1560 m/s (Mach 4.3) or 89% of the C-J detonation speed. These 5 traces correspond to 45° increments in circumferential angle from the upper to lower wall.

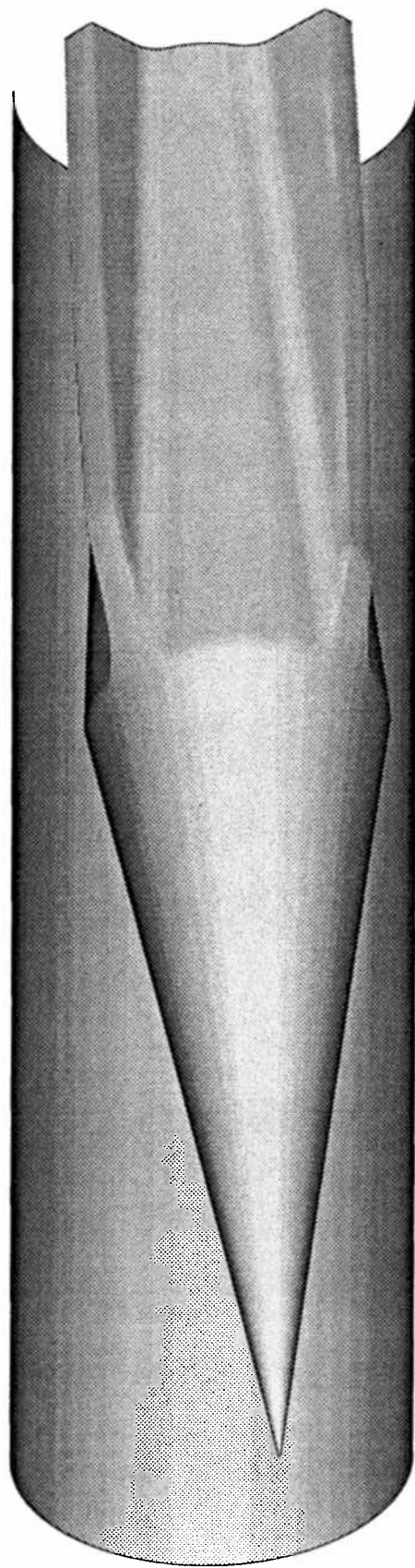


Figure 5-30: Projectile geometry used in the simulation of a canted projectile with fins which has an angle of attack of 3° and a nose tip translation of 6.5 mm. 149x119x29 cell grid in the axial, circumferential and radial directions respectively.

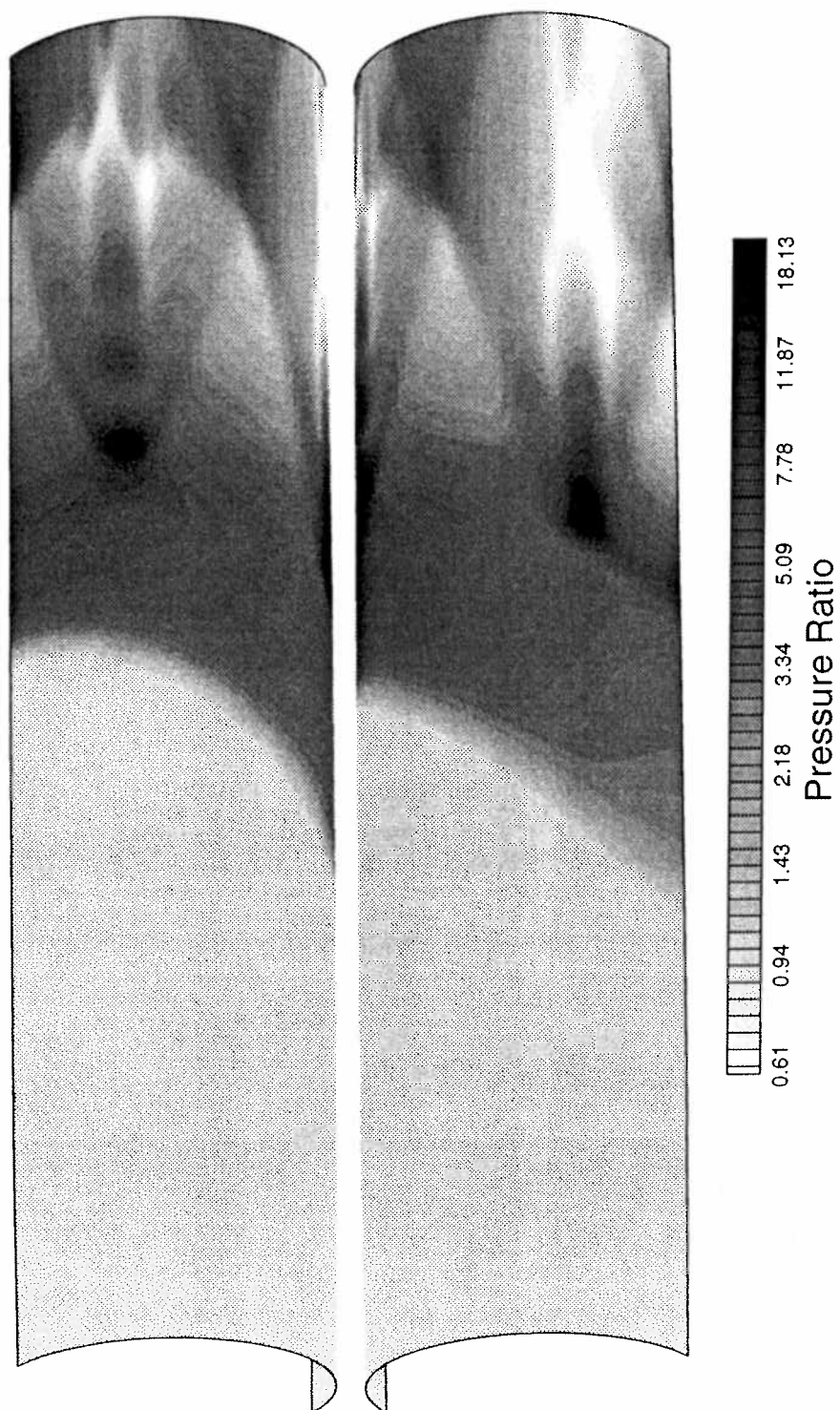


Figure 5-31: Three-dimensional surface plot of the calculated tube wall pressure distribution resulting from a canted projectile with fins which has an angle of attack of 3° and a nose tip translation of 6.5 mm. Superdetonative regime, 1920 m/s (Mach 5.3) or 110% of the C-J detonation speed. Surface shading is proportional to pressure.

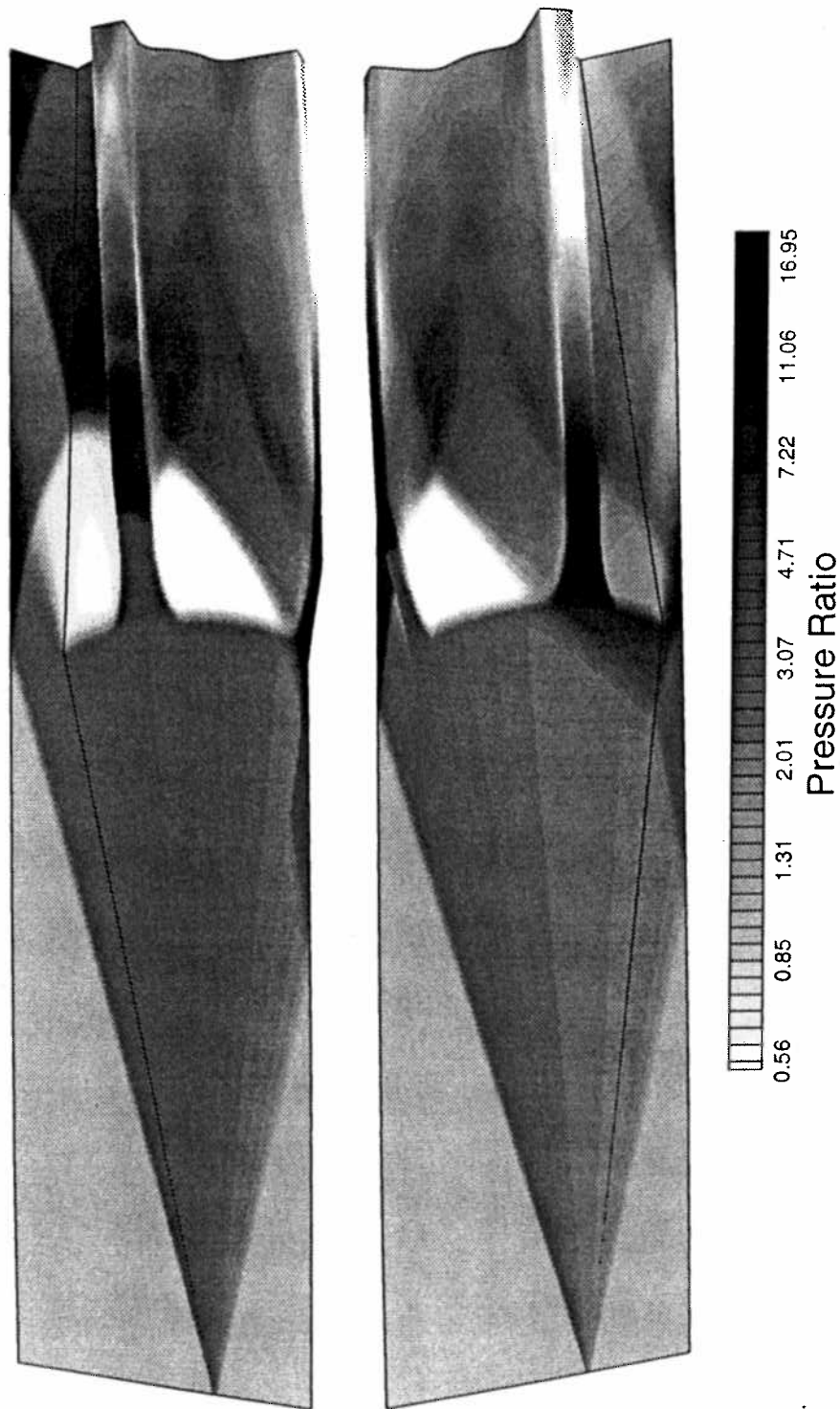


Figure 5-32: Three-dimensional surface plot of the calculated body surface pressure distribution of a canted projectile with fins which has an angle of attack of 3° and a nose tip translation of 6.5 mm. Pressure distribution of the upper and lower symmetry planes also shown. Supersonic regime, 1920 m/s (Mach 5.3) or 110% of the C-J detonation speed. Surface shading is proportional to pressure.

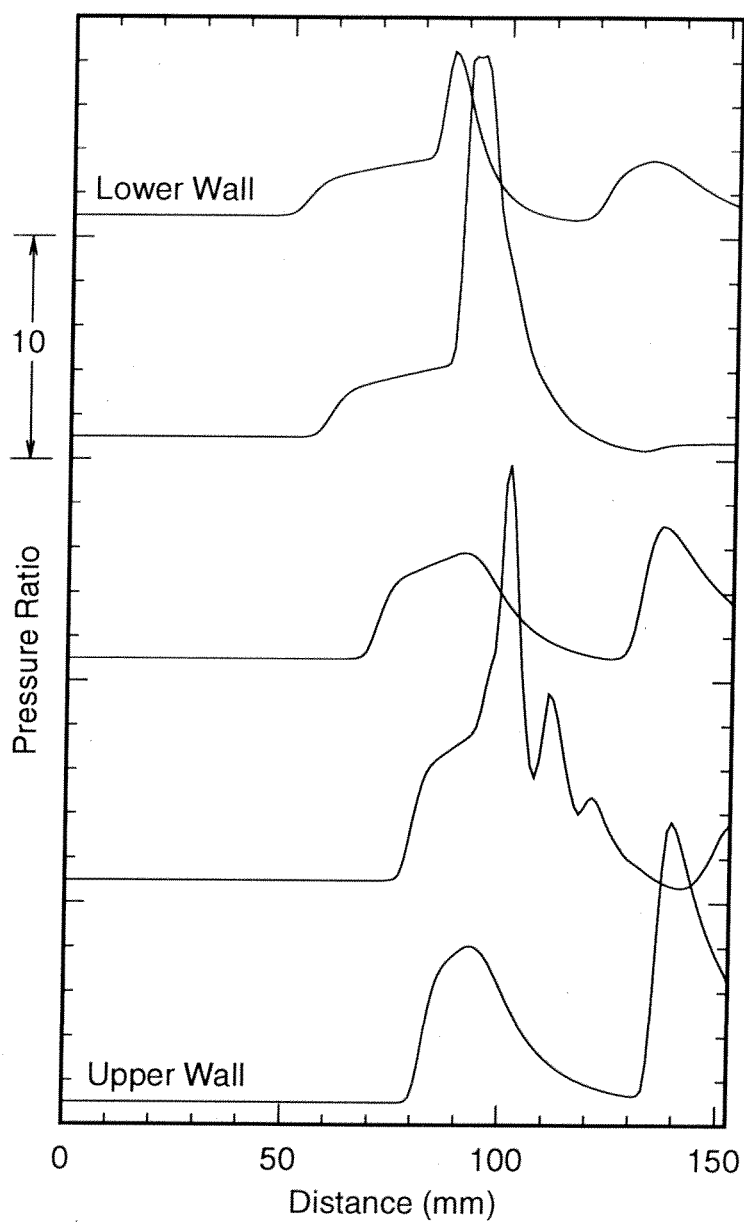


Figure 5-33: Line plots of the calculated tube wall pressure distribution of a canted projectile with fins which has an angle of attack of 3° and a nose tip translation of 6.5 mm. Subdetonative regime, 1920 m/s (Mach 5.3) or 110% of the C-J detonation speed. These 5 traces correspond to 45° increments in circumferential angle from the upper to lower wall.

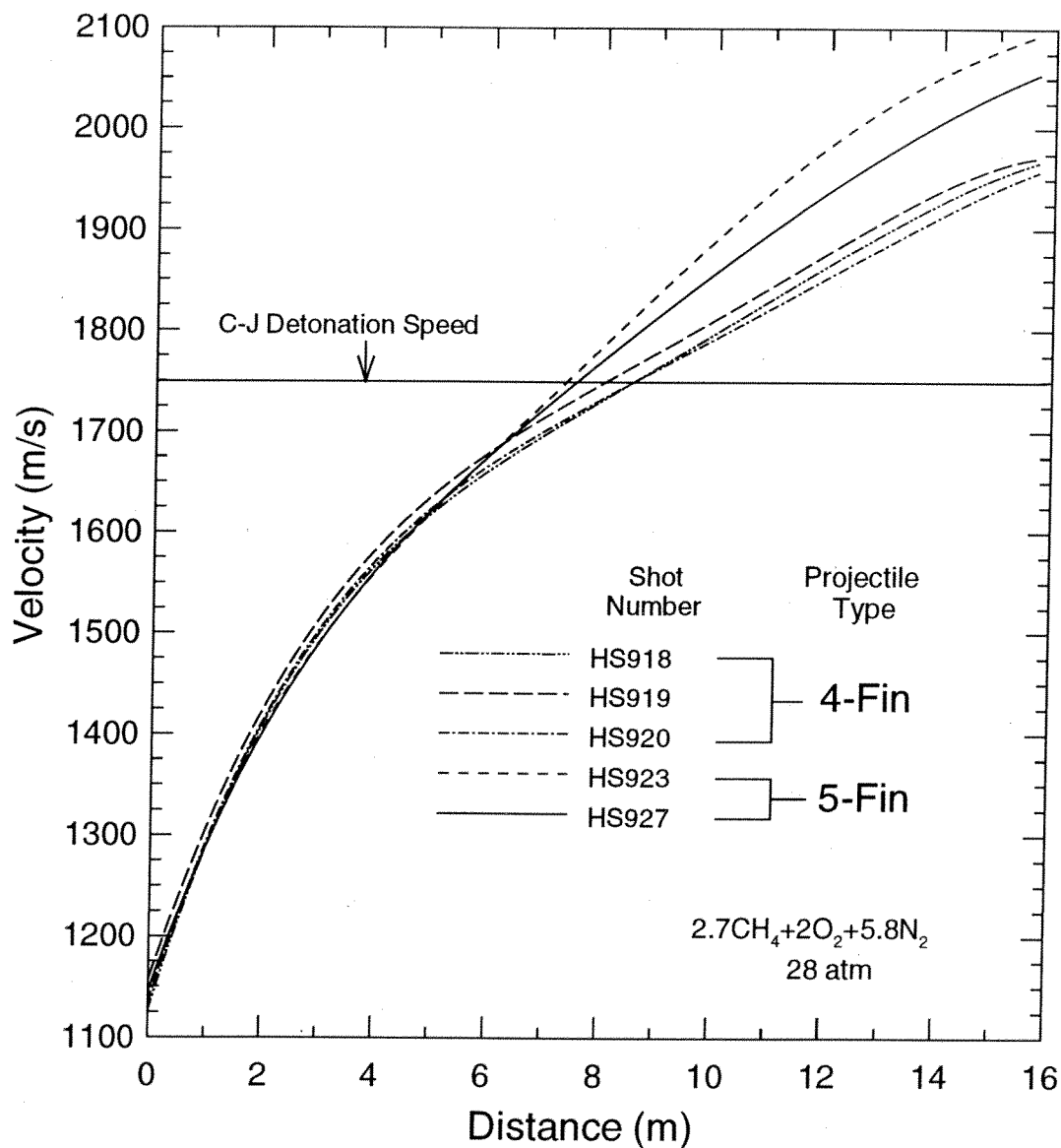


Figure 5-34: Plot of projectile velocity versus distance for 5-fin and 4-fin projectiles. Single-stage of 16 m in length, gas mixture of $2.7\text{CH}_4 + 2\text{O}_2 + 5.8\text{N}_2$, and a tube fill pressure of 28 atm. Projectile masses are 74 gm and 84 gm for 4-fin and 5-fin projectiles respectively.

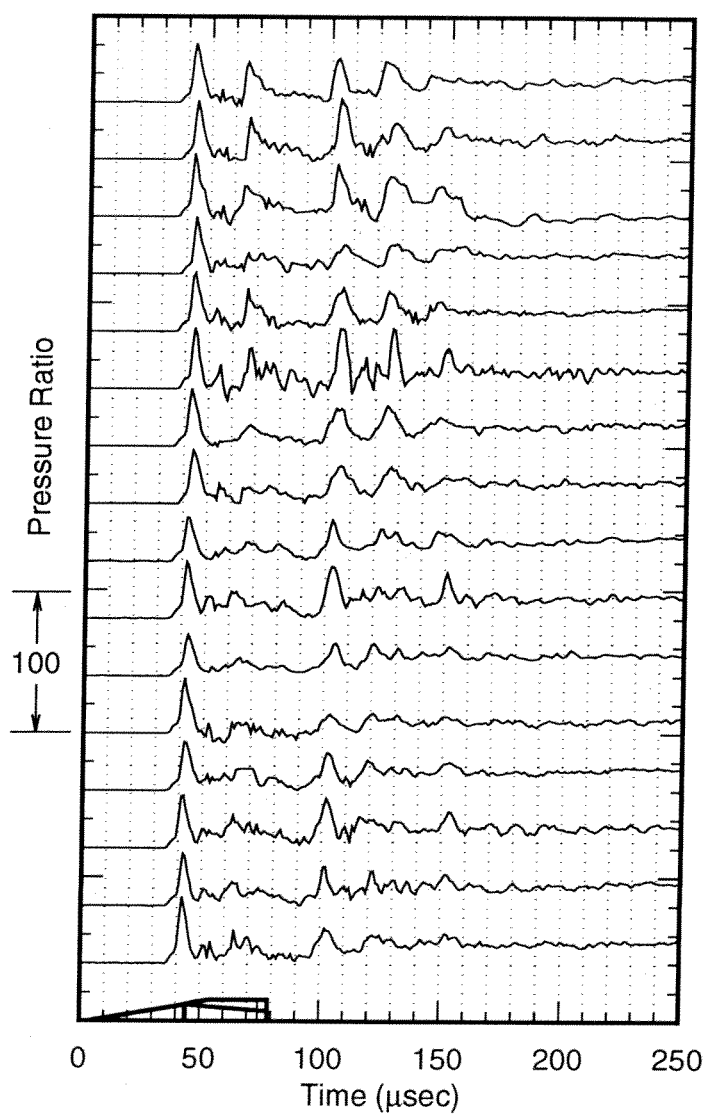


Figure 5-35: Tube wall pressure traces from a projectile unstart. Superdetonative regime, 2060 m/s (Mach 5.7) or 118% of the C-J detonation speed. Note the large amplitude shock wave and the remains of the initial conical shock generated by the projectile nose cone.

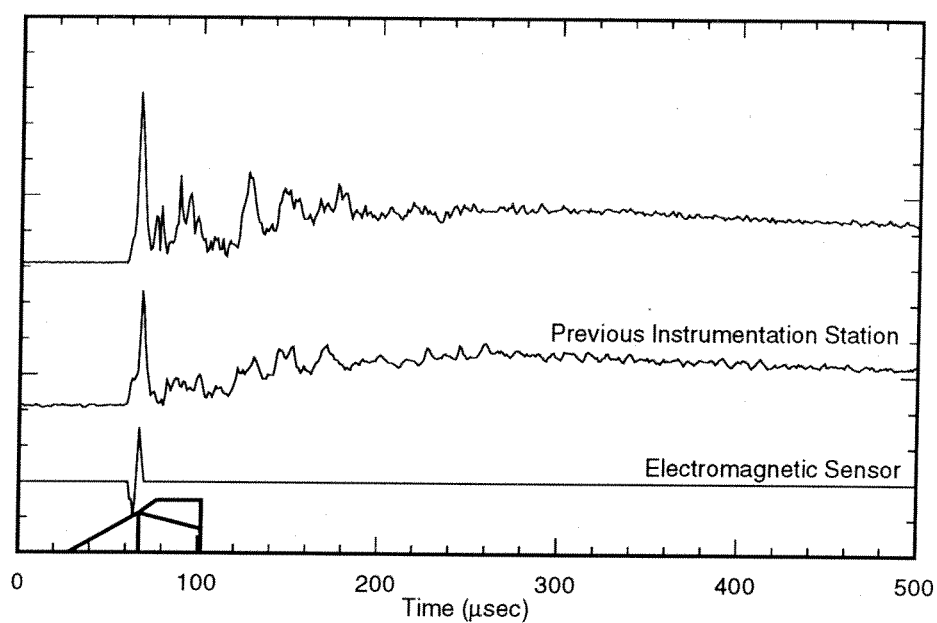


Figure 5-36: Comparison of data from trace 1 of Fig. 5-35 to that of an instrumentation station approximately 22 cm upstream (opposite the direction of projectile motion) with the same azimuthal orientation. Magnetic sensor data shown below to correlate projectile position with the pressure traces. Note difference in shock pressure peak amplitude.

Chapter 6: Conclusions

This chapter consists of the conclusions reached from performing research into the three-dimensional flow field of the ram accelerator projectile. The inherent three-dimensionality of the flow field is discussed as well as the effects of projectile canting. The combustion phenomena which were observed are summarized and recommendations for further research are proposed.

6.1 Three-Dimensionality of the Projectile Flow Field

The highly three-dimensional nature of the projectile flow field was found to be due mainly to the presence of the fins which serve to keep the axisymmetric projectile body centered in the tube. The fins have a significant effect on the structure of the flow field in the channels between fins as well as in the flow field behind the projectile. The number of fins (four or five and perhaps even more) also has a measurable affect on projectile performance, mainly in the area of thrust augmentation, with 5-fin projectiles exhibiting increased thrust levels over 4-fin projectiles (although not necessarily higher ultimate velocities). Thus the fin interaction with the flow field is quite important and must be taken into account to determine the performance of a ram accelerator projectile of a particular geometry.

6.2 Projectile Canting

Canting of the projectile was shown to be common in almost all experiments and was successfully numerically simulated, thus confirming the experimental results. It appears that the effects of this phenomenon are a very significant problem and evidence was presented which supports the claim that superdetonative unstarts (and perhaps transition failures in multiple stage experiments) are caused by the canting phenomenon. The obvious way to avoid these problems is to prevent the projectile from canting in the tube. This may be accomplished by utilizing 5-fin projectiles manufactured from higher strength and more heat resistant materials such as titanium or other exotic materials.

6.3 Combustion Phenomena

The experiments conducted for this dissertation observed many types of combustion phenomena which occurred at very high pressures. The shock induced combustion present in the diffuser at superdetonative Mach numbers was not totally unexpected, but the fact that, numerically at least, the diffuser does not unstart is quite promising assuming the problem of projectile canting can be solved. The experimentally observed and numerically simulated "ring-like" pressure variations in the flow field behind the projectile were linked to some type of combustion augmented shock structure which is not present in the non-reacting flow field and warrants further experimental and numerical research. A related topic, which has more of a basic research appeal is the investigation of combustion processes at pressures in the 100 to 1000 atm range. The chemical kinetics for even methane based mixtures are not all that well understood at near atmospheric pressures let alone hundreds of atmospheres.

6.4 Recommendations for Future Research

There are a few directions in which future research based on this dissertation could be directed. One would be the development of even more advanced instrumentation tech-

niques, such as using pressure transducers with much smaller sensitive areas, thus allowing increased circumferential spatial resolution. These transducers might be based on the conventional piezoelectric crystal design or the use of expendable transducers based on piezoelectric film technology may be possible. An improvement in the luminosity sensors which would give better reliability and provide better spatial discrimination of the visible radiation produced by combustion occurring in the projectile flow field would be extremely useful. In conjunction with these two ideas, higher data sampling may yield more useful information.

Numerically, more fully three-dimensional, chemically reacting Navier-Stokes simulations will be necessary to help understand the real flow field. This may be especially true in the case of canted projectiles at superdetonative velocities. The only caveat is related to reliable kinetic models and the associated rate data at elevated pressures. In fact, superdetonative experiments, similar to those performed herein, may act as an experimental benchmark against which new kinetic models may be compared. Additional Euler simulations may also be useful to optimize the projectile geometry or in fact develop completely new geometries which can then be tested in the laboratory.

References

- Anderson, W. K., Thomas, J. L., and Van Leer, B., 1986. "Comparison of Finite Volume Flux Vector Splittings for the Euler Equations," *AIAA Journal*, Vol. 24 (9).
- Arnone, A., Liou, M-S, and Povinelli, L. A., 1993. "Multigrid Time-Accurate Integration of Navier-Stokes Equations," AIAA Paper 93-3361.
- Blazek, J., Kroll, N., Radespiel, R., and Rossow, C-C., 1991. "Upwind Implicit Residual Smoothing Method for Multi-Stage Schemes," AIAA Paper 91-1533.
- Bruckner, A.P., Knowlen, C., and Hertzberg, A., 1991. "Operational Characteristics of the Thermally Choked Ram Accelerator," *Journal of Propulsion and Power*, Vol. 7, pp. 828-836.
- Burnham, E. A., 1993. "Investigation of Starting and Ignition Transients in the Thermally Choked Ram Accelerator," Ph.D. dissertation, University of Washington.
- Dadone, A. and Grossman, B., 1992. "Characteristic-Based, Rotated Upwind Scheme for the Euler Equations," *AIAA Journal*, Vol. 30 (9).
- Enander, R., 1993. "Improved Implicit Residual Smoothing for Steady State Computations for First-Order Hyperbolic Systems," *Journal of Computational Physics*, **107**, pp. 291-296.
- Gaitonde, D. and Shang, J.S., 1993. "Accuracy of Flux-Split Algorithms in High-Speed Viscous Flows," *AIAA Journal*, Vol. 31 (7).
- Hertzberg, A., Bruckner A.P., and Bogdanoff, D.W., 1988. "Ram Accelerator: A New Chemical Method for Accelerating Projectiles to Ultrahigh Velocities," *AIAA Journal*, Vol. 26, pp. 195-203.

- Hertzberg, A., Bruckner, A.P., and Knowlen, C., 1991. "Experimental Investigation of Ram Accelerator Propulsion Modes," *Shock Waves*, Vol. 1, pp. 17-25.
- Hinkey, J.B., Burnham, E.A., and Bruckner, A.P., 1993. "Investigation of Ram Accelerator Flow Fields Induced by Canted Projectiles," AIAA Paper 93-2186.
- Hinkey, J.B., Burnham, E.A., and Bruckner, A.P., 1992. "High Spatial Resolution Measurements In A Single Stage Ram Accelerator," 29th JANNAF Combustion Subcommittee Meeting.
- Hinkey, J.B., Burnham, E.A., and Bruckner, A.P., 1992. "High Spatial Resolution Measurements of Ram Accelerator Gas Dynamic Phenomena," AIAA Paper 92-3244.
- Holmes, D. G., 1989. "Inviscid 2-D Solutions on Unstructured, Adaptive Grids," Numerical Methods for Flows in Turbomachinery, von Karman Institute for Fluid Dynamics, Lecture Series 1989-06.
- Ingram, D. M., Lambert, C., Batten, P., and Causon, D. M., 1993. "Hydrodynamic Code Calculations of a Blast on a Tank Farm," presented at the poster session of the 19th International Symposium on Shock Waves, to appear in *SIAM*.
- Jameson, A. and Baker, T. J., 1983. "Solution of the Euler Equations for Complex Configurations," AIAA Paper 83-1929.
- Jameson, A., Schmidt, W., and Turkel, E., 1981. "Numerical Solutions of the Euler Equations by Finite Volume Methods Using Runge Kutta Time-Stepping Schemes," AIAA Paper 81-1259.
- Knowlen, C., Higgins, A. J., Hinkey, J. B., Burnham, E. A., and Mattick, A. T., 1992. "Diagnostic Techniques for Ram Accelerator Phenomena," 43rd Meeting of the Aeroballistic Range Association.
- Knowlen, C., Li, J.G., Hinkey, J., and Dunmire, B., 1991. "University of Washington Ram Accelerator Facility," 42nd Meeting of the Aeroballistic Range Association.
- Liou, M-S. and Steffen, C.J., 1993. "A New Flux Splitting Scheme," *Journal of Computational Physics*, **107**, pp. 23-39.

- Martinelli, L. and Jameson, A., 1988. "Validation of a Multigrid Method for the Reynolds Averaged Equations," AIAA Paper 88-0414.
- Rizzi, A. and Eriksson, L-E, 1984. "Computation of flow around wings based on the Euler equations," *J. Fluid Mech.* Vol. 148, pp. 45-71.
- Roe, P. L., 1981. "Approximate Riemann Solvers, Parameter Vectors, and Difference Schemes," *Journal of Computational Physics*, **43**, pp. 357-372.
- Soetrisno, M., Imlay, S.T., and Roberts, D.W., 1993. "Numerical Simulations of the Superdetonative Ram Accelerator Combusting Flow Field," AIAA Paper 93-2185.
- Soetrisno, M., Imlay, S.T., and Roberts, D.W., 1992. "Numerical Simulations of the Transdetonative Ram Accelerator Combusting Flow Field on a Parallel Computer," AIAA Paper 92-3249.
- Taylor, G.I. and Maccoll, J.W., 1937. "The Air Pressure on a Cone Moving at High Speeds," *Proceedings of the Royal Society of London, Series A*, Vol. 159, pp. 459-472.
- Van Leer, B., Tai, C-H, and Powell, K. G., 1989. "Design of Optimally Smoothing Multi-Stage Schemes for the Euler Equations," AIAA Paper 89-1933.
- Welch, G. E. and Chima, R. V., 1993. "Two-Dimensional CFD Modelling of Wave Rotor Flow Dynamics," AIAA Paper 93-3318.
- Yee, H. C., Klopfer, G. H., and Montagne, J.-L., 1988. "High-Resolution Shock-Capturing Schemes for Inviscid and Viscous Hypersonic Flows," NASA TR 100097.
- Zhu, Z. W., Lacor, C., and Hirsch, C., 1993. "A New Residual Smoothing Method for Multigrid, Multi-Stage Schemes," AIAA Paper 93-3356.

Appendix

This appendix contains a table which lists all of the experiments conducted with either the HITS or the inserts. The absolute pressure (atmospheres), velocity (m/s), which high density tube section was used, position of the HITS or inserts, which type of projectile (4- or 5-fin), and whether a reacting ($2.7\text{CH}_4+2\text{O}_2+5.8\text{N}_2$) or an inert ($2.7\text{CH}_4+7.8\text{N}_2$) gas was used are listed for each shot. The position of the HITS or the inserts is indicated by, for example, 1/2, which means that the HITS or inserts were placed at the joint between tubes 1 and 2.

Shot #	Pressure (atm)	Velocity (m/s)	HITS or Inserts	Location	Projectile Type	Reacting/ Inert
HS890	24	1540	HITS	3/4	4-fin	Reacting
HS916	24	1667	HITS	4/5	4-fin	Reacting
HS917	28	1750	HITS	4/5	4-fin	Reacting
HS918	28	1750	HITS	4/5	4-fin	Reacting
HS919	28	1873	HITS	6/7	4-fin	Reacting
HS920	28	1849	HITS	6/7	4-fin	Reacting
HS921	28	1560	HITS	2/3	4-fin	Reacting
HS922	18	1437	HITS	2/3	4-fin	Reacting
HS923	28	1560	HITS	2/3	5-fin	Reacting
HS927	28	1850	HITS	5/6	5-fin	Reacting
HS928	28	1400	HITS	1/2	4-fin	Reacting

Shot #	Pressure (atm)	Velocity (m/s)	HITS or Inserts	Location	Projectile Type	Reacting/ Inert
HS951	30	1960	Inserts	7/8	4-fin	Reacting
HS952	33	2020	Inserts	7/8	4-fin	Reacting
HS953	30	2040	Inserts	7/8	5-fin	Reacting
HS983	28	1406	Inserts	2/3	4-fin	Inert
HS984	33	1646	Inserts	4/5	4-fin	Inert
HS985	33	1920	Inserts	7/8	4-fin	Inert
HS987	33	1950	Inserts	7/8	4-fin	Reacting
HS988	35	2055	Inserts	7/8	4-fin	Reacting
HS989	28	1730	Inserts	4/5	4-fin	Reacting
HS990	28	1415	Inserts	1/2	4-fin	Reacting

Vita

John Benjamin Hinkey, Jr. was born July 20, 1965 in North Tonawanda, New York. After graduating eleventh out of a class of approximately 430 from Hamburg High School in 1983, he attended the State University of New York at Buffalo and completed a Bachelors of Science Degree in Aerospace Engineering in 1987. He then continued on to graduate school where he studied hypersonics until graduating with a Masters of Science Degree in June of 1990. His Doctoral studies were performed at the University of Washington in Seattle, where he experimentally and numerically studied the three-dimensional flow field about a ram accelerator projectile, associated combustion phenomena, detonation waves, and unsteady compressible flows.

Publications:

Hinkey, J.B., Burnham, E.A., and Bruckner, A.P., 1994. "High Spatial Resolution Measurements In A Single Stage Ram Accelerator," accepted for publication in the *Journal of Propulsion and Power*.

Hertzberg, A., Burnham, E., and Hinkey, J., 1993. "Recent Advances in Ram Accelerator Technology," to appear in the proceedings of *ICASE*.

Hertzberg, A. Takayama, K., Hinkey, J., and Itaka, S., 1993. "The Taylored Nozzle: A Method for Reducing the Convective Heat Transfer to Nozzle Throats by Gas Dynamic Shielding," *Proceedings of the 19th International Symposium on Shock Waves*.

Hinkey, J.B., Burnham, E.A., and Bruckner, A.P., 1993. "Investigation of Ram Accelerator Flow Fields Induced by Canted Projectiles," AIAA Paper 93-2186.

- Hinkey, J.B., Burnham, E.A., and Bruckner, A.P., 1992. "High Spatial Resolution Measurements In A Single Stage Ram Accelerator," 29th JANNAF Combustion Subcommittee Meeting.
- Hinkey, J.B., Burnham, E.A., and Bruckner A.P., 1992. "High Spatial Resolution Measurements of Ram Accelerator Gas Dynamic Phenomena," AIAA Paper 92-3244.
- Knowlen, C., Higgins, A. J., Hinkey, J. B., Burnham, E. A., and Mattick, A. T., 1992. "Diagnostic Techniques for Ram Accelerator Phenomena," 43rd Meeting of the Aeroballistic Range Association.
- Knowlen, C., Li, J.G., Hinkey, J., and Dunmire, B., 1991. "University of Washington Ram Accelerator Facility," 42nd Meeting of the Aeroballistic Range Association.
- Hinkey, J. B., 1990. "Performance of a Hypersonic Shock Tunnel Incorporating a Monotonic Area Reduction at the Diaphragm of the Shock Tube," Master of Science Thesis, State University of New York at Buffalo.